TÉCNICO LISBOA

Numerical Investigation on the Influence of the Fuel on the Performance of a Laboratory Combustor

Pedro Daniel Canuto Rijo

Thesis to obtain the Master of Science Degree in

Mechanical Engineering

Supervisor: Prof. Pedro Jorge Martins Coelho

Examination Committee

Chairperson: Prof. Carlos Frederico Neves Bettencourt da Silva

Supervisor: Prof. Pedro Jorge Martins Coelho

Member of the Committee: Prof. Daniel Cardoso Vaz

July 2020

Abstract

In this work, numerical simulations were performed to study the fuel flexibility of a small-scale combustor operating in the flameless combustion mode. The combustor geometrical characteristics and the operating conditions, such as thermal power and equivalence ratio (φ), were kept constant for all fuels studied.

The studied fuels were: methane, propane, acetylene, ethanol, biogas, syngas, hydrogen and mixtures of CH_4/H_2, CH_4/NH_3 and H_2/NH_3. In the CH_4/NH_3 and H_2/NH_3 mixtures, the influence of NH_3 concentration and the equivalence ratio (φ) to obtain this combustion regime were also studied. The numerical model applied was validated through the numerical and experimental comparison of the temperature and species concentration fields obtained from the methane flameless combustion.

All calculations were performed using the commercial code *Ansys Fluent 18.* The combustion model applied was the Eddy Dissipation Concept (EDC) coupled with a suitable kinetic mechanism for each studied fuel. The turbulence model was the realizable k-ε model and the radiation model used was the discrete ordinate model.

The numerical results show that for a preheated air temperature of 900 K and $\varphi = 0.5$, flameless combustion can be obtained for all fuels except acetylene, syngas and hydrogen. These three fuels have a non-uniform temperature field combined with rapid oxygen and fuel consumption, which suggests the presence of a flame front. In the CH_4/NH_3 and H_2/NH_3 mixtures, the flameless combustion can be established for the two NH_3 concentrations studied and also for $\varphi \leq 1$. In the fuel-rich condition ($\varphi = 1.2$), the numerical results suggest the presence of a flame front for both mixtures. Flameless combustion is characterized by low NO_x emissions (< 15 ppm) for nitrogen-free fuels. However, the NO_x concentration obtained in the CH_4/NH_3 and H_2/NH_3 mixtures is above 800 ppm for this combustion mode, which suggests a need to optimize flameless combustion for ammonia-rich fuels.

Keywords

Combustor flexibility, flameless combustion, acetylene, biogas, ethanol, hydrogen, methane, propane, syngas, ammonia combustion.

Resumo

Neste trabalho, foram realizadas simulações numéricas para estudar a flexibilidade no combustível de uma pequena câmara de combustão laboratorial que opera no modo de combustão sem chama visível. As características geométricas da fornalha e as condições operatórias, como a potência térmica e a razão de equivalência (φ), foram mantidas constantes para todos os combustíveis estudados.

Os combustíveis estudados foram: o metano, o propano, o acetileno, o etanol, o biogás, o syngas, o hidrogénio e as misturas de CH_4/H_2, de CH_4/NH_3 e de H_2/NH_3. Nas misturas de CH_4/NH_3 e de H_2/NH_3 foram também estudadas a influência da concentração de NH_3 e da razão de equivalência para a obtenção deste regime de combustão. A validação do modelo numérico aplicado foi feita através da comparação dos resultados numéricos e experimentais dos campos de temperatura e de concentração de espécies obtidos na combustão sem chama visível do metano.

Todos os cálculos foram realizados recorrendo ao software comercial *Ansys Fluent 18*. O modelo de combustão aplicado foi o Eddy Dissipation Concept (EDC) acoplado com o mecanismo cinético mais adequado para cada combustível estudado. O modelo de turbulência foi o modelo k-ε realizável e o modelo de radiação utilizado foi o modelo das ordenadas discretas.

Os resultados numéricos mostram que para uma temperatura de pré-aquecimento do ar de 900 K e φ = 0.5, a combustão sem chama visível pode ser obtida para todos combustíveis com excepção para o acetileno, o syngas e o hidrogénio. Estes três combustíveis apresentam um campo de temperaturas não uniforme acompanhado por um rápido consumo de oxigénio e de combustível, o que sugere a presença de uma frente de chama. Nas misturas de CH_4/NH_3 e de H_2/NH_3, a combustão sem chama visível pode ser obtida para as duas concentrações de NH_3 estudadas e também para $\varphi \leq 1$. Na condição rica em combustível (φ = 1.2), os resultados numéricos sugerem a presença de uma frente de chama para ambas as misturas. A combustão sem chama visível é caracterizada por baixas emissões de NO_x (< 15 ppm) para combustíveis sem azoto. No entanto, a concentração de NO_x obtida neste modo de combustão para as misturas de CH_4/NH_3 e de H_2/NH_3 é superior a 800 ppm, o que sugere a necessidade de optimizar a combustão sem chama visível para os combustíveis ricos em amoníaco.

Palavras-chave

Flexibilidade da câmara de combustão, combustão sem chama visível, acetileno, biogás, etanol, hidrogénio, metano, propano, combustão de amoníaco.

Acknowledgements

Firstly and foremost, I would like to thank my supervisor Professor Pedro Coelho for all the unceasing support and availability during this research work. All the meetings, emails or simple conversations contributed to the development of the present work.

I would also to thank Rodolfo Rocha and my sister for their availability and support during the numerical simulations and many helpful discussions.

Also to all the friends who accompanied me during the development of this thesis: Fábio Baptista, Gonçalo Pacheco, Inês Ferrão, Miguel Franco, Níbia Silva, Ricardo Ferreira, Tiago Rio and Tomás Fernandes, for all the camaraderie, friendship, support and all the funny moments and relaxed conversations promoted.

Finally, special thanks to my parents, who have always supported me and gave everything they could to make these academic years easier.

Table of Contents

List of Figures

List of Tables

Nomenclature

Roman Characters

Lower case letters

a – sound speed (m/s)

$a_{\varepsilon,i}$ – emissivity weighting factor for the ith fictious gray gases (-)

a_1 – SST k- ω constant (-)

b_{nuc}^{*} - normalized radical nuclei concentration (particles x 10^5/kg)

c_p – specific heat (J/(kg.K))

d_p – mean diameter of a soot particle (m)

g_i – gravitational acceleration in the i direction (m/s^2)

h – specific enthalpy (J/kg)

k – turbulent kinetic energy (m^2/s^2)

$j_{i,j}$ – mass diffusion flux in the j direction of i-species (kg/(m.s^2))

$j_{q,j}$ - component of the j direction of the heat flux vector (W/m^2)

l – length scale (m) or Moss-Brookes model constant (-)

m – Moss-Brookes model constant (-)

$\dot{m}_E$ – internal flue gas recirculation mass flow rate (kg/s)

$\dot{m}_{fuel}$ – fuel inlet mass flow rate (kg/s)

$\dot{m}_{air}$ – air inlet mass flow (kg/s)

$\dot{m}_J$ – entrained gases mass flow rate (kg/s)

n – Moss-Brookes model constant (-)

$\vec{n}$ – normal vector to the surface (m)

p – pressure (Pa)

p_i – partial pressure of the ith gray gas (Pa)

$\vec{q}$ – radiative heat flux vector (W/m^3)

$\dot{q}_R'''$ – heat exchange by radiation (W/m^3)

s – path length (m)

$\vec{s}$ – direction vector (m)

t – time (s)

u – component of the flow velocity perpendicular to the gravitational vector (m/s)

u_j – the j direction of the velocity vector (m/s)

v – component of the flow velocity parallel to the gravitational vector (m/s)

w_j – weight of the quadrature in the j direction (-)

x_j – position (m)

y – distance to the next surface (m)

y_i – mass fraction of i-species (-)

Upper case letters

A_E – east face area of the volume element (m^2)

A_N – north face area of the volume element (m^2)

A_S – south face area of the volume element (m^2)

A_W – west face area of the volume element (m^2)

A_0 – realizable k-ε model constant (-)

A_S – realizable k-ε model constant (-)

C_1 – realizable k-ε model constant (-)

$C_{1\varepsilon}$ – k-ε model constant (-)

$C_{2\varepsilon}$ – k-ε model constant (-)

$C_{3\varepsilon}$ – k-ε model constant (-)

C_{ξ} – EDC constant (-)

C_{τ} – EDC constant (-)

C_{μ} – k-ε model constant (-)

C_α – Moss-Brookes model constant for soot inception rate (s^{-1})

C_β – Moss-Brookes model constant for coagulation rate (-)

C_γ – surface growth rate scaling factor ((kg.m)/(kmol.s))

C_ω – oxidation model constant ((kg.m)/(kmol.$s.K^{1/2}$)

C_{oxid} – oxidation rate scaling parameter (-)

D^M – mass diffusivity (m^2/s)

D_ω – cross-diffusion term (kg/(m.s^3))

D_ω^+ – positive portion of the cross-diffusion term (kg/(m.s^3))

$F()$ – compressibility function (-)

G_b – generation of turbulence kinetic energy due to buoyancy (kg/(m.s^3))

G_{inc} – incident radiation (W/m^2)

G_k – generation of turbulence kinetic energy due to the mean velocity gradients (kg/(m.s^3))

G_k – production of turbulence kinetic energy (kg/(m.s^3))

G_ω – generation of ω (kg/(m.s^3))

$I(\vec{s})$ – radiative intensity in the direction $\vec{s}$ (W/m^2)

I_b – blackbody radiative intensity (W/m^2)

$I_w(\vec{s})$ – radiative intensity of the surface in the direction $\vec{s}$ (W/m^2)

I_{bw} – blackbody intensity on the surface (W/m^2)

I_E^n – average radiant intensity of the east face (W/m^2)

I_W^n – average radiant intensity of the west face (W/m^2)

I_N^n – average radiant intensity of the north face (W/m^2)

I_S^n – average radiant intensity of the south face (W/m^2)

I_P^n – average intensity of the volume element center (W/m^2)

K_v – internal flue gas recirculation rate (-)

L – reference length (m)

Le_i – Lewis number of i-species (-)

M – soot mass concentration (kg/m^3)

M_i – molar weight of i-species (kg/kmol)

M_P – mass of an incipient soot particle (kg/kmol)

M_t – turbulent Mach number (-)

M_{t0} – SST k- ω constant (-)

N – soot particle number density (particles/m^3)

N_A – Avogadro Number (kmol^{-1})

Re – Reynolds number (-)

$R_{i,r}$ – formation rate of i-species in reaction r (kg/(m.s^3))

R_β – SST k- ω constant (-)

R_k – SST k- ω constant (-)

R_ω – SST k- ω constant (-)

S – strain rate magnitude (-) or modulus of the mean rate-of-strain tensor (1/s)

S_k – user-defined source term in k-ε model or in k-ω model (kg/(m.s^3))

S_ε – user-defined source term in k-ε model (kg/(m.s^3))

S_ω – user-defined source term in k-ω model (kg/(m.s^3))

T_α – activation temperature of soot inception (K)

T_γ – activation temperature of surface growth rate (K)

U – fluid velocity (m/s)

X_{OH} – mole fraction of OH radical (-)

X_{prec} – mole fraction of soot precursor (-)

X_{sgs} – mole fraction of the participating surface growth species (-)

$\tilde{Y}_i$ – average mass fraction of i-species (-)

Y_i^* – mass fractions of i-species inside the fine structure (-)

Y_i^o – mass fractions of i-species outside the fine structure (-)

Y_k – dissipation of k due to the turbulence (kg/(m.s^3))

Y_M – contribution of the fluctuating dilatation in compressible turbulence to the overall dissipation rate ((kg.s^3)/m)

Y_ω – dissipation of ω due to the turbulence (kg/(m.s^3))

Greek characters

Lower case letters

α – thermal diffusivity (m^2/s)

α_∞ – SST k- ω constant (-)

α_0 – SST k- ω constant (-)

α_∞^* – SST k- ω constant (-)

β – thermal expansion coefficient (1/K)

$\beta_{i,1}$ – SST k- ω constant (-)

$\beta_{i,2}$ – SST k- ω constant (-)

β_∞^* – SST k- ω constant (-)

δ_{ij} – Kronecker's delta function (-)

ε – dissipation rate of turbulence kinetic energy (m^2/s^3)

ε_w – emissivity of the surface (-)

ζ^* – SST k- ω constant (-)

η_{coll} – collisional efficiency parameter (-)

η^n – cosine director of a direction n (-)

θ' – angle between any incoming $\overrightarrow{s'}$ and the normal vector (rad)

κ – absorption coefficient of the medium (-)

κ_i – absorption coefficient of the ith gray gas (1/m)

λ – thermal conductivity (W/(m.K)) or excess air coefficient (-)

μ – dynamic viscosity of the fluid (kg/(m.s))

μ_t – turbulent viscosity (kg/(m.s))

ν – cinematic viscosity (m^2/s)

ξ – length of the fine structure (m)

ξ^n – cosine director of a direction n (-)

ρ – fluid density (kg/m^3)

ρ_w – reflectivity of the surface (-)

ρ_{soot} – soot density (kg/m^3)

σ_k – turbulent Prandtl numbers for k (-)

σ_ε – turbulent Prandtl numbers for ε (-)

$\sigma_{k,1}$ – SST k- ω constant (-)

$\sigma_{k,2}$ – SST k- ω constant (-)

$\sigma_{\omega,1}$ – SST k- ω constant (-)

$\sigma_{\omega,2}$ – SST k- ω constant (-)

τ – time scale (s) or time scale of the fine structure (s)

τ_{ij} – viscous stress tensor (-)

φ – equivalence ratio (-)

ω – specific turbulent energy dissipation rate (1/s)

$\dot{\omega}_i$ – formation/destruction rate of i-species ($kg/(m^3.s)$)

ω_k – angular velocity (rad/s)

Upper case letters

Γ_k – effective diffusivity of k (kg/(m.s))

Γ_ω – effective diffusivity of ω (kg/(m.s))

Ω_{ij}– rate of rotation tensor (rad/s)

Exponents

$(\bar{})$ – Reynolds time average

$(\breve{})$ – Favre mass-weighted average

$(\,)'$ – Reynolds fluctuation

$(\,)''$ – Favre fluctuation

$(\,)^0$ – Relative to the fine structure surroundings

$(\,)^*$ – Relative to the fine structures

Acronyms

CCS – Carbon Capture and Storage system

CDC – Colorless Distribution Combustion

CFD – Computational Fluid Dynamic

DO – Discrete Ordinates

EDC – Eddy Dissipation Concept

EDM/FR – Eddy Dissipation Model with Finite-Rate chemistry

FLOX – Flameless Oxidation

GHG – Greenhouse Gases

HiTAC – High Temperature Air Combustion

MILD – Moderate or Intense Low-oxygen Dilution combustion

PDF – Probability Density Function

PFR – Plug Flow Reactor

PSR – Perfect Stirred Reactor

RKE – Realizable k-ε model

RNG – Renormalization Group k-ε model

RTE – Radiative Transfer Equation

SKE – Standard k-ε model

SST – Shear Stress Transport

WSGG – Weighted Sum of Gray Gases

1. Introduction

1.1 Motivation

Since the first industrial revolution until today, global economic growth has been based on aggressive consumption of fossil fuels and their derivatives, which has led to an increase in the concentration of greenhouse gases (GHG) in the atmosphere. This consequence has contributed to an increase in the Earth's average temperature and an acceleration of climate change. To reduce the climate changes, around 195 countries have agreed to limit the Earth's average temperature increase to 1.5 ºC and have established a set of initiatives included in the Paris Agreement to achieve this aim [1].

One of the main initiatives is the strong reduction in GHG emissions, especially carbon dioxide (CO_2), carbon monoxide (CO), nitrogen oxides (NO_x), methane (CH_4) and floured gases. Figure 1.1 shows the evolution of the GHGs reduction to reach the goal of increasing the temperature of 1.5 ºC. From the year 2070 carbon neutrality is reached and the end of the 21st century there is the CO_2 removal from the atmosphere through the Earth's natural mechanisms and also by the implementation of CO_2 capture and storage systems [2].

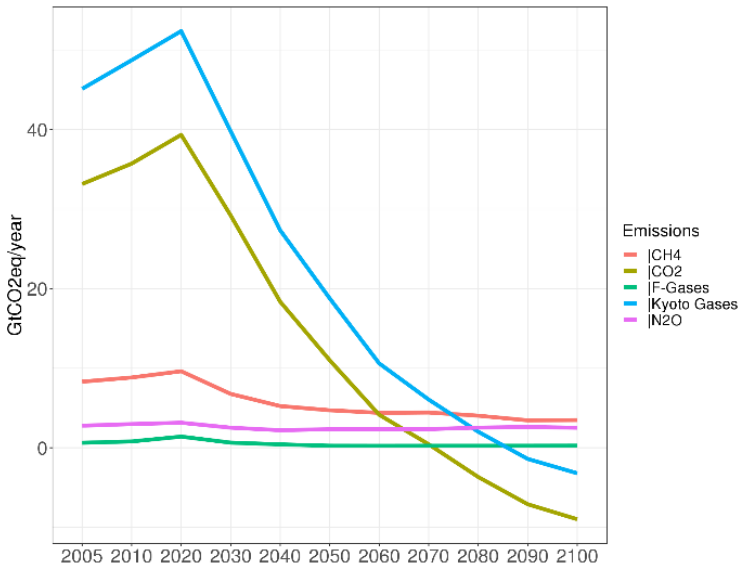

Figure 1.1 – Annual evolution of greenhouse gas emissions to reach the goal of increasing the temperature of 1.5 ºC [2].

The European Union forecasts [3] indicate that the main sectors that will contribute strongly to the CO_2 emission reduction are the power generation and industrial sectors despite the CO_2 emission increase in the transport sector, see figure 1.2. In 2005, the first two sectors were responsible for 48% of CO_2 emission and in 2050 they will be responsible for 28% while in the transport sector there is an increase of 24% recorded in 2005 to 41% in 2050. In the power generation sector, the strong CO_2 emission reduction is due to a paradigm shift in electricity production, which will see a transition from investments in thermoelectric plants to photovoltaic and wind power plants and the slow conversion of current thermoelectric plants in green hydrogen production and storage plants. The CO_2 emission increase observed in the transport sector is mainly due to the growth of air and road transport. Despite the hybrid

technologies and electrification underway in light vehicles, the European Union predicts the use of liquefied natural gas (LNG) to replace diesel in goods and passenger transports for medium and long-distance travel.

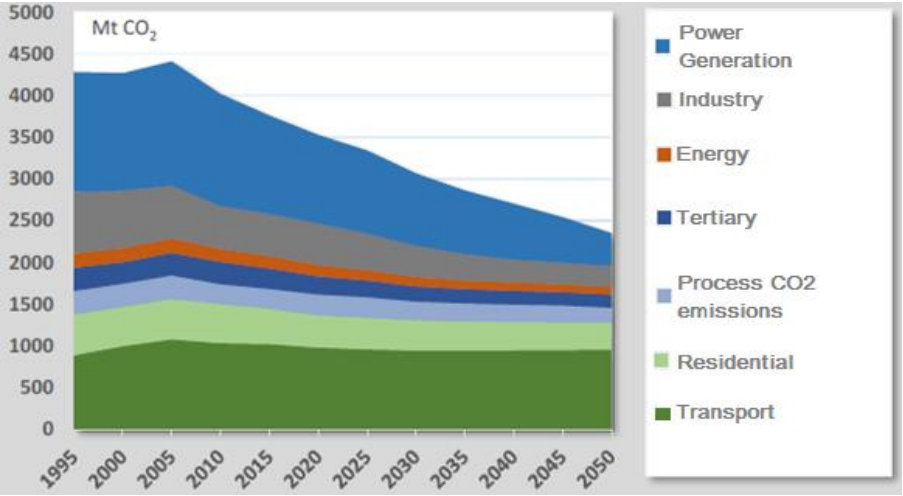

Figure 1.2 – Annual evolution of CO_2 emissions for each sector predicted by the European Union [3].

However, the transition from current thermal equipment to clean technologies is more difficult to occur in the industrial sector, especially in the metallurgical and cement industries, where temperatures in the manufacturing process are required above 1000 °C, which makes combustion an essential technology. Combustion is also essential in the power generation sector due to the uncertain supply of electricity from solar and wind sources. To make combustion a cleaner technology, it is necessary to use new combustion techniques, such as oxy-fuel combustion and flameless combustion, but also possibility to use green fuels and carbon capturing systems in order to reduce GHG emissions.

Oxy-fuel combustion is not technically a CO_2 capture technology, but a combustion process that takes place in an oxygen-enriched environment, that is, in the absence of nitrogen. The flue gases are composed essentially of CO_2 and water vapor where the water vapor is condensed and the CO_2 is compressed and stored in high pressure tanks [4]. The oxygen is removed from the air through a cryogenic air separation unit and it is diluted with the flue gases in order to maintain the combustion conditions similar to the conditions existing in the air-fired configuration. As a rule, the oxygen dilution is done through the external recirculation of 2/3 of the flue gases leaving the boiler or gas turbine [4]. This alternative allows CO_2 emissions close to zero when a carbon capture and storage system is coupled downstream of the boiler or gas turbine, see figure 1.3. The oxy-fuel combustion disadvantages are: the limited space of the current power plants to install this technology, the air separation and CO_2 compression units reduce net plant output by 25% in relation to the air-fired configuration, higher installation costs and little flexibility to change operating conditions [4].

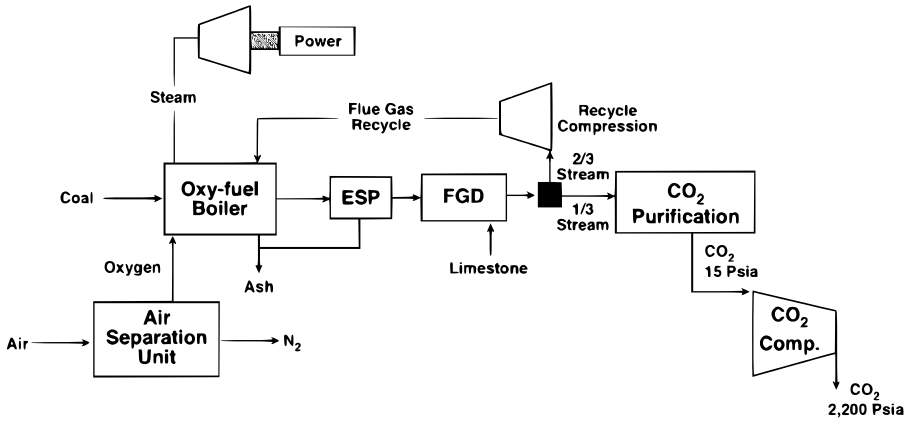

Figure 1.3 – Schematic diagram of a pulverized coal oxy-fuel combustion system with carbon capture and storage system. [4]

Carbon capture and storage (CCS) systems are technologies applied in post-combustion. The CO_2 capture can be done by four different techniques: by the use of physical and chemical solvents, through a membrane system or an adsorption system and finally by cryogenic separation [4]. Maximum efficiency occurs when this technology is installed together with oxy-fuel combustion technology. The CCS system disadvantages are: high installation costs, little mature technology, inefficient for large volumes of flue gases with low CO_2 concentration, i.e. inefficient technology when using the air-fired configuration and losses up to 30% of the net plant output [4].

Flameless combustion is characterized by a uniform distribution of temperature and O_2 concentration inside the combustion chamber due to a strong dilution of the reactants with the flue gases. It is a mature technology and has been successfully applied in the metallurgical industry. Flameless combustion allows an improvement of 30% in thermal efficiency, which means a reduction in fuel consumption and CO_2 emissions, as well as NO_x emission reduction of 70% [5]. With this technology, it is possible to burn fuels with low heating value where the flame instability, flashback or blow-off phenomena are not observed. The flameless combustion application involves lower installation costs compared to the two technologies mentioned above and allows to work with a wide range of operating conditions and different burner configurations. However, it is optimized for the fossil fuels combustion and more research is needed in the application of alternative fuels.

Currently, the thermal equipment in the industries and in the thermoelectric power plants are optimized for burning a certain fuel and are little flexible or even inflexible when the fuel is changed. When the fuel is changed, it is needed to install new burners or the other components in this thermal equipment.

Boyce [6], Khalil and Gupta [7] studied the gas turbine flexibility to burn new fuels. The authors observed that it is necessary to change the combustion type to maintain the same flame stability and to respect the same limit values for NO_x and carbon monoxide (CO) emissions. A change in the combustion type is necessary when the reactivity and/or the heating value of the new fuel differs significantly from the original fuel. The premixed combustion to non-premixed combustion transition requires that the burners have the ability to inject the premixed reactants in the same nozzle as well as the capacity to inject the fuel and oxidant in different nozzles [6,7].

1.2 Objectives

The present work intends to study the flameless combustion of different fuels using the same combustor and the same operating conditions, i.e. the same thermal power, equivalence ratio and air inlet temperature. The combustion of alternative fuels to natural gas, such as propane, biogas, syngas or ammonia (NH_3), is studied. The influence of NH_3 concentration on the mixture and the equivalence ratio for achieving flameless combustion are also studied. The numerical simulations were performed using a commercial code *Ansys Fluent 18*.

In this work three objectives were proposed. The first objective is to predict the velocity, temperature and chemical species concentration profiles in a small-scale flameless combustor for proposed fuels. The second objective is to study and compare the temperature contours and the normalized deviation of predicted temperature contours of the different fuels in order to verify which fuels burn in the flameless combustion mode, i.e. to study the flameless combustor flexibility. The third objective is to compare CO, CO_2 and NO_x emissions of the different fuels studied.

1.3 Structure of the Thesis

The thesis contains six chapters. In the first chapter, brief background information about the oxy-fuel combustion, flameless combustion and carbon capture and storage system are given and the objectives of the work are explained. The following chapter describes the theoretical description of flameless combustion and is accompanied by numerical and experimental works done in this area. The third chapter mathematically describes the reactive system equations, the turbulence, species transport and radiation models used in the commercial code. The Experimental and Numerical Setup chapter briefly describes the experimental methods and equipment necessary to perform the experimental campaign, while the numerical setup describes the computational domain and the boundary conditions used, as well as the air and fuel inlet velocities, and the chemical composition for each fuel. In this work, the experimental campaign was not carried out and the experimental data used are available in the literature. In the Results and Discussion chapter, all profiles of velocity, temperature and concentrations of chemical species are presented and the influence of the grid size and the turbulence models are studied. Moreover, the combustion type of each fuel is determined when it is subjected to the same boundary conditions. The last chapter presents the main conclusions of this thesis and suggests some topics to study in future works.

2. Literature Review

Chapter 2 is divided into four sections. The first section briefly describes the main combustion regimes. The second section explains the flameless combustion mechanism and finally the last two sections present experimental and numerical works performed in the flameless combustion.

2.1 Combustion Background

Before introducing the flameless combustion concept, this section explains the concepts and definitions to understand what combustion is and how it is classified.

Combustion is a common phenomenon for people and is present in the simplest and most easily accessible things, such as a lighter, or even in the most complex mechanisms, such as an internal combustion engine. Combustion is defined by a set of chemical reactions between a fuel, such as methane, with an oxidizer, usually air, associated with the heat and mass transfer phenomena. Combustion can occur in lean, stoichiometric and rich conditions. A generalized chemical reaction of a hydrocarbon in stoichiometric condition is shown below [8].

$$C_xH_y + (x + y/4)(O_2 + 3.76N_2) \rightarrow xCO_2 + (y/2)H_2O + 3.76(x + y/4)N_2$$

In air, the O_2 to N_2 volumetric ratio is approximately 1:3.76 and the combustion occurs in the stoichiometric condition when the amount of oxidant is theoretically enough to convert one mole of fuel into CO_2 and H_2O, i.e., when the equivalence ratio is equal to one (φ = 1). The stoichiometric oxidizer-fuel ratio is calculated through equation 2.1, where M_{O2}, M_{N2} and M_{fuel} are the molecular weights of oxygen, nitrogen and hydrocarbon used as fuel. The equivalence ratio (φ) is defined as the ratio of the fuel-to-oxidizer ratio in an arbitrary mixture (m_{fuel}/m_{ox}) to the stoichiometric fuel-oxidizer ratio ($(m_{fuel}/m_{ox})_{st}$) and is calculated through equation 2.2.

$$(m_{air}/m_{fuel})_{st} = \frac{(x + y/4)(M_{O2} + 3.76M_{N2})}{M_{fuel}} \quad (2.1)$$

$$\varphi = \frac{(m_{fuel}/m_{ox})}{(m_{fuel}/m_{ox})_{st}} \quad (2.2)$$

Combustion takes place in the fuel-lean condition when the equivalence ratio is less than 1 (φ<1), i.e., when the oxidant amount is greater than the theoretical oxidant amount required to burn the entire fuel. When the oxidant amount is less than the theoretical oxidant amount, the combustion occurs in the fuel-rich condition, i.e., for equivalence ratio greater than 1 (φ>1).

The wide burners range made it necessary to classify the burner according to the combustion type. Currently, there are three criteria to classify the combustion regime, which are [9]:

i. the way that air and fuel mixture reach the combustion zone;
ii. fluid flow regime of the mixture;

iii. flame stability.

Criterion (i) is the main parameter that defines the combustion regime and classifies combustion as being premixed, non-premixed or diffusion and partially premixed. These three flame conditions will be explained in the following paragraphs.

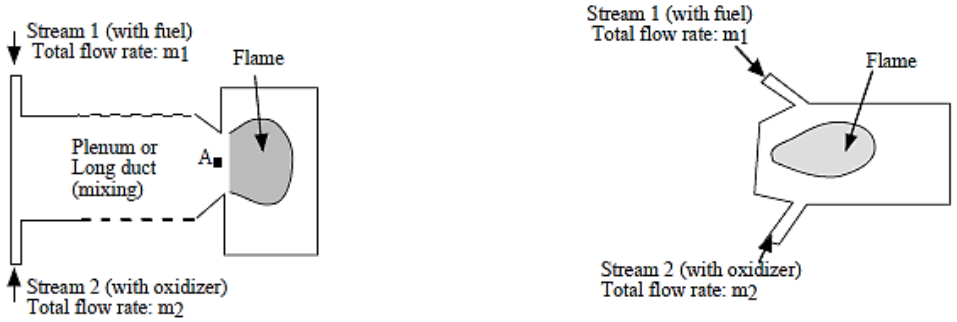

a) **b)**

Figure 2.1 – Classification of combustion regimes in function of reactant inlets in reaction zone. a) Premixed combustion, b) non premixed or diffusion combustion.(Adapted from [9])

In the premixed combustion, the fuel and oxidizer are perfectly mixed before reaching the reaction zone, see figure 2.1 a). The premixed flame propagation is done by the diffusion and reaction mechanisms in the direction of the fresh mixture [9]. The heat produced from the exothermic reactions is used to preheat the reactants through diffusion until the chemical reaction occurs.

Non-premixed combustion occurs when the reactants are introduced into the reaction zone separately, see figure 2.1 b). This type of combustion makes it possible to build simple and safe burners since the flame does not propagate towards the fuel stream due to the oxidizer absence. In the premixed and non-premixed flames, turbulence improves the combustion process [9]. When the fuel and oxidizer jets are turbulent, the flame length remains constant regardless of the fuel jet velocity increase when it is discharged into ambient air. If the mass flow rates are large, they can lead to the appearance of lifted flames and then to blow-off or flame quenching.

The premixed combustion efficiency is higher than non-premixed combustion because in the diffusion flame the reactant and oxidizer need to mix before combustion occurs through molecular diffusion mechanisms [9]. However, it is easier to control the flue gases temperature and emissions in non-premixed flames than in premixed flames.

A partially premixed flame is a hybrid flame in that it has characteristics of a diffusion flame as well as a premixed flame [9]. The diffusion and premixed flames have only one reaction zone whereas a partially premixed flame can have two or more reaction zones. When a flame has two reaction zones, it means that it has a premixed reaction zone on the fuel side and a non-premixed reaction zone on the oxidant side. A flame with two reaction zones is called a double flame. A triple flame is a flame with three reaction zones, i.e., two premixed reaction zones, one is fuel-rich and the other is fuel-lean, the third reaction zone is non-premixed. These reaction zones are spatially separated but are synergistically linked

through thermochemical and fluid dynamics interactions between them. Each zone depends on the other reaction zones which makes the flame structure strongly dependent on these zones [10].

Criterion (ii) indicates if the flow is laminar or turbulent through the Reynolds number. The Reynolds number, Re, is a dimensionless parameter that defines the ratio between the inertia forces and the viscous forces, see equation 2.3. The constants ρ, U, L and μ represent the fluid density, fluid velocity, the reference length and the dynamic viscosity of the fluid.

$$Re = \frac{\rho U L}{\mu} \tag{2.3}$$

Most applications occur in turbulent regime because the turbulence improves the combustion intensity and allows the design of small burners. Table 2.1 indicates some practical examples of combustion system where combustion can be premixed or non-premixed and the fluid flow regime applied. Criterion (iii) classifies whether the combustion is stable or unstable based on thermodiffusive instabilities and thermoacoustic instabilities.

Table 2.1 - Some examples of practical combustion systems in terms of premixed/ non premixed flame and laminar/ turbulent flow field. [9]

Flow / Flame	Premixed	Non-Premixed
Laminar	Bunsen burner	Lighter
	Domestic cooker	Candle
Turbulent	Gas turbines	Industrial furnaces
	Spark ignited Otto engines	Diesel engines, rockets

The presence of thermodiffusion instabilities depends on the mass diffusivity of the limitant reactant and the thermal diffusivity of the mixture in combustion. When the flame front is convex to the fresh mixture, the diffusion rate of the reactants in the flue gas is higher than the heating rate of the reactants which makes the local laminar flame speed greater than the speed of a planar flame front. If the diffusion rate of the reactants is lower than the heating rate, the local laminar flame speed is lower than the speed of a planar flame front and the flame front is concave to the fresh mixture. Whenever the local laminar flame speed is lower than the speed of a planar flame front, thermodiffusion instabilities can be neglected and stable combustion occurs [9]. The presence of these instabilities can be assessed through the Lewis number (Le). This dimensionless number is defined as the ratio between thermal diffusivity (α) and mass diffusivity (D^M), see equation 2.4. If the Lewis number is higher than the critical Lewis number which varies with the fuel used, the thermodiffusion instabilities may be neglected.

$$Le = \frac{\alpha}{D^M} \tag{2.4}$$

Thermoacoustic instability is a phenomenon that occurs due to the mutual interaction between acoustic waves and heat release oscillations of the flame. As the acoustic waves are created in the flame zone, they propagate and reflect in the combustion chamber which can compromise the combustion system operation [11]. These instabilities become dangerous when the velocity and pressure oscillations that occur inside the combustion chamber produce self-sustaining vibratory waves. These waves cause fatigue cycles in the combustion system elements and blow-off/flashback phenomena in the flame [11].

2.2 Flameless Combustion

In last decade of the 20th century, a group of researchers observed that for a certain air inlet temperature and velocity, the flame disappeared despite the continuous flue gas emission [5]. This group also found a significant NO_x emission reduction and an uniform O_2 concentration inside the combustion chamber[5].

Based on the experimental tests, the researchers [5] observed that the combustion reaction occurred uniformly throughout the furnace, the temperature distribution was uniform, the radiative heat transfer increased by 30% and there was noise decrease in the combustion process. With these characteristics, the researchers were able to create a new technology that improves the combustion system thermal efficiency and simultaneously decreases fuel consumption and NO_x emission [12]. This new technology, German researches have called flameless combustion or Flameless oxidation (FLOX) while Japanese researchers have called High Temperature Air Combustion (HiTAC). Later, new terms such as Moderate or Intense Low-oxygen Dilution combustion (MILD combustion) and Colorless Distribution Combustion (CDC) appeared.

However, there are slight differences between FLOX and CDC, and MILD combustion with HiTAC. In the first set, CDC operates at high thermal intensity with very low residence time. In the latter set, HiTAC requires air inlet temperature above 1000 °C.

According to Cavaliere and de Joannon [13], for MILD combustion to occur, the reactants must be preheated above the self-ignition temperature (T_{si}) of the fuel and the maximum temperature increase (ΔT) in the combustor must be less than the self-ignition temperature. The maximum temperature increase is the temperature difference between the maximum temperature recorded in the combustion chamber (T_{af}) and inlet temperature of the reactants (T_{in}). Flue gases must also be recirculated and entrained into the reaction zone to heat and dilute the air/fuel mixture. These conditions allow the maximum temperature inside the combustion chamber to be below the adiabatic flame temperature and the flame is no longer visible as shown in the figure 2.2.

Figure 2.2 - Transition from conventional combustion regime to flameless combustion regime (adapted from [14])

When one of the two above conditions is not respected, the mild combustion is no longer stable and may switch to other combustion mode or combustion does not happen, as shown in figure 2.3. If the mixture temperature and the maximum temperature increase are higher than the self-ignition temperature of the fuel, the mild combustion transits to high temperature combustion. If both conditions are lower than self-ignition temperature, there is piloted combustion. If the mixture temperature is lower than self-ignition temperature, but the maximum temperature increase is higher than self-ignition temperature, the feedback (conventional) combustion occurs [15].

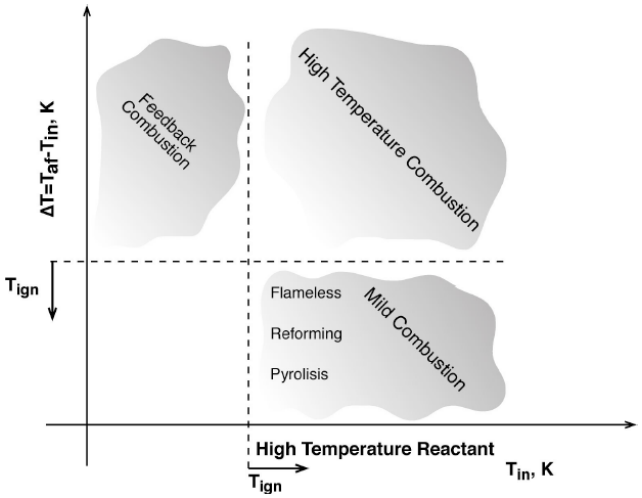

Figure 2.3 – Several types of combustion in function of temperatures [15]

As flameless combustion works according to the heat and flue gas recirculation principles since the flue gas recirculation promotes the heating of the reactants and the O_2 dilution at the local level, so there is a need to calculate the recirculation rate. Wunning and Wunning [12] defined the recirculation rate as the ratio of the internal flue gas recirculation mass flow rate ($\dot{m}_E$) to the sum of the fuel ($\dot{m}_{fuel}$) and air ($\dot{m}_{air}$) mass flow rates at the burner inlet, see equation 2.5. The mass flow rate of internal gas recirculation is the difference between the mass flow rate of the mixture of reactants with the flue gas ($\dot{m}_J$) and the fuel and air mass flow rates, see figure 2.4.

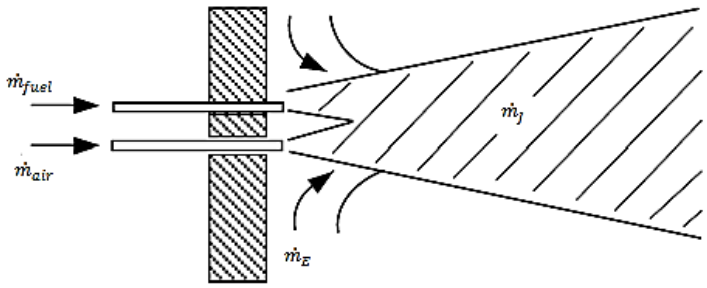

Figure 2.4 – Schematic representation of the different mass flows present in stable flameless combustion [12].

$$K_v = \frac{\dot{m}_E}{\dot{m}_{fuel} + \dot{m}_{air}} = \frac{\dot{m}_J - (\dot{m}_{fuel} + \dot{m}_{air})}{\dot{m}_{fuel} + \dot{m}_{air}} \tag{2.5}$$

Wunning and Wunning [12] established a relationship between the recirculation rate and the furnace temperature for the different combustion modes, as shown in figure 2.5. The authors observed that there is a critical value for K_v and furnace temperature to establish flameless combustion. However, these critical parameters vary with the type of burner and fuel used. To obtain methane flameless combustion, Wunning and Wunning [12] use a critical K_v value of 2.5 while Rebola *et al.* [16] use a K_v of 1.9. Hosseini *et al.* found that when using the same burner, the critical K_v for natural gas was 4.5 while in biogas the minimum K_v was 3 to obtain flameless combustion [17].

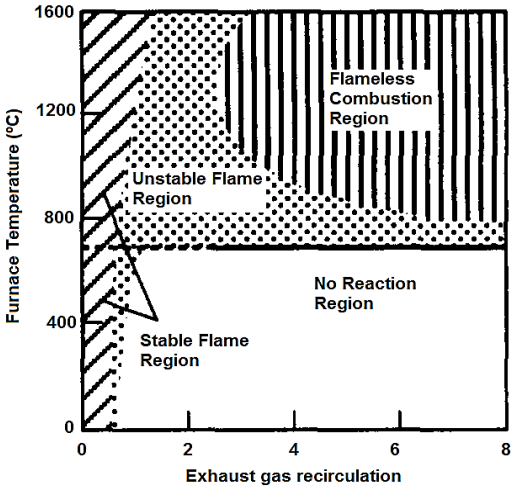

Figure 2.5 – The relationship between K_v and temperature in methane non-premixed combustion. (Adapted from [12])

Flameless combustion can also be done in non-premixed, premixed and partially premixed combustion mode. However, only the non-premixed and premixed combustion modes will be present.

Non-premixed MILD combustion requires that the fuel and air enter different channels in the combustion chamber. The air can be preheated or not as verified by Mi *et al.* [18]. If the air is not preheated, the air jet must have a Reynolds number high enough to compensate the velocity loss due to the viscosity effect. The conditions necessary to perform MILD combustion do not depend only on the local O_2 concentration, which should be less than 15 % by volume, and on the local temperature, but it also depends on the local velocity of mixture. MILD combustion can also occur in conditions where the temperature is high and the O_2 concentration and velocity of mixture are low. If the local velocity is higher than the flame propagation speed, the flame front will be suppressed, and the flameless combustion occurs even if the local O_2 concentration and temperature are high [5].

In flameless premixed combustion, the fuel and air are already perfectly mixed before entering the combustion chamber. However, the air is not preheated to high temperatures to avoid the risk of explosion inside the mixing chamber. As in the non-premixed mode, flameless combustion depends on the local O_2 concentration, the local temperature and the local velocity of mixture. In this combustion mode, the mixture jet velocity must be greater than the turbulent flame speed to allow the flue gases to be entrained to heat and dilute the reactants [5]. To obtain stable premixed flameless combustion, it is

necessary that the local O_2 concentration is greater than 15 % in volume, the local temperature is higher than the self-ignition temperature and the local velocity is higher than the flame propagation speed [5].

When the two combustion modes are compared, it is possible to observe that the premixed flameless combustion is easier to achieve and emits less CO and NO_x amount when compared to the CO and NO_x emissions of the non-premixed flameless combustion for the same temperature and reactant mass flow rate conditions [5].

Recent studies show that it is possible to use different gaseous fuels, but it is also possible to use liquid fuels, such as ethanol [19], octane and decane [20], and solid fuels, like coal [21] and solid biomass (rice husk) [22], to obtain flameless combustion.

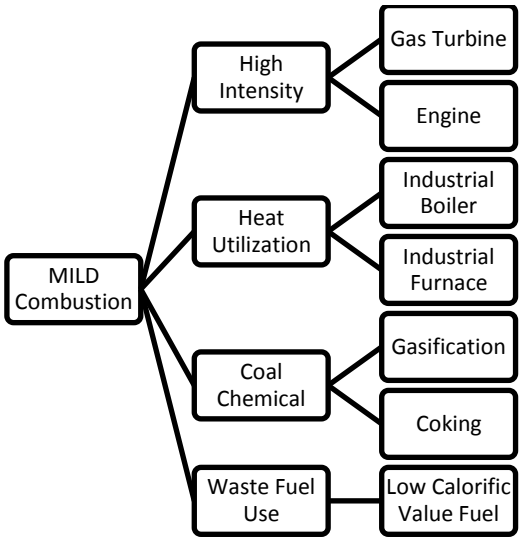

Figure 2.6 – Potential industrial applications of MILD combustion. (Adapted from [5])

The advantages of MILD combustion are improved combustion process efficiency, use of fuels with low calorific value, such as biogas and syngas, higher thermal efficiency, the temperature field homogeneity and reduced temperature gradients, which promote better control of the maximum temperature with beneficial effects on the combustor materials. The NO_x emissions are strongly reduced due to the lower maximum temperature, which is typically below 1800 K, suppressing the thermal NO_x formation mechanism. Soot formation is suppressed due to the significant flue gases recirculation, which promotes an O_2 concentration homogeneity inside the combustion chamber [23].

To conclude this section, figure 2.6 presents a set of potential industrial applications using this combustion technology. However, this technology is strongly used in ceramic and metallurgical industries as well as applied in industrial boilers [5].

2.3 Flameless combustion studies

The focus of this work is to study the non-premixed flameless combustion. Before presenting the various works carried out in this area, it is important to present the existing and studied diffusion burners for this combustion regime.

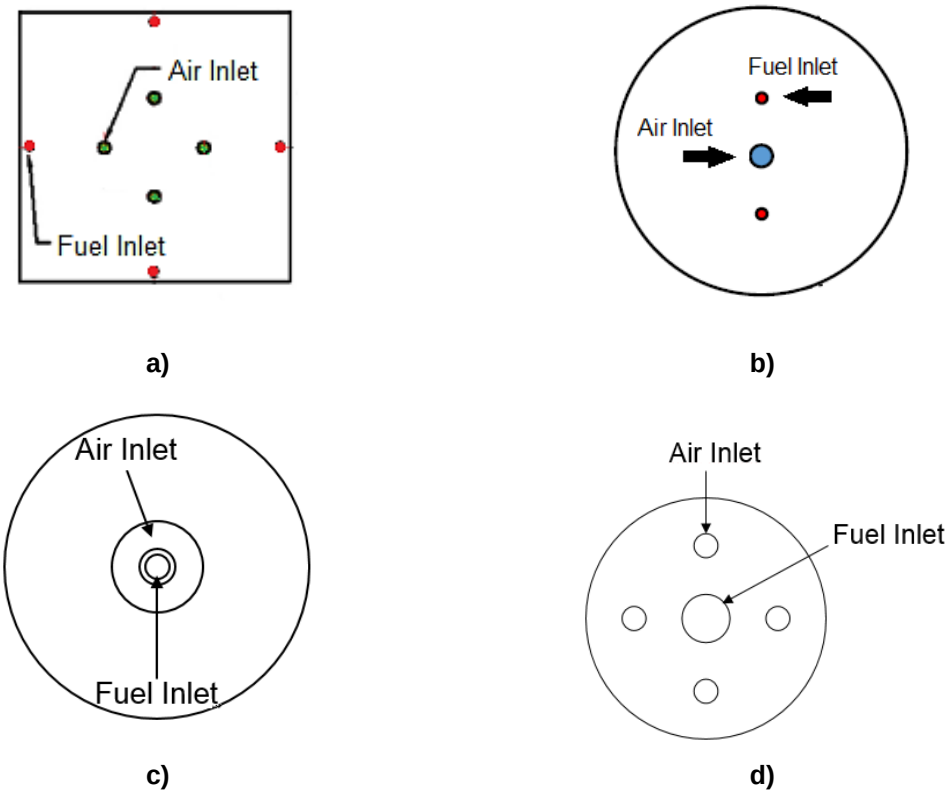

Figure 2.7 – Different burners used to study flameless non-premixed combustion.

So far, three different diffusion burner configurations have been used, whose geometric difference is the spatial arrangement of the nozzles for the fuel and oxidizer inlet. In this work, the burners will be called by type I, type II and type III burner. The type I burner consists of a radial distribution of two or more pairs of air and fuel inlet ports [24], see figure 2.7 a). The type II burner consists of a central oxidant inlet port and is surrounded by two or more fuel inlet ports distributed radially [25], see figure 2.7 b). Finally, the type III burner is very similar to the type II burner and consists of a central fuel inlet port surrounded by annular air inlet port [16], see figure 2.7 c). The type III burner can also have the following configuration: central fuel inlet port surrounded by two or more air inlet ports distributed radially around the fuel port [26], see figure 2.7d).

The next subsections present several studies performed in this area according to the fuel used.

2.3.1 Methane and natural gas

Galletti *et al.* [23] studied methane mild combustion in a type III burner and observed that when the burner works in mild combustion, NO_x emissions are 30 ppmv while in the flame mode the NO_x emissions are 1000 ppmv for the same operating conditions. The influence of the variation in the annular area of air inlet and the equivalence ratio were studied. When the air inlet area is reduced by half and for the same equivalence ratio, NOx emission decreases from 30 ppmv to 10 ppmv due to the air jet velocity increase, which improves the flue gases recirculation inside the combustion chamber [23]. But when the air inlet area remains constant and the equivalence ratio increases, there is a NO_x emission increase in an order of magnitude. The authors found that there is an improvement in thermal efficiency in flameless combustion when compared to the flame combustion mode [23]. With a similar burner and

the same fuel, Liu *et al.* [27] found that it is possible to perform mild combustion without preheating the reactants before entering the combustion chamber. To reach the auto-ignition temperature, the reactants are heated by flue gas dilution [27].

Rebola *et al.* [16] studied methane flameless combustion in a type III burner and found that it is possible to establish several operating conditions for the same combustion regime. The temperature, carbon monoxide and oxygen mole fractions fields are relatively uniform in comparison with conventional combustion. For different operating conditions, the maximum temperature inside the combustion chamber was less than 1500 ^{o}C and NO_x emission was independent of the operating conditions used [16]. The authors found also that CO and HC emissions, as well as thermal efficiency are strongly affected by the excess air coefficient used. In the type II burner, Veríssimo *et al.* [28] found that for low excess air coefficients, the reaction zone moves away from the burner and is uniformly distributed over a large volume of the combustion chamber and with smooth temperature gradients.

Karyeyen [29] studied the influence of the O_2 concentration in the oxidant and the oxidant inlet temperature for a type III burner with methane as the reference fuel. When the O_2 concentration decreases, the maximum temperature inside the combustion chamber decreases and promotes a more uniform temperature field [29]. The oxidant inlet temperature influences the temperature field uniformity, the maximum temperature obtained inside the combustion chamber and the flue gas temperature. When the oxidant inlet temperature increases, the temperature field is more uniform and the temperature difference between the maximum temperature and the flue gas temperature decreases [29]. So, the author concluded that there must be a favorable combination of these parameters to achieve near-zero CO and NO_x emissions and that the flameless combustion can be applied in gas turbines [29].

Castela *et al.* [30] studied the natural gas mild combustion in a type III burner and found that for a given air preheating temperature, the air jet velocity influences NOx emission, which decreases when the air jet velocity increases. The authors observed that for low air jet velocities, the burner works in conventional lean combustion mode and for high velocities the burner works in mild combustion [30]. The reaction zone in mild combustion is away from the burner and the temperature and species concentration gradients are smaller when compared to conventional lean combustion mode [30].

Huang *et al.* [26] studied the equivalence ratio influence in a type III burner and using natural gas as fuel. The researchers found that when the equivalence ratio decreases, the air jet velocity increases, which promotes higher entrainment of the flue gases inside the combustion chamber. The dilution rate increase promotes a shorter preheating time of the reactants to the auto-ignition temperature [26]. When the equivalence ratio increases, the mixing effect is less, which means that more time is needed to preheat the reactants and the reaction zone moves away from the burner and occupies a smaller volume of the combustion chamber, as can be seen in figure 2.8 [26]. The reaction zone location is determined by the OH radical concentration measured experimentally by chemiluminescence techniques.

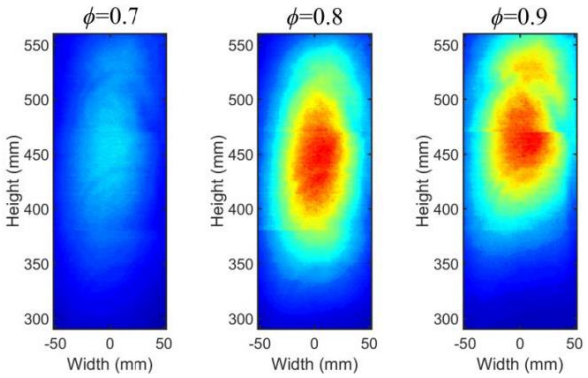

Figure 2.8 – Reaction zone location for different equivalence ratios through OH* chemiluminescence technique.[26]

Tu *et al.* [31] studied the influence of the combustion chamber shape to obtain mild combustion using a type II burner and natural gas. The researchers studied the effect of variation of the angle between the burner base and the combustion chamber wall. The study was carried out keeping constant the thermal power, equivalence ratio and the reactant temperature. The authors found that when the angle increases, the flue gas recirculation rate increases which leads to lower peak temperatures and low NO_x emissions [31]. For angles less than 85º, the combustion became unstable for the air and fuel jet conditions used, to ensure stable mild combustion it was necessary to increase the air and fuel jet velocities [31].

Later, Tu *et al.* [32] studied methane flameless combustion in oxy-fuel conditions. The three atmospheres studied in the oxidant were O_2/N_2, O_2/CO_2 and O_2/H_2O. The peak temperatures are higher in O_2/N_2 atmosphere than in O_2/CO_2 and O_2/H_2O atmospheres. The CO_2 atmosphere has lower peak temperatures since CO_2 has a higher capacity to heat absorption than N_2 and H_2O. The flameless combustion was established for the three atmospheres, but the CO_2 atmosphere showed a wider heat distribution and a thicker reaction zone [32]. The authors found that regardless of the atmosphere applied in flameless combustion, the CH_4 consumption route is given by: $CH_4 \rightarrow CH_3 \rightarrow CH_2O \rightarrow HCO \rightarrow CO \rightarrow CO_2$ [32].

2.3.2 Propane

Sorrentino *et al.* [33] developed a cyclonic burner to study the non-premixed flameless combustion of propane, see figure 2.9. The authors observed that to obtain flameless combustion, it is necessary that the air and fuel inlet temperatures are higher than 920 K and the C/O ratio influences the combustion stability. Based on these parameters, the researchers concluded that for each temperature value there is a C/O ratio range to establish stable flameless combustion [33].

Later, Sorrentino *et al.* [34] studied the influence of the equivalence ratio, dilution level in N_2 and the residence time of gases, *i.e.,* the air and fuel jet velocities. Based on these parameters, the authors concluded that there is a range of the equivalence ratio, dilution level and residence time in which stable flameless combustion can be achieved with CO and NO_x emissions below 10 ppm [34].

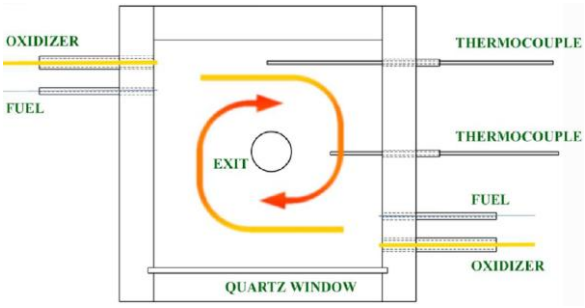

Figure 2.9 – A sketch of cyclonic combustion chamber [34].

Cheong *et al.* [25] studied the influence of the radial length between the central oxidant inlet port and the fuel inlet ports. The authors observed that stable flameless combustion occurs for different equivalence ratios and also for different radial distances with the fuel and air inlet temperatures equal to ambient temperature [25]. However, when the radial length increases, the equivalence ratio range decreases to form stable flameless combustion [25].

Later, Cheong *et al.* [35] also studied propane flameless combustion in a premixed burner. The authors observed that this regime was stable for a certain equivalence ratio and it was possible to establish flameless combustion in the stoichiometric condition for the flue gas recirculation rate above 2.5 [35]. The CO emission was practically undetectable for fuel-lean conditions and the NO_x emission was below 50 ppm in all tested conditions [35]. The authors found that the prompt-NO and NO-reburning mechanism are important and that the N_2O-intermediate mechanism prevails in lean conditions while the thermal-NO mechanism prevails at temperatures above 1600 K [35].

2.3.3 Acetylene

Acetylene (C_2H_2) is an intermediate species during combustion and is one of the most important precursors of soot formation. Its application is limited to welding processes due to the high adiabatic flame temperature and heating value essential to proceed with localized fusion and respective union of two metal alloys. However, the acetylene combustion has proved to be an area of little interest in the academic community, but acetylene has been extensively studied to understand and deepen the knowledge on soot formation. Based on the available information, some studies on acetylene combustion are summarized.

Alzueta *et al.* [36] studied experimentally and numerically the acetylene oxidation phenomenon for a range of temperatures and equivalence ratios in a flow reactor. The authors observed that the C_2H_2 conversion pathway is approximately the same independent of the stoichiometry. They also found that the C_2H_2 concentration decreases significantly when the equivalence ratio decreases, which is accompanied by an increase in CO and CO_2 concentrations [36]. This phenomenon happens because the main reaction of C_2H_2 conversion occurs due to the recombination of C_2H_2 with the O radical.

Shen *et al.* [37] studied the effect of CO_2 and H_2O dilution in C_2H_2/air premixed flames. The authors observed that the CO_2 dilution in the mixture does not influence the preference path of C_2H_2 consumption, the main consumption reaction is the same as that Alzueta *et al.* [36] verified. The CO_2

present in the mixture is used as a third body in certain chemical reactions and the laminar flame speed is less sensitive in the presence of CO_2 in the mixture than H_2O in the mixture. The authors observed that the H_2O addition favors the production of OH radicals instead of O radicals, which promotes a lower C_2H_2 consumption rate and in turn a lower laminar flame speed [37].

Xu *et al.* [38] studied the soot formation through C_2H_2/air diffusion flames and found that the soot formation starts in the presence of H radicals and ends when the C_2H_2 molar fraction is below 1%. The authors observed that the CO_2 and H_2O concentrations increase throughout the soot formation region. The maximum CO_2 and H_2O concentrations occur when the equivalence ratio is equal to one, i.e., close to the flame sheet, but the maximum CO concentration occurs upstream of the flame sheet [38].

Finally, Al-Hamamre and Tamin [39] studied the H_2 addition effect on the C_2H_2/ air premixed combustion. The authors observed that as the H_2 concentration in the mixture increases, the adiabatic flame temperature decreases and the laminar flame speed increases up to 90% of H_2 in the fuel, but for H_2 concentration above 90%, the laminar flame speed decreases [39]. The authors also found that the main C_2H_2 consumption pathway is the same described by Alzueta *et al.* [36], regardless of the H_2 concentration in the fuel and the equivalence ratio.

2.3.4 Biogas

Biogas can be used in conventional combustion like natural gas. However, the biogas characteristics are completely different from natural gas, which means that the control system, the fuel supply system and the burner have to be changed to proceed the biogas combustion. Furthermore, biogas upgrading for CO_2 elimination is a very expensive process. All these disadvantages can be eliminated using the flameless combustion mode since this mode allows to use low calorific fuels and the CO_2 removal is not necessary because CO_2 is used to dilute the oxidizer [40].

Hosseini *et al.* [40] studied biogas flameless combustion experimentally using a type III burner. The authors observed that the biogas flameless combustion efficiency is higher than in conventional combustion mode which corresponds to lower heat losses due to the reuse of the heat from the flue gases to heat the combustion air [40]. They observed that the temperature field is uniform inside the combustion chamber, the hot spots disappear and the thermal NO formation mechanism is suppressed [40]. The authors found that when the air inlet temperature and the excess air coefficient increase, the NO_x concentration increases [40].

Later, Hosseini *et al.* [17] simulated biogas flameless combustion and found that the furnace temperature must be above 1000 K to obtain flameless combustion. The authors observed that for an O_2 dilution higher than 15%, there is the appearance of a flame front, failing to respect the flameless combustion mode [17]. Regarding the NO_x formation mechanisms, they found that the NO-thermal mechanism is suppressed and N_2O-intermediate mechanism is responsible for the formation of NO_x. They concluded that the low temperatures in the combustion chamber are due to the fact that the CO_2 molecules have better heat absorption capacity compared to N_2 molecules [17]. This fact was also

observed by Colorado *et al.* [41] when they compared the biogas and natural gas flameless combustion in a similar burner.

Mameri *et al.* [42] studied the influence of the CO_2 and H_2 concentrations in the biogas composition to obtain flameless combustion in a burner with the opposed jet combustion configuration, see figure 2.10. The authors observed that for the same O_2 concentration in the oxidizer, the maximum temperatures are not sensitive with the CO_2 concentration in the fuel. However, the temperature increases as the H_2 concentration in fuel increases [42]. With respect to emissions, they found that the H_2O, CO and NO emissions decrease when the CO_2 concentration in fuel increases [42].

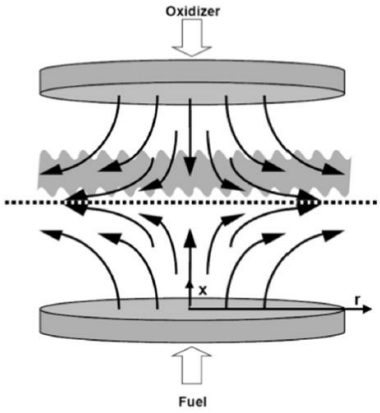

Figure 2.10 – Combustor with opposing air and fuel jet configuration.[42]

2.3.5 Ethanol

Ethanol is a form of renewable energy produced from the fermentation of sugar cane, sugar beets, switch grass, corn and barley. Ethanol has been presented as an alternative to gasoline in internal combustion engines. However, ethanol needs to be mixed with gasoline in order to avoid accelerated corrosion in the fuel supply systems in the car due to its acidity.

Azevedo *et al.* [43] studied the ethanol flameless combustion in a type III burner where the fuel was injected in a liquid state through a blurry injector. The authors observed that the auto-ignition temperature varies according to the thermal input and equivalence ratio used. The flameless combustion of liquid fuels occurs when the spray is formed, followed by its vaporization and mixed with the combustion air and the flue gases. In this combustion mode, the droplet vaporization time is longer when compared to conventional combustion [43]. They found that the decrease in the equivalence ratio leads to an increase in air velocity and momentum, which promotes better flue gas drag and recirculation [43]. This improves the air and fuel mixture in order to decrease the oxygen concentration in the reaction zone, which is decisive for the flameless combustion establishment [43]. The conventional combustion to flameless combustion transition, the authors observed a CO_2 emission increase and an unburned hydrocarbons, CO and NO_x emissions reduction and the responsible NO_x formation mechanism is intermediate N_2O-route mechanism [43].

Ye *et al.* [20] studied ethanol flameless combustion in which the ethanol was vaporized and transported in a stream of N_2 or air. The combustion chamber had a reverse-flow configuration where the flue gas

outlet and the reactant inlet were made on the same side and the burner applied was type III. They observed that ethanol flameless combustion can be achieved up to a pressure of 5 bar and the CO emission remains unchanged, but the NO_x emission increases with the pressure [20]. The authors studied the influence of air velocity and found that the NO_x emission decreases when the air velocity increases and the NO_x emission was less than 10 ppm for all studied equivalence ratios [20]. Regarding the use of N_2 or air as carrier gas, the authors reported that when the air is used as a carrier gas, the NO_x concentration is almost 3 times higher compared to the NO_x concentration obtained when N_2 is used as a carrier gas [20].

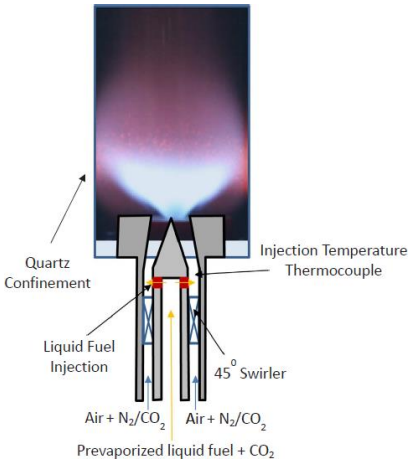

Figure 2.11 – Schematic of the swirl burner. [44]

Khalil and Gupta [44] studied the colorless distribution combustion (CDC) of ethanol and JP-8 pre-vaporized in a swirl burner, see figure 2.11, where the air and fuel inlet temperatures used were 700 K. The authors observed that the decrease in the O_2 concentration in the oxidant promotes a more uniform distribution of the OH radicals, which shows an enlarged reaction zone [44]. They also found that it is possible to obtain CDC of ethanol for lower O_2 concentration in relation to JP-8 due to the existence of oxygen in the ethanol composition [44]. In the flameless combustion of both fuels, the authors found a CO and NO_x emissions decrease, but ethanol emits less CO and NO_x emissions than JP-8 [44].

Zhu *et al.* [45] studied experimentally and numerically the influence of the inlet temperature of the co-flow gas, as well as, the O_2 concentration in the co-flow gas to obtain ethanol flameless combustion for a type III burner. They found that flameless combustion occurs for a restricted temperature and O_2 concentration ranges in the co-flow gas. The temperature field uniformity improves when a co-flow temperature is fixed and the O_2 concentration decreases in comparison with the temperature field uniformity for a fixed O_2 concentration and the inlet temperature increases [45]. The authors also observed that for low O_2 concentrations, processes such as secondary cracking and soot formation can also occur beyond the combustion [45].

2.3.6 Syngas

The syngas or synthetic gas consists mainly of hydrogen, carbon monoxide and often carbon dioxide. The syngas composition varies depending on the feedstock, such as natural gas, coal and biomass, and the amount of O_2 and H_2O used during the gasification process. As in biogas, syngas needs to be cleaned to remove compounds containing sulfur and nitrogen and some particulate matter in order to be safely burned or used as raw material in several chemical processes [46].

Huang *et al.* [24] studied the influence of air preheating temperature for various equivalence ratios to obtain syngas flameless combustion in a type I burner. The air preheating temperatures used were 293 K and 573 K and the critical equivalence ratio for flameless combustion establishment is 0.49 for both temperatures [24]. The authors observed that when the air preheating temperature increases, the NO_x emission increases, but CO emission decreases. Regarding the equivalence ratio influence, the NO_x and CO emissions have the same behavior observed in the air preheating temperature increase [24]. They concluded that the responsible NO_x formation mechanisms are the thermal-NO and N_2O-intermediate mechanisms [24].

Later, Huang *et al.* [47] studied the influence of spatial arrangement of air and fuel nozzles. The four configurations studied were: air and fuel injected at the base of the combustor (ABFB), air injected at the top and fuel injected at the base (ATFB), air injected at the base and fuel at the top (ABFT) and the air and fuel injected into the top of combustor (ATFT). The authors observed that the critical equivalence ratio is lower in the ABFB and ABFT configurations with $\varphi = 0.49$, then the ATFT configuration with $\varphi = 0.52$ and, finally, the ATFB configuration with $\varphi = 0.60$ [47]. They found that for the same equivalence ratio, parallel flow configurations emit less NO_x and CO than counter-flow configurations [47].

Ming *et al.* [48] studied the influence of the fuel jet velocity in the syngas flameless combustion of a type III burner. They found that the mixture between the oxidizer and fuel is better when the fuel jet velocity increases. The oxidizer used is a mixture of flue gases from the first combustion chamber with air that enters the second combustion chamber where flameless combustion occurs [48]. The authors observed that when the fuel jet velocity increases, there is an increase of flame lift-off distance, the flame temperature decreases, the thermal field is more uniform and NO_x emission decreases, but there is an increase in head loss and CO emission [48].

Mardani *et al.* [49] studied the flameless combustion of syngas and a H_2/CH_4 mixture for different H_2 concentrations, different Reynolds numbers and O_2 concentrations in the oxidizer for a type III burner. The authors found that the H_2 concentration increase in the mixture leads to the appearance of high temperature regions because there is a higher H_2O emission instead of CO_2, and H_2O has a lower capacity to absorb heat compared to CO_2 [49]. The O_2 concentration decrease in the oxidant leads to the peak temperatures decrease and a reaction zone growth. These changes are more intense in the H_2/CH_4 mixture compared to syngas [49]. The authors observed that the syngas is less sensitive to the variation in the Reynolds number compared to the H_2/CH_4 mixture and for the same H_2 concentration in syngas and H_2/CH_4 mixture, the heat release rate is higher in the H_2/CH_4 mixture [49].

2.3.7 Hydrogen

The use of hydrogen is considered an alternative to the use of fossil fuels because it does not emit CO_2, CO, unburned hydrocarbons and matter particulate, only emits NO_x and H_2O. Hydrogen is a fuel with a high lower heating value, laminar flame speed and adiabatic flame temperature compared to traditional gaseous fuels. The adiabatic flame temperature of H_2 is above 2400 K which promotes the NO formation through the thermal mechanism. The use of H_2 in conventional combustion processes has been limited due to the environmental restrictions that exist in relation to NO_x emissions. To overcome this limitation, some authors have shown an interest in burning H_2 in its pure state or mixed with CH_4 in the flameless combustion mode.

Yu *et al.* [50] numerically studied flameless combustion for four mixtures of H_2/CH_4 with the following compositions: 40%H_2/60%CH_4 (by volume), 60%H_2/40%CH_4, 80%H_2/20%CH_4 and pure H_2. The simulations were performed in the perfect stirred reactor (PSR) network. The NO_x emission was calculated using the Zeldovich mechanism and the excess air coefficient was the same for all tested mixtures, $\lambda = 1.1$. The results show that NO_x emission is less than 30 ppmv and CO emission is below 50 ppmv. The CO emission tends to decrease to zero as the H_2 concentration increases in the mixture. The authors observed that the NO_x emission is not sensitive to the H_2 concentration in the fuel despite the peak temperatures increase with the H_2 concentration. This independence is related to the flue gases recirculation, which promotes the NO-reburning mechanism [50].

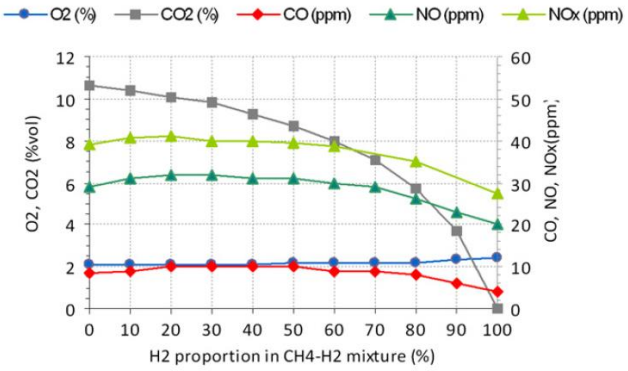

Figure 2.12 – Evolution of flue gas composition versus H_2 proportion in the fuel for T_{air} = 585 ºC and $\lambda = 1.11$.[51]

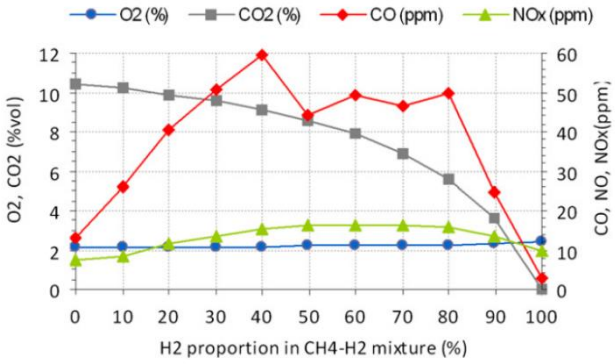

Figure 2.13 – Evolution of flue gas composition versus H_2 proportion in the fuel for T_{air} = 25 ºC and $\lambda = 1.11$.[51]

Ayoub *et al.* [51] experimentally studied flameless combustion of the H_2/CH_4 mixture for different H_2 concentration in a type II burner. The flameless combustion was achieved for all mixtures studied for the same thermal power, equivalence ratio and for two air preheating temperatures (T_{air} = 585 ºC and T_{air} = 25 ºC). Figures 2.12 and 2.13 show the CO, CO_2, O_2 and NO_x emissions on dry basis as a function of the H_2 concentration in the fuel for the two air preheating temperatures studied. The authors observed that the CO_2 and NO_x emissions decrease with the H_2 concentration increase in the fuel and they are not sensitive to the air preheating temperature used [51]. The O_2 emission is not sensitive to H_2 concentration in the fuel and the air preheating temperature. However, CO emissions are very sensitive to the air preheating temperature [51].

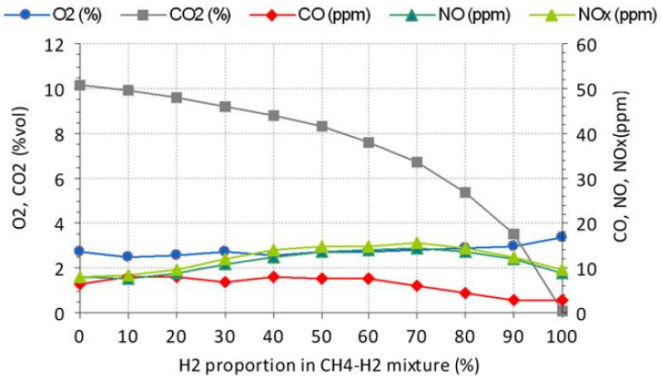

Figure 2.14 – Evolution of flue gas composition versus H_2 proportion in the fuel for T_{air} = 25 ºC and λ = 1.14.[51]

To control CO emissions, the authors increased the excess air coefficient from 1.11 to 1.14 in such a way that the CO emissions are below 10 ppm as shown in figure 2.14. The authors found that for lower H_2 concentration, the main NO_x formation mechanism is the thermal mechanism since H_2 has higher diffusivity and reactivity than CH_4, which promotes higher release of local heat in the reaction zone and the reaction zone tends to approach the burner [51]. For H_2 concentration above 70%, the NO_x concentration decrease is not sensitive to the reaction zone location, but to the carbon species concentration in the fuel, since the prompt-NO mechanism no longer prevails until it is suppressed in the pure H_2 combustion [51].

Nikakhtar and Akbari [52] simulated flameless combustion of pure H_2 in a gas turbine using a PSR and plug flow reactor (PFR) network. They studied the influence of the operating pressure, equivalence ratio, air preheating temperature and the flue gas recirculation rate. The authors found that the temperature gradients in the combustion chamber decrease and the NO_x emission increases when the pressure increases, but for pressures higher than 3 atm, the temperature gradients remain constant [52]. In relation to the air preheating temperature, the flameless combustion no longer occurs for air inlet temperatures above 800 K and the NO_x emission increases with the temperature increase [52]. The authors observed that the flue gas temperature is not sensitive to the flue gas recirculation rate, but the temperature field becomes more uniform when the recirculation rate increases. Furthermore, they found that there is a significant NO_x emission increase when the equivalence ratio increases [52]. Of the three studied parameters, the NO_x concentration is very sensitive to the equivalence ratio and there is a critical φ value for which flameless combustion does not occur [52].

2.3.8 Ammonia

The use of ammonia (NH_3) as a carbon-free fuel has been extensively studied experimentally and numerically in premixed and non-premixed combustion with methane and hydrogen. In this section, some work performed in non-premixed combustion will be presented.

Lee *et al.* [53] studied the stability limits of non-premixed combustion of NH_3/H_2 with air. The authors observed that the blow-off limits, the maximum flame temperature and the light radicals concentration, such as OH and H, decrease when the NH_3 concentration in the fuel increases. This reduction happens because the NH_3 is less reactive than H_2. However, the authors found that NO_x concentration increases when the NH_3 concentration in the fuel increases due to the presence of nitrogen in the fuel.

Um *et al.* [54] studied the stability limits of non-premixed combustion of NH_3 /H_2 up to 30% of NH_3 in the mixture. The tests were performed on a type III burner and the fuel and air were at atmospheric pressure and ambient temperature. Regarding the flame stability, the authors observed that the flame stability is compromised when the NH_3 concentration in the fuel increases. They also observed that for a fuel Reynolds number of 7500, the flame has a partial extinction and reignition behavior [54]. At the flame structure level, they found that the NH_3 consumption occurs in regions away from the burner, compared to the location of H_2 consumption regions. This phenomenon occurs because the H_2 has higher diffusivity and reactivity than NH_3 [54]. Regarding NO_x emissions, the authors observed that when the NH_3 concentration increases, the NO_x concentration increases smoothly and decreases with the air jet velocity increase. However, the NO_x concentration increases with the fuel jet velocity increase [54].

Li *et al.* [55] developed a reduced kinetic mechanism for combustion of the $NH_3/CH_4/H_2$ mixture. After validating the mechanism under premixed combustion conditions, the authors tested this mechanism under non-premixed combustion using the experimental data available in literature for CH_4/H_2 flameless combustion in a type III burner [56]. The authors observed that the radial profiles of temperature and species concentration had a good agreement with the experimental data obtained for the CH_4/H_2 flameless combustion [55]. In that work, the authors studied four $CH_4/H_2/NH_3$ mixtures presented in table 2.1. The authors found that the mixture with 65% NH_3 presented blow-off conditions due to the lower reactivity of this species when compared to methane and hydrogen and the longer ignition delay times.

Table 2.2 – Mass composition of the studied mixtures. [55]

Mixture	Y_{CH4}	Y_{H2}	Y_{NH3}
M1	0.872	0.109	0.019
M2	0.808	0.101	0.091
M3	0.604	0.075	0.321
M4	0.308	0.038	0.654

Figure 2.15 shows the contours of N_2O and NO emissions from the combustion chamber for mixtures M1, M2 and M3. The authors found that the NH_3 addition in the mixture increases the N_2O and NO concentrations. The N_2O formation occurs in rich fuel regions and away from the burner, while the NO

formation occurs in regions of higher temperatures and stoichiometric nature. Mixture M3 has a lower NO concentration when compared to mixture M1. This NO reduction is due to the fact that NH_3 behaves as a NO reducing agent according to the selective non-catalytic reduction (SNCR) principle where NH_3 is decomposed in NH_2 which subsequently reacts with NO to produce H_2O and N_2.

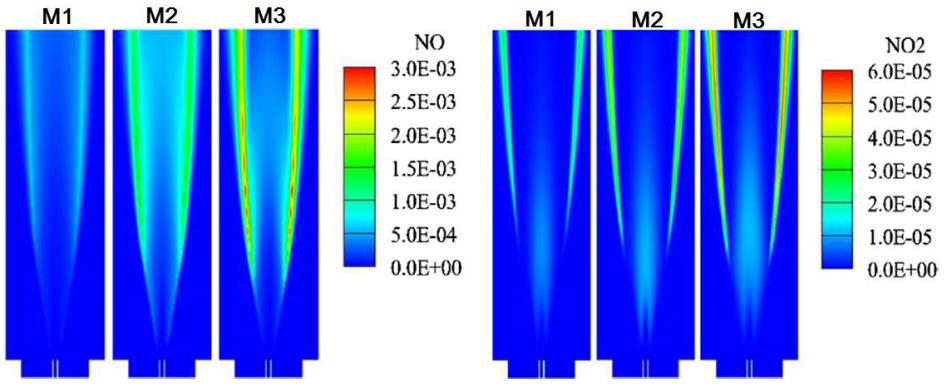

Figure 2.15 – Mass fraction of NO and NO_2 contours for the mixtures M1, M2 and M3. [55]

Sorrentino *et al.* [57] were the pioneers in obtaining experimentally the ammonia flameless combustion in a combustor represented in figure 2.9. The authors studied the influence of air preheating temperature, thermal input and equivalence ratio. They observed that the maximum temperature inside the combustion chamber occurs in the stoichiometric condition and that the peak temperature increases with the air inlet temperature increase, but the difference between these two temperatures decreases [57]. Regarding emissions, the authors found that the NO_x concentration increases with air preheating temperature and the excess air coefficient, but NH_3 and H_2 concentrations are above 1000 ppm when combustion takes place in fuel-rich conditions [57]. The low NO_x concentration and high NH_3 and H_2 concentration in fuel-rich conditions are due to the recombination of the NH_2 and N_2H_2 radicals with NO [57]. According the authors, the NO_x emission increase is directly proportional to the thermal input increase for any equivalence ratio used [57].

2.4 Numerical Simulation of Flameless Combustion

In this section, the turbulence models, the combustion models and the kinetic mechanism used by authors to study flameless combustion for different fuels will be presented.

In the context of flameless combustion simulation, Christo and Dally [58] studied the best turbulence and combustion model to be applied in this combustion mode for a type III burner. The studied turbulence models were the standard k-ε model (SKE), realizable k-ε model (RKE), renormalization group k-ε model (RNG) and a modified version of the standard k-ε model that consists of replacing the value of the constant $C_{\varepsilon 1}$ = 1.44 to 1.6. Based on the studied turbulence models, they found that the numerical results produced using the modified SKE model showed an excellent agreement with the experimental results [58]. Regarding combustion models, the studied models were: the mixture fraction/ probability density function model (ε/PDF), flamelet model, eddy dissipation model with finite-rate chemistry (EDM/FR) and eddy dissipation concept model (EDC). Of the four models studied, the authors found that single conserved scalar-based models (ε/PDF and flamelet models) are the most

inappropriate for this combustion mode followed by the EDM/FR model, the EDC model is more accurate in results when using detailed kinetic mechanisms instead of the skeletal kinetic mechanism [58]. Like Christo and Dally, Rebola *et al.* [59] studied which turbulence and combustion models should be applied to simulate flameless combustion in a type III burner. The authors concluded that the combination of the EDC and SKE models provides the best results [58].

Lupant *et al.* [60] also studied the application of the EDM/FR and EDC models to perform flameless combustion simulations for a type II burner. The authors found that the EDC model provides good results in the temperatures and species fields when compared to experimental results and this model can capture the kinetic limitation impact due to dilution [60]. However, the reaction delay time is underestimated, which means that the predicted reaction zone location may not coincide with experimental data [60].

Parente *et al.* [61] also studied which of the EDM/FR and EDC combustion models provided the best agreement with the experimental results obtained in a flameless combustion regime for type III burner. The authors concluded that the EDC model application is the one that establishes the best agreement with the experimental data [61]. Tabacco *et al.* [62] also concluded that the EDC model provides good numerical results when compared to the experimental data of a type III burner. In this case, the authors also found that RKE model has a better performance than the SKE model. These authors suggest that to improve the accuracy of the EDC model results, it is necessary to change the C_τ and C_ε constants [62]. This suggestion is also indicated by De *et al.* [63], in which they observed an improvement in the convergence of the experimental results to the numerical ones for axial distances close to the burner. However, there is a temperature overestimation for higher axial distances [63].

The use of the EDC model to simulate flameless combustion has been accepted by the entire scientific community as the best combustion model so far. In relation to the turbulence models, it seems that the model applied differs from burner to burner and also for the same type of burner. The works of Christo and Dally [58], Rebola *et al.* [59], Parente *et al.* [61] and Tabacco *et al.* [62] have in common the fact that the burner consists of a central fuel inlet port surrounded by an annular section for the air inlet. However, the turbulence model applied was different according to the operating conditions and the geometric characteristics of the burner.

To close this section and chapter, the turbulence, combustion, and radiation models employed in previous studies will be presented in table form, as well as the kinetic mechanism and studied parameters of the numerical works presented in section 2.3, see table 2.2.

Table 2.3 – The models and kinetic mechanism used to study the flameless combustion of different fuels.

Authors	Fuel	Turbulence Model	Combustion Model	Radiation Model	Kinetic Mechanism	Studied parameters
Galletti *et al.* [23]	CH_4	Modified SKE	EDM/FR	Discrete Ordinates method (DO) + weighted sum of gray gases model (WSGG)	Simple one-step global mechanism	• air inlet velocity • air excess coefficient • turbulence – chemistry iterations • burner efficiency
Liu *et al.* [27]	CH_4	Modified SKE	EDC	DO + WSGG	GRI-Mech 3.0 [64]	• mild combustion establishment without air preheated
Verissimo *et al. [65]*	CH_4	RKE	EDC	DO + WSGG	Skeletal mechanism [66]	• influence of the air preheating temperature
Karyeyen *et al.* [29]	CH_4	SKE	β-function PDF	P1-model	Not specified	• Oxygen concentration • Equivalence ratio • Inlet temperature
Huang *et al.* [26]	Natural gas	K – ε model	Flamelet model with β-function PDF	P1 model	Not specified	• Equivalence ratio • Dilution rate
Tu *et al.* [31]	CH_4	SKE	EDC	P1 model + WSGG	5 – step global reaction mechanism	• Combustion chamber shape

Tu *et al.* [32]	CH_4	Modifed SKE	EDC	DO + WSGG	GRI – Mech 3.0 [64]	• Establishment of flameless combustion mode in oxy-fuel conditions
Cheong *et al.* *[35]*	C_3H_8	SKE	EDC	DO + WSGG	reduced reaction mechanism of propane [67]	• Establishment of premixed flameless combustion
Cheong *et al.* [25]	C_3H_8	SKE	EDC	DO + WSGG	reduced reaction mechanism of propane [67]	• Compare experimental results with numerical results
Huang *et al.* *[48]*	Syngas	RKE	EDC	DO + WSGG	GRI – Mech 3.0 [64]	• Air preheated temperature
Mardani *et al.* *[49]*	Syngas and H_2/CH_4	Modified SKE	EDC	Radiation was not considered	GRi – Mech 3.0 [64] DRM – 22 [68]	• Effect of H2 in fuel
Hosseini *et al.* [17]	Biogas	SKE	EDM/FR	DO + WSGG	Two-step chemical kinetic mechanism	• Study the characteristics of biogas flameless combustion
Zhu *et al.* [45]	Ethanol	SKE	Steady laminar flamelet model	DO + WSGG	Marinov [69]	• Study the influence of co-flow gas temperature and O_2 concentration to obtain flameless combustion.

3. Mathematical Model

3.1 Introduction

This chapter describes the conservation equations of the reactive flow present inside the combustion chamber. Initially, the equation system used for reactive flows is presented, as described by Coelho and Costa [8], and then extended to turbulent flows. Thereafter, the turbulence, combustion and radiation models used in the present work are presented in detail.

3.2 Conservation Equations for Simple Reactive Systems

The principles of conservation of mass, momentum, energy and chemical species describe the physical phenomena associated with the combustion process. This section presents the equations associated with each principle stated above.

The mass conservation principle also known as the continuity equation is written as:

$$\frac{\partial \rho}{\partial t} + \frac{\partial (\rho u_j)}{\partial x_j} = 0 \tag{3.1}$$

where ρ represents the fluid density, t the time, the u_j represents the component in the j direction of the velocity vector and x_j is the position.

The mass conservation equation of the i-species is given by:

$$\frac{\partial (\rho y_i)}{\partial t} + \frac{\partial (\rho u_j y_i)}{\partial x_j} = -\frac{\partial j_{i,j}}{\partial x_j} + M_i \dot{\omega}_i \tag{3.2}$$

where y_i, M_i, $\dot{\omega}_i$ and $j_{i,j}$ are mass fraction, the molar weight, the net reaction rate of species i and the mass diffusion flux in the j direction of species i.

The mass diffusion flux is the sum of three effects, namely, the diffusion resulting from the concentration gradient of i-species, the thermal diffusion, also known as the Soret effect, and the diffusion caused by the pressure gradient. The effect associated with pressure can be neglected in most combustion processes as well as the Soret effect. Then the mass diffusion flux is approximated by Fick's law described in equation 3.3.

$$j_{i,j} = -\rho D_i^M \frac{dy_i}{dx_j} \tag{3.3}$$

where D_i^M is mean diffusion coefficient of species i in the mixture.

The momentum conservation equation has the following form:

$$\frac{\partial(\rho u_i)}{\partial t} + \frac{\partial}{\partial x_j}\left(\rho u_i u_j\right) = -\frac{\partial p}{\partial x_i} + \frac{\partial \tau_{ij}}{\partial x_j} + \rho g_i \tag{3.4}$$

where p is the pressure, g_i represents the gravitational acceleration in the i direction, μ is the dynamic viscosity of the fluid and τ_{ij} is viscous stress tensor given by:

$$\tau_{ij} = \mu\left(\frac{\partial u_i}{\partial x_j} + \frac{\partial u_j}{\partial x_i}\right) - \frac{2}{3}\mu\frac{\partial u_k}{\partial x_k}\delta_{ij} \tag{3.5}$$

where δ_{ij} is Kronecker's delta function, such that $\delta_{ij} = 1$ if i = j and $\delta_{ij} = 0$ if i ≠ j.

The energy conservation principle expressed in terms of specific enthalpy (h) is given by:

$$\frac{\partial(\rho h)}{\partial t} + \frac{\partial(\rho u_j h)}{\partial x_j} = \frac{\partial p}{\partial t} + u_j\frac{\partial p}{\partial x_j} + \tau_{ij}\frac{\partial u_i}{\partial x_j} - \frac{\partial j_{q,j}}{\partial x_j} + \dot{q}_R''' \tag{3.6}$$

where $\dot{q}_R'''$ is the heat exchange by radiation, per unit of volume and $j_{q,j}$ represents the component of the j direction of the heat flux vector. The heat flux vector has three contributions, namely, the heat flux derived from heat conduction, expressed by the Fourier law that corresponds to the first term of equation 3.7, the flux derived from the Dufour effect, this portion is neglected in combustion, and the flux caused by mass diffusion which corresponds to the second term of the equation.

$$j_{q,j} = -\frac{\lambda}{c_p}\frac{\partial h}{\partial x_j} + \sum_{i=1}^{N}\left(1 - \frac{1}{Le_i}\right)\frac{\lambda}{c_p}h_i\frac{\partial y_i}{\partial x_j} \tag{3.7}$$

where λ is the thermal conductivity, c_p is the specific heat and Le_i represents the Lewis number of species i. In most applications, viscous dissipation is neglected and the Lewis number varies little from species to species, being close to one for all chemical species. The pressure terms can also be neglected if the combustion process occurs at constant pressure and the viscous dissipation term is often neglected. In turbulent flows, it is assumed that Le number is one, so the heat flux is described by the Fourier law. If all these hypotheses are valid, the energy equation is simplified as follows:

$$\frac{\partial(\rho h)}{\partial t} + \frac{\partial(\rho u_j h)}{\partial x_j} = \frac{\partial}{\partial x_j}\left(\frac{\lambda}{c_p}\frac{\partial h}{\partial x_j}\right) + \dot{q}_R''' \tag{3.8}$$

3.3 Conservation Equations for Turbulent Reactive Systems

Turbulent flows are generally characterized by a fluid motion that becomes intrinsically unstable and unsteady, so that the final state of the fluid has a chaotic and random behavior, hence the need to use statistical methods to quantify the turbulent flow [70]. Despite this characteristic, there are other characteristics that define a turbulent flow which are: diffusivity, large Reynolds number, three-dimensional vorticity fluctuations, dissipation and continuity. The turbulent flows are diffusivity because the velocity fluctuations present in the fluid increase the momentum, heat and mass transfer rates [70]. Turbulent flow is always dissipative because the work done by viscous shear stresses increases the internal energy of the fluid at the expense of turbulent kinetic energy [70]. To compensate for these viscous losses, it is necessary to continuously supply energy to the fluid. As turbulence is a continuum phenomenon, the fluid mechanics equations are valid for this type of flow [70].

Even with existing advances in computational technologies, the random nature of fluid flow still excludes calculations based on the equations presented in the previous section with the required precision. Hence the use of statistical approaches to solve the equations that govern fluid mechanics. One of the approaches used is the Reynolds decomposition that solves the equations for the time average field of the dependent variables. The Reynolds decomposition defines that a scalar $\varphi(\vec{r},t)$ is the sum of an average time value $\bar{\varphi}(\vec{r})$ and a fluctuation $\varphi'(\vec{r},t)$.

$$\varphi(\vec{r},t) = \bar{\varphi}(\vec{r}) + \varphi'(\vec{r},t) \tag{3.9}$$

The time average value is defined as:

$$\bar{\varphi}(\vec{r}) = \lim_{\Delta t\to\infty} \frac{1}{\Delta t}\int_{t_0}^{t_0+\Delta t} \varphi(\vec{r},t)dt \tag{3.10}$$

where Δt is a large enough time interval exceeding the time scales of the slowest variations. While the average value of the fluctuation component is null, by definition:

$$\overline{\varphi'(\vec{r},t)} = \lim_{\Delta t\to\infty} \frac{1}{\Delta t}\int_{t_0}^{t_0+\Delta t} \varphi'(\vec{r},t)dt \equiv 0 \tag{3.11}$$

However, Reynolds decomposition does not account for variations in fluid density, which cannot be neglected in combustion processes due to the thermal expansion of gases described by Versteeg and Malalasekera [71]. So, the use of the Favre average approach is the desirable approach to solve these types of problems. As in the Reynolds decomposition, Favre decomposition defines a scalar $\varphi(\vec{r},t)$ as the sum of the mass-weighted average $\tilde{\varphi}(\vec{r})$ and a fluctuation $\varphi''(\vec{r},t)$.

$$\varphi(\vec{r},t) = \tilde{\varphi}(\vec{r}) + \varphi''(\vec{r},t) \tag{3.12}$$

In this case, the average component is defined as:

$$\tilde{\varphi}(\vec{r}) = \lim_{\Delta t \to \infty} \frac{1}{\bar{\rho}\Delta t} \int_{t_0}^{t_0+\Delta t} \bar{\rho}\varphi(\vec{r}, t)dt \tag{3.13}$$

In Favre decomposition, the mean fluctuation value is zero, but its mean time value is different from zero:

$$\widetilde{\varphi''(\vec{r}, t)} = 0 \tag{3.14}$$

$$\overline{\varphi''(\vec{r}, t)} \neq 0 \tag{3.15}$$

Note that:

$$\overline{\overline{\rho\, \varphi''(\vec{r}, t)}} = 0 \tag{3.16}$$

$$\overline{\overline{\rho\, \varphi(\vec{r}, t)}} = \bar{\rho}\tilde{\varphi}(\vec{r}) + \overline{\overline{\rho\, \varphi''(\vec{r}, t)}} \tag{3.17}$$

Based on equations 3.16 and 3.17, the mass-weighted average is a function of the time average value and is expressed as follows:

$$\tilde{\varphi}(\vec{r}) = \frac{\overline{\overline{\rho\, \varphi(\vec{r}, t)}}}{\bar{\rho}} \tag{3.18}$$

Based on equation 3.12, it is possible to substitute instantaneous density, velocities, enthalpy and other scalar properties by their mass-weighted mean values and fluctuation values in the governing equations, which are commonly known as Favre-Average Navier-Stokes equations and can be written as follows:

- Continuity equation

$$\frac{\partial \bar{\rho}}{\partial t} + \frac{\partial(\bar{\rho}\widetilde{u_j})}{\partial x_j} = 0 \tag{3.19}$$

- Momentum conservation equation

$$\frac{\partial(\bar{\rho}\widetilde{u_i})}{\partial t} + \frac{\partial}{\partial x_j}(\bar{\rho}\widetilde{u_i}\widetilde{u_j}) = -\frac{\partial \bar{p}}{\partial x_i} + \frac{\partial}{\partial x_j}\left[\mu\left(\frac{\partial \widetilde{u_i}}{\partial x_j} + \frac{\partial \widetilde{u_j}}{\partial x_i}\right) - \frac{2}{3}\mu\frac{\partial \widetilde{u_k}}{\partial x_k}\delta_{ij} - \bar{\rho}\widetilde{u''_i u''_j}\right] + \bar{\rho}g_i \tag{3.20}$$

- Energy conservation equation

$$\frac{\partial(\bar{\rho}\tilde{h})}{\partial t} + \frac{\partial(\bar{\rho}\widetilde{u_j}\tilde{h})}{\partial x_j} = \frac{\partial}{\partial x_j}\left(\overline{\frac{\lambda}{c_p}\frac{\partial h}{\partial x_j}} - \bar{\rho}\widetilde{u''_j h''}\right) + \overline{\dot{q}_R'''} \tag{3.21}$$

- Species mass conservation equation

$$\frac{\partial(\bar{\rho}\tilde{y}_i)}{\partial t} + \frac{\partial(\bar{\rho}\tilde{u}_j\tilde{y}_i)}{\partial x_j} = \frac{\partial}{\partial x_j}\left(\overline{\rho D_i^M \frac{dy_i}{dx_j}} - \bar{\rho}\widetilde{u''_j y''_i}\right) + M_i\overline{\dot{\omega}_i} \tag{3.22}$$

The Favre-Averaged Navier-Stokes equations contain new unknows and to close this equation system it is necessary to use turbulence, combustion and radiation models. The next sections of this chapter serve to present the turbulence, combustion and radiation models used to carry out this work.

3.4 Turbulence Models

The two-equation models use two transport equations for two turbulence properties in addition to mean-flow Navier-Stokes equations. Usually, the first transport equation is for turbulent kinetic energy (k), while the second equation can be used for a variety of turbulence properties that include: the dissipation rate of turbulence kinetic energy (ε), the specific dissipation rate (ω), the length scale (l), the product of k and l, the time scale (τ), the product of k and τ, among others. The two-equation models most used in industries and in many engineering problems are the k-ε and k-ω models [72].

In this work, the turbulence models used were standard k-ε model, realizable k-ε model and SST (Shear Stress Transport) k-ω model. These models will be described in the following sections.

3.4.1 Standard k-ε model

The standard k-ε model is very popular in industry flow and heat transfer simulations due to its robustness, economy and reasonable accuracy for a wide range of turbulent flows. It was proposed by Launder and Spalding [73]. This is a semi-empirical model since the transport equation for k is derived from mathematical correlations while the transport equation for ε is obtained through experiments [70], [74]. The transport equations for k and ε are defined as follows:

$$\frac{\partial}{\partial t}(\rho k) + \frac{\partial}{\partial x_i}(\rho k u_i) = \frac{\partial}{\partial x_j}\left[\left(\mu + \frac{\mu_t}{\sigma_k}\right)\frac{\partial k}{\partial x_j}\right] + G_k - \rho\varepsilon \tag{3.23}$$

$$\frac{\partial}{\partial t}(\rho \varepsilon) + \frac{\partial}{\partial x_i}(\rho \varepsilon u_i) = \frac{\partial}{\partial x_j}\left[\left(\mu + \frac{\mu_t}{\sigma_\varepsilon}\right)\frac{\partial \varepsilon}{\partial x_j}\right] + C_{1\varepsilon}\frac{\varepsilon}{k}\,G_k - C_{2\varepsilon}\rho\frac{\varepsilon^2}{k} \tag{3.24}$$

where G_k represents the generation of turbulence kinetic energy due to the mean velocity gradients and μ_t represents the turbulent viscosity. The $C_{1\varepsilon}$, $C_{2\varepsilon}$ are constants and σ_k and σ_ε represent the turbulent Prandtl numbers for k and ε.

The way in which the term G_k is calculated is valid for both standard and realizable k-ε models and is defined as:

$$G_k = -\rho\overline{u'_i u'_j}\frac{\partial u_j}{\partial x_i} \tag{3.25}$$

The turbulent viscosity is defined as follows:

$$\mu_t = \rho C_\mu \frac{k^2}{\varepsilon} \tag{3.26}$$

where C_μ is a constant. By definition, the parameters $C_{1\varepsilon}$, $C_{2\varepsilon}$, C_μ , σ_k and σ_ε, in the standard k-ε model, have the values of:

$C_{1\varepsilon} = 1.44$ $C_{2\varepsilon} = 1.92$ $C_\mu = 0.09$ $\sigma_k = 1.0$ $\sigma_\varepsilon = 1.3$

3.4.2 Realizable k-ε model

In the realizable k-ε model, the term realizable means that the model satisfies certain mathematical constraints on normal Reynolds stress, consistent with the physics of turbulent flows. This model ensures that the normal Reynolds stress is always positive and that Schwarz inequality ($\overline{u_i}\overline{u_j}^2 \leq \overline{u_i^2 u_j^2}$ for shear stresses are not violated even when the mean strain rate is high. The realizable k-ε model provides a new formula for calculating turbulent viscosity involving the C_μ variable and a new model equation for ε based on the dynamic equation of the mean-square vorticity fluctuation [70,74].

One of the limitations of this model is to produce turbulent viscosities with no physical significance in a computational domain that contains both rotating and stationary fluid zones. This is because the effects of mean rotation are included in the definition of turbulent viscosity [74].

The transport equation for turbulent kinetic energy in this model is similar to the equation applied in the standard k-ε model, see equation 3.23. The transport equation for ε is given by:

$$\frac{\partial}{\partial t}(\rho\varepsilon) + \frac{\partial}{\partial x_j}(\rho\varepsilon u_j) = \frac{\partial}{\partial x_j}\left[\left(\mu + \frac{\mu_t}{\sigma_\varepsilon}\right)\frac{\partial \varepsilon}{\partial x_j}\right] + \rho C_1 S\varepsilon - \rho C_2 \frac{\varepsilon^2}{k + \sqrt{v\varepsilon}} \tag{3.27}$$

where the constant C_1 is calculated as follows:

$$C_1 = \max\left\{0.43, \frac{\eta}{\eta+5}\right\}, \ \eta = S\frac{k}{\varepsilon} \tag{3.28}$$

where the term S is the modulus of the mean rate-of-strain tensor, defined as:

$$S = \sqrt{2S_{ij}S_{ij}} \tag{3.29}$$

The turbulent viscosity is calculated according to equation 3.26 in which the constant C_μ is calculated as follows:

$$C_\mu = \frac{1}{A_0 + A_S \frac{kU^*}{\varepsilon}} \tag{3.30}$$

where

$$U^* \equiv \sqrt{S_{ij}S_{ij} + \widetilde{\Omega}_{ij}\widetilde{\Omega}_{ij}} \tag{3.31}$$

$$\widetilde{\Omega}_{ij} = \Omega_{ij} - 2\varepsilon_{ijk}\omega_k \tag{3.32}$$

$$\Omega_{ij} = \overline{\Omega_{ij}} - \varepsilon_{ijk}\omega_k \tag{3.33}$$

The term $\overline{\Omega_{ij}}$ is the mean rate-of-rotation in a moving reference frame with the angular velocity ω_k. The constants A_0 and A_S are given by:

$$A_0 = 4.04,\ A_S = \sqrt{6}\,cos\varphi \tag{3.34}$$

where

$$\varphi = \frac{1}{3}\cos^{-1}(\sqrt{6}W) \tag{3.35}$$

$$W = \frac{S_{ij}S_{jk}S_{ki}}{\tilde{S}^3} \tag{3.36}$$

$$\tilde{S} = \sqrt{S_{ij}S_{ij}} \tag{3.37}$$

$$S_{ij} = \frac{1}{2}\left(\frac{\partial u_j}{\partial x_i} + \frac{\partial u_i}{\partial x_j}\right) \tag{3.38}$$

In the realizable k-ε model, the constants $C_{1\varepsilon}$, C_2, σ_k and σ_ε take the values of:

$$C_{1\varepsilon} = 1.44,\ C_2 = 1.9,\ \sigma_k = 1.0,\ \sigma_\varepsilon = 1.2$$

3.4.3 SST k-ω model

The Shear Stress Transport (SST) k-ω model is a two-equation model proposed by Menter [75] that uses the transport variable k to determine the turbulence energy and the specific dissipation rate (ω) as the second transport variable to determine the scale of turbulence. This model is a hybrid model that combines the Wilcox (standard) k-ω and k-ε models. This model uses the k-ω formulation in the viscous sub-layer down to the wall and changes to the k-ε behavior in the free-stream since the k-ω formulation is very sensitive for inlet free-stream turbulence properties. The SST k-ω model can be used as a

turbulence model for low Reynolds numbers without the need to use damping functions. It also performs well in the presence of adverse pressure gradients and flows separation. This model produces high levels of turbulence in regions with large normal strain, like stagnation regions and regions with strong acceleration, when compared to the k-ε models [74,76].

The transport equations for the SST k-ω model are as follows:

$$\frac{\partial}{\partial t}(\rho k) + \frac{\partial}{\partial x_i}(\rho k u_i) = \frac{\partial}{\partial x_j}\left(\Gamma_k \frac{\partial k}{\partial x_j}\right) + G_k - Y_k \tag{3.39}$$

$$\frac{\partial}{\partial t}(\rho \omega) + \frac{\partial}{\partial x_j}(\rho \omega u_j) = \frac{\partial}{\partial x_j}\left(\Gamma_\omega \frac{\partial \omega}{\partial x_j}\right) + G_\omega - Y_\omega + D_\omega \tag{3.40}$$

where the term G_k is the production of turbulence kinetic energy, G_ω represents the generation of ω, Γ_k and Γ_ω are the effective diffusivity of k and ω, Y_k and Y_ω represent the dissipation of k and ω due to the turbulence, D_ω is the cross-diffusion term.

The term G_k is defined in the same manner as in the standard k-ε models, see equation 3.25. The term G_ω is defined as follows:

$$G_\omega = \alpha \frac{\omega}{k} G_k \tag{3.41}$$

$$\alpha = \frac{\alpha_\infty}{\alpha^*}\left(\frac{\alpha_0 + {Re_t}/{R_\omega}}{1 + {Re_t}/{R_\omega}}\right) \tag{3.42}$$

$$\alpha^* = \alpha_\infty^*\left(\frac{\alpha_0^* + {Re_t}/{R_k}}{1 + {Re_t}/{R_k}}\right) \tag{3.43}$$

$$Re_t = \frac{\rho k}{\mu \omega} \tag{3.44}$$

$$\alpha_0^* = \frac{\beta_i}{3} \tag{3.45}$$

$$\beta_i = F_1 . \beta_{i,1} + (1 - F_1) . \beta_{i,2} \tag{3.46}$$

The dissipation of k is defined as follows:

$$Y_k = \rho . \beta^* . k . \omega \tag{3.47}$$

$$\beta^* = \beta_i^* \left[1 + \zeta^* F(M_t)\right] \tag{3.48}$$

$$\beta_i^* = \beta_\infty^*\left(\frac{\left({4}/{15}\right) + \left({Re_t}/{R_\beta}\right)^4}{1 + \left({Re_t}/{R_\beta}\right)^4}\right) \tag{3.49}$$

The compressibility function, $F(M_t)$, is given by:

$$F(M_t) = \begin{cases} 0, & M_t \le M_{t0} \\ M_t^2 - M_{t0}^2, & M_t > M_{t0} \end{cases} \quad (3.50)$$

$$M_t^2 = \frac{2k}{a^2} \quad (3.51)$$

where M_t represents the Mach number and a is the sound speed. The dissipation of ω is defined as follows:

$$Y_\omega = \rho.\beta.\omega^2 \quad (3.52)$$

$$\beta = \beta_i \left[1 - \frac{\beta_i^*}{\beta_i}\zeta^*.F(M_t)\right] \quad (3.53)$$

The cross-diffusion term is given by:

$$D_\omega = 2(1-F_1).\rho.\frac{1}{\omega.\sigma_{\omega,2}}.\frac{\partial k}{\partial x_j}\frac{\partial \omega}{\partial x_j} \quad (3.54)$$

The effective diffusivity of k and ω are given by:

$$\Gamma_k = \mu + \frac{\mu_t}{\sigma_k} \quad (3.55)$$

$$\Gamma_\omega = \mu + \frac{\mu_t}{\sigma_\omega} \quad (3.56)$$

$$\sigma_k = \frac{1}{\frac{F_1}{\sigma_{k,1}} + \frac{(1-F_1)}{\sigma_{k,2}}} \quad (3.57)$$

$$\sigma_k = \frac{1}{\frac{F_1}{\sigma_{k,1}} + \frac{(1-F_1)}{\sigma_{k,2}}} \quad (3.58)$$

$$\sigma_\omega = \frac{1}{\frac{F_1}{\sigma_{\omega,1}} + \frac{(1-F_1)}{\sigma_{\omega,2}}} \quad (3.59)$$

$$F_1 = \tanh(\phi_1^2) \quad (3.60)$$

$$\phi_1 = \min\left[max\left(\frac{\sqrt{k}}{0.09\omega y}, \frac{500\mu}{\rho y^2 \omega}\right), \frac{4\rho k}{\sigma_{\omega,2} D_\omega^+ y^2}\right] \quad (3.61)$$

$$D_\omega^+ = \max\left[2\rho\frac{1}{\sigma_{\omega,2}}\frac{1}{\omega}\frac{\partial k}{\partial x_j}\frac{\partial \omega}{\partial x_j}, 10^{-10}\right] \quad (3.62)$$

where y represents the distance to the next surface and D_ω^+ is the positive portion of the cross-diffusion term. Finally, the turbulent viscosity in SST k- ω model is defined as follows:

$$\mu_t = \frac{\rho k}{\omega}\frac{1}{\max\left[\frac{1}{\alpha^*}; \frac{SF_2}{a_1\omega}\right]} \quad (3.63)$$

$$F_2 = \tanh\left(\phi_2^2\right) \tag{3.64}$$

$$\phi_2 = \max\left[\frac{2\sqrt{k}}{0.09\omega y}, \frac{500\mu}{\rho y^2 \omega}\right] \tag{3.65}$$

where S is the strain rate magnitude and the model constants have the following values:

$$\sigma_{k,1} = 1.176 \quad \sigma_{k,2} = 1.0 \quad \sigma_{\omega,1} = 2.0 \quad \sigma_{\omega,2} = 1.168$$
$$\alpha_\infty = 0.52 \quad \alpha_0 = 1/9 \quad \alpha_\infty^* = 1 \quad R_\beta = 8$$
$$\beta_{i,1} = 0.075 \quad \beta_{i,2} = 0.0828 \quad \beta_\infty^* = 0.09 \quad a_1 = 0.31$$
$$R_k = 6 \quad R_\omega = 2.65 \quad \zeta^* = 1.5 \quad M_{t0} = 0.25$$

3.5 Eddy Dissipation Concept

In this work, the combustion model used was the Eddy Dissipation Concept (EDC) which was developed by Magnussen [77]. This model has the advantage of incorporating the influence of the finite kinetic rate in a very moderate computational cost when compared to more advanced models such as the transported PDF method. This advantage is associated with the cost of a less accurate description of turbulent temperature fluctuations [63].

In the EDC model, the influence of turbulent fluctuations on the mean rate of chemical reaction is associated with the phenomenological description of turbulence in terms of the turbulent energy cascade. The key variables used in the description of the turbulent energy cascade are the energy dissipation rate (ε) and the characteristics of the viscous scale of the flow (Kolmogorov scale), *i.e.*, the description of this energy cascade depends only on ε and kinematic viscosity (ν) [63].

This model assumes that chemical reactions occur in confined zones called fine structures that can be smaller than the size of the computational mesh used. These structures are characterized by being adiabatic and isobaric structures and perfect stirred reactors, transferring only mass and energy to the surrounding fluid that is responsible for supplying the reactants and removing the products from the chemical reactions of the fine structures. The scale of the length of the fine structure, ξ, and the mean residence time of the fluid inside the fine structure, in other words, the time scale of the fine structure, τ, are determined as follows:

$$\xi = C_\xi \left(\frac{\nu\varepsilon}{k^2}\right)^{1/4} \tag{3.66}$$

$$\tau = C_\tau \left(\frac{\nu}{\varepsilon}\right)^{1/2} \tag{3.67}$$

where C_ξ and C_τ are constant and have values of 2.1377 and 0.4082, respectively.

The EDC model assumes that all chemical reactions occur only in fine structures, so the reaction rate of the chemical species is determined through the mass balance in the structure and that the net mean species reaction rate present in equation 3.22 is given by:

$$\overline{\dot{\omega}_\iota} = \frac{\bar{\rho}\tilde{\xi}^2}{\tau}\frac{(Y_i^* - \tilde{Y}_i)}{(1-\tilde{\xi}^3)} \tag{3.68}$$

where $\tilde{Y}_i$ is the average mass fraction of ith species and is calculated by combining the mass fractions of ith species inside, Y_i^*, and outside, Y_i^o, the fine structure, see equation 3.69.

$$\tilde{Y}_i = \tilde{\xi}^3 Y_i^* + (1-\tilde{\xi}^3)Y_i^o \tag{3.69}$$

In *Ansys Fluent* code, the EDC model assumes that the fine structure are small perfectly stirred, constant pressure and temperature reactors where the mass fraction of the chemical species is obtained by integration from t = 0 to t = τ of the formation/destruction rate of each species ($\dot{\omega}_i$) through the following equation:

$$\frac{d}{dt}\left(\rho Y_i(t)\right) = \dot{\omega}_i(t) \tag{3.70}$$

$$\dot{\omega}_i = M_i \sum_r^{N_r} R_{i,r} \tag{3.71}$$

The formation/destruction rate of chemical species is obtained by adding the Arrhenius terms of the reactions present in combustion such that $R_{i,r}$ represents the formation rate of ith species in reaction r, see equation 3.71. In the calculation algorithm, equation 3.71 is first solved in the whole control volume for each iteration in which the mean values of temperature and mass fraction in each computational cell are used as initial conditions. The term Y_i^* is obtained through the integration of equation 3.70, the source term in equation 3.22 is obtained through equation 3.68 and finally the term y_i is obtained by equation 3.22.

The temperature is iteratively calculated through enthalpy as follows:

$$\tilde{h} = \sum_i^n \tilde{Y}_i h_i(\tilde{T}) \tag{3.72}$$

while $\bar{\rho}$ is determined according to the perfect gases law as follows:

$$\frac{1}{\bar{\rho}} = \frac{R\tilde{T}}{\rho}\sum_i^n \frac{\tilde{Y}_i}{M_i} \tag{3.73}$$

The EDC model is an extension of the eddy dissipation model that allows a detailed chemical mechanism to be included in turbulent flows. In order to reduce the computational time associated with the integration of Arrhenius reaction rates in these fine structures, the In Situ Adaptative Tabulation (ISAT) method proposed by Pope [78] is used.

3.6 Discrete Ordinates Method

The discrete ordinates (DO) method is used in this work as a radiation model to define the source term present in the energy conservation equation, see equation 3.21.

According to Coelho [79], the discrete ordinate term refers to an angular discretization procedure in which the radiative transfer equation (RTE) is solved for a finite set of directions. Weighting factors or weights are used for all directions such that the sum of these weights is equal to the area of a spherical surface with a radius of 1, *i.e.*, 4π and the integrals over the solid angles are evaluated using the quadrature method. The radiative transfer equation to an absorbing/emitting, non-scattering and gray medium is given as follows [80]:

$$\frac{dI(\vec{s})}{ds} = \kappa(-I(\vec{s}) + I_b) \tag{3.74}$$

where $I(\vec{s})$ is the radiative intensity in the direction $\vec{s}$, κ is the absorption coefficient of the medium and I_b is the blackbody radiative intensity. The boundary conditions for a diffuse surface are given by:

$$I_w(\vec{s}) = \varepsilon_w I_{bw} + \frac{\rho_w}{\pi} \int_{\vec{n}.\vec{s'}<0} I\left(\vec{s'}\right) \left|\vec{n}.\vec{s'}\right| d\Omega' \tag{3.75}$$

where ε_w and ρ_w represent the emissivity and reflectivity of the surface, respectively, $I_w(\vec{s})$ is the radiative intensity of the surface in the direction $\vec{s}$ and I_{bw} represents the blackbody intensity on the surface. The vector $\vec{n}$ represents the normal vector to the surface and $\vec{n}.\vec{s'} = \cos\theta'$ is the cosine of the angle between any incoming $\vec{s'}$ and the normal vector, as shown in figure 3.1.

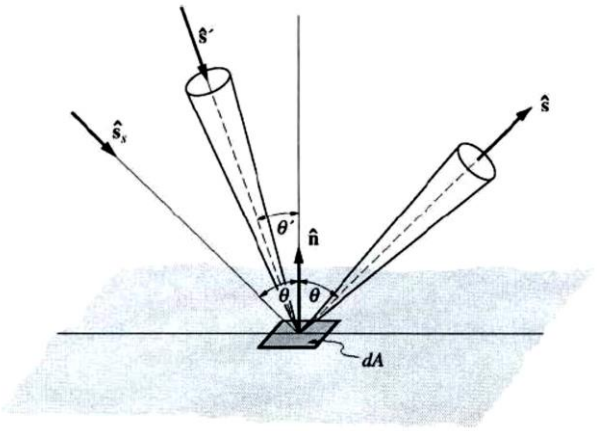

Figure 3.1 – Radiative intensity reflected from a surface.

According to Modest [80], the radiative transfer equation is solved for a set of n different directions in a solid angle of 4π as follows:

$$\frac{dI^n}{ds} = \kappa(-I^n + I_b) \tag{3.76}$$

and the boundary condition for a given direction is given by:

$$I_w^n = \varepsilon_w I_{bw} + \frac{\rho_w}{\pi} \sum_j w_j I^j \left|\vec{n}.\vec{s_j}\right| \tag{3.77}$$

where w_j is the weight of the quadrature in the j direction. The finite volume approach is used for spatial discretization, integrating the equation for each control volume and applying the divergence theorem. In this work, the simulations are carried out in a 2D space, so equation 3.76 is written as follows:

$$|\xi^n|(A_E I_e - A_W I_w) + |\eta^n|(A_N I_n - A_S I_s) = \kappa\left(I_{b,P} - I_P\right)V \tag{3.78}$$

where A_E, A_W, A_N and A_S are the areas of the faces of the volume element and I_e, I_w, I_n and I_s represent the average radiative intensities associated with the center of each face, see figure 3.2. The terms $I_{b,P}$ and I_P represent the average intensities associated with the center of the volume element, point P, and ξ^n and η^n are the direction cosine of direction n.

The source term present in the energy conservation equation is given by:

$$\dot{q_R}''' = \nabla.\vec{q} = \kappa(4\pi I_b - G_{inc}) \tag{3.79}$$

where $\vec{q}$ is the radiative heat flux vector and G_{inc} is the incident radiation obtained as follows:

$$G_{inc} = \int_{4\pi} I(\vec{s})\, d\Omega \simeq \sum_{j=1}^{N} w_j I^j \tag{3.80}$$

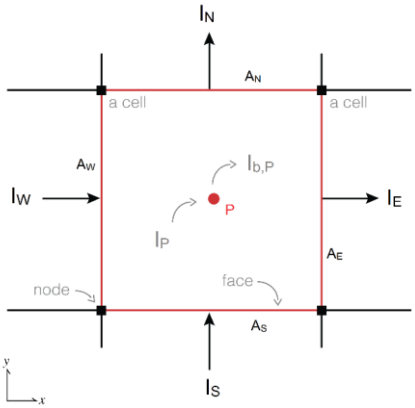

Figure 3.2 – Representation of a 2D volume element

The properties of the gases present in the medium required by the radiation model are calculated using the weighted sum of gray gases model (WSGG). When the gray gases hypothesis is valid, the total absorptivity and total emissivity are similar and calculated as follows:

$$\varepsilon(T,s) = \alpha(T,s) = \frac{1}{I_b(T)}\int_0^\infty (1 - e^{-\kappa_\eta s}) I_{b\eta}(T) d\eta \tag{3.81}$$

With the application of the WSGG model, the total emissivity can be approximated by:

$$\varepsilon(T,s) = \sum_{i=1}^{I} a_{\varepsilon,i}(T)(1 - e^{-\kappa_i p_i s}) \tag{3.82}$$

where $a_{\varepsilon,i}$ is the weighting factor for the ith fictious gray gas, κ_i and p_i are the absorption coefficient and partial pressure of the ith gray gas, respectively, and s is the path length. For the medium emissivity calculation only the CO_2 and H_2O were considered as absorbing gases. In the *Ansys* software, the values of the absorption coefficient and the weighting factor of the above-mentioned species are taken from the work done by Smith *et al.* [81] and Coppalle and Vervisch [82].

3.7 Soot Modelling

In this work, the soot formation model used in turbulent non-premixed combustion is the Moss-Brookes model [83]. This model solves two transport equations, one is responsible to determinate the soot mass fraction (Y_{soot}) and the second equation determines the normalized radical nuclei concentration (b^*_{nuc}). The two equations are described as follows [74]:

$$\frac{\partial}{\partial t}(\rho Y_{soot}) + \nabla.(\rho \vec{v} Y_{soot}) = \nabla.\left(\frac{\mu_t}{\sigma_{soot}} \nabla Y_{soot}\right) + \frac{\partial M}{\partial t} \tag{3.83}$$

$$\frac{\partial}{\partial t}(\rho b^*_{nuc}) + \nabla.(\rho \vec{v} b^*_{nuc}) = \nabla.\left(\frac{\mu_t}{\sigma_{soot}} \nabla b^*_{nuc}\right) + \frac{1}{N_{norm}} \frac{\partial N}{\partial t} \tag{3.84}$$

where N_{norm} is a model constant, M is the soot mass concentration and N is the soot particle number density. The instantaneous production rate of soot particles, $\frac{\partial N}{\partial t}$, and the source term for soot mass concentration, $\frac{\partial M}{\partial t}$, are modeled by the following expressions [74]:

$$\frac{dN}{dt} = C_\alpha N_A \left(\frac{X_{prec}P}{RT}\right)^l \exp\left\{-\frac{T_\alpha}{T}\right\} - C_\beta \left(\frac{24RT}{\rho_{soot}N_A}\right)^{1/2} d_p^{1/2} N^2 \tag{3.85}$$

$$\frac{dM}{dt} = M_P C_\alpha \left(\frac{X_{prec}P}{RT}\right)^l \exp\left\{-\frac{T_\alpha}{T}\right\} + C_\gamma \left(\frac{X_{sgs}P}{RT}\right)^m \exp\left\{-\frac{T_\gamma}{T}\right\} \left[(\pi N)^{1/3} \left(\frac{6M}{\rho_{soot}}\right)^{2/3}\right]^n - C_{oxid} C_\omega \eta_{coll} \left(\frac{X_{OH}P}{RT}\right) \sqrt{T}\, (\pi N)^{1/3} \left(\frac{6M}{\rho_{soot}}\right)^{2/3} \tag{3.86}$$

where C_α, C_β, C_γ, C_{oxid}, C_ω, η_{coll}, l, m and n are model constants and N_A, ρ_{soot} and M_P represent the Avogadro Number, mass density of soot and the mass of an incipient soot particle, respectively. The parameters T_α, T_γ represent the activation temperature of soot inception and surface growth rate, X_{prec}, X_{sgs}, X_{OH} are the mole fractions of soot precursor, participating surface growth species and OH radical, respectively, d_p is the mean diameter of a soot particle and η_{coll} represents the collision efficiency.

The Moss-Brookes model assumes that the OH radical is the oxidizing agent and the surface-specific oxidation rate of soot by this radical is determined according to the model proposed by Fenimore and Jones. In this work, the soot-turbulence and soot-radiation interactions were also taken into account. The Moss-Brookes model constants have the following values [74]:

$N_{norm} = 10^{15}\ particles$	$M_P = 144\ kg/kmol$	$C_\alpha = 54\ s^{-1}$	$C_\beta = 1.0$
$N_A = 6.022 \times 10^{26}\ kmol^{-1}$	$T_\alpha = 21 \times 10^3\ K$	$C_\gamma = 11.7 \times 10^3\ \frac{kg.m}{kmol.s}$	$C_{oxid} = 0.015$
$\rho_{soot} = 1800\ kg/m^3$	$T_\gamma = 12.1 \times 10^3\ K$	$C_\omega = 105.8125\ \frac{kg.m}{kmol.K^{1/2}.s}$	$\eta_{coll} = 0.04$

4. Experimental and Numerical Setup

4.1 Experimental Setup

The purpose of this section is to provide an insight into how the experimental campaign is carried out. It is important to note that the experimental tests for methane flameless combustion were performed by Rebola *et al.* [16]. The present work is performed using only computational tools.

This section presents the characteristics of the small-scale combustor and the techniques used to obtain temperature and species concentration profiles inside the combustor.

4.1.1 Small-scale Combustor

Figure 4.1 shows schematically the combustor used in this study [16]. The combustion chamber is a stainless-steel cylinder with an inner diameter of 150 mm and a length of 300 mm. The burner is placed on the top of the combustion chamber and the flue gases are exhausted at the opposite end through a convergent nozzle with a length of 50 mm and an angle of 35º. The combustion chamber contains five ports along its length, each with a diameter of 20 mm to allow the introduction of a probe inside the combustion chamber. The five ports are located at 30, 90, 150, 210 and 270 mm from the burner.

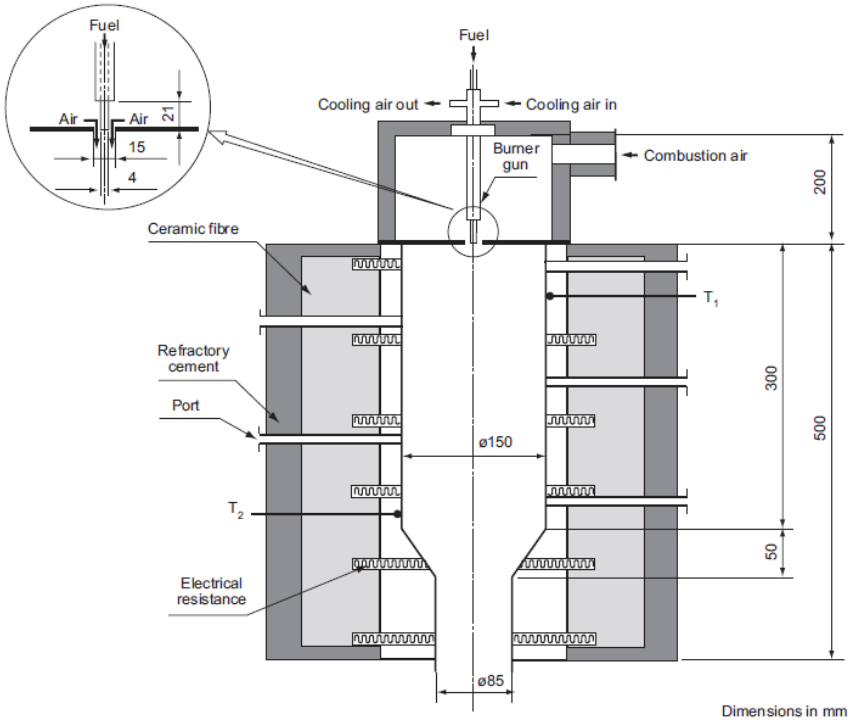

Figure 4.1 – Schematic representation of the small-scale combustor [16].

The combustion chamber walls are equipped with an electric heating system to allow the walls to be preheated to a temperature of 900 ºC. Two K-type thermocouples are installed in the combustion chamber, as shown in figure 4.1, in order to monitor the wall temperature and evaluate the temperature gradient along its axis. The burner consists of a central gas gun with an internal diameter of 4 mm and an external diameter of 6 mm and the combustion air is supplied in a conventional double concentric

configuration, see figure 4.1., the combustion air is preheated through an electric heating system to a temperature of 700 ºC.

4.1.2 Measurement Setup

Local mean temperature measurements were made using a R-type thermocouple. The R-type thermocouple consists of a fine wire of 100% platinum welded to a fine wire of platinum alloy with 13% rhodium, both wires have a diameter of 76 μm. This welded wire is supported to wires with diameter of 350 μm of the same material located in a twin-bore alumina sheath with an external diameter of 5 mm. The uncertainty due to heat transfer by radiation was estimated to be less than 5% considering the heat transfer by radiation and convection between the thermocouple and the surroundings [16].

The species measured were O_2, CO, CO_2, unburned hydrocarbons (HC) and NO_x. The gas sample containing these species is removed through a water-cooled stainless-steel probe. The gases are filtered and dried before entering the analyzer system [16]. This system consists of a magnetic pressure analyzer for O_2 measurements, a flame ionization detector for HC measurements and a chemiluminescent analyzer for NO_x measurements [16]. The main sources of uncertainty in the concentration measurements found inside the combustion chamber were the quenching of chemical reactions and aerodynamic disturbances of the flow. The uncertainty of the gases measured inside the combustion chamber was 10% of the average value [16].

The procedure used to measure the species concentration of flue gases at the combustion chamber outlet is identical to the procedure used to measure species concentrations inside the combustion chamber. Aerodynamic flow disturbances due to the probe are negligible, so the only source of uncertainty is the quenching of the chemical reactions [16]. The measured uncertainty is 5% of the average value [16].

4.2 Numerical Setup

This section presents all the essential elements used to perform this computational work. This section presents the computational domain, the numerical methods used and the established convergence criteria.

4.2.1 Computational Domain

The geometrical details of the burner and the combustion chamber are outlined in figure 4.1. As the combustor is symmetrical and the nature of the flow inside the combustor presents symmetry, the simulations can be performed in a two-dimensional and axisymmetric plane, see figure 4.2.

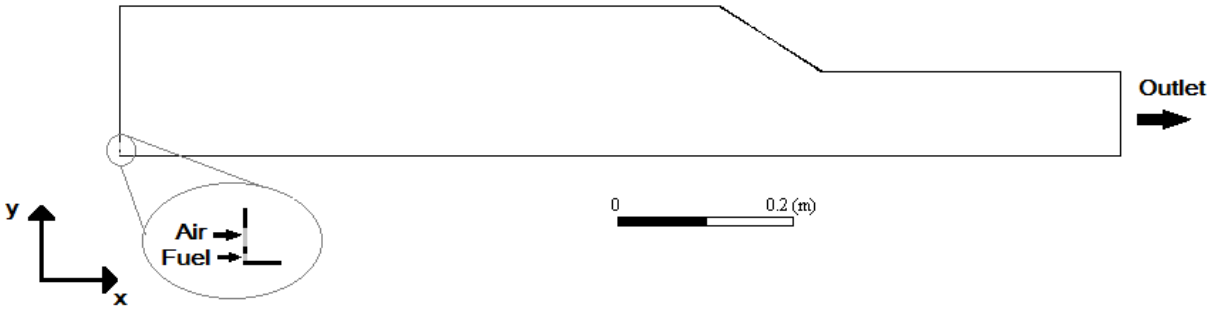

Figure 4.2 – Computational domain of the combustor.

Ansys Workbench was used to design the mesh for the computational domain. The grid used is an unstructured mesh composed by quadrilateral elements, see appendix A.1. To determine the number of cells in the mesh that produce satisfactory results for the present study, three meshes were studied. The coarse mesh composed by 50 000 elements, the intermediate mesh contains 79 000 elements and finally the fine mesh contains about 114 000 elements. The study of the influence of the grid size is discussed in the next chapter.

Table 4.1 – Solution and discretization methods.

Variable	Numerical Method
Gradient	SIMPLE
Pressure	Green – Gauss Node Based
Momentum	Second Order Upwind
Turbulent kinetic energy, k	Second Order Upwind
Specific dissipation rate, ω	Second Order Upwind
Dissipation rate of turbulence kinetic energy, ε	Second Order Upwind
Energy	Second Order Upwind
Species	Second Order Upwind
Discrete ordinates	Second Order Upwind

The solution options and spatial discretization schemes chosen for each solved equation are listed in table 4.1. The convergence of the solution for all the simulations performed was based on the sum of the residues for each equation and on the monitoring of a predefined set of points. The values used in the first part of the convergence criterion are listed in table 4.2.

The second convergence criterion is based on the monitoring of the following variables: axial velocity, temperature and CO_2 and CO molar fractions for fuels containing carbon elements in their composition and molar fractions of H_2, NH_3 and H_2O for carbon-free fuels. The monitoring points used have the following coordinates: (x,y) = (30,0), (x,y) = (300,0) and (x,y) = (500,0). The second point is located immediately before the contraction of the combustion chamber and the third point corresponds to the point of flue gas exit in the combustion chamber.

Table 4.2 – Convergence criterion of the sum of residuals

Equation	Residuals
Continuity	10^{-4}
X – velocity	10^{-6}
Y – velocity	10^{-6}
Energy	10^{-6}
Turbulent kinetic energy, k	10^{-6}
Specific dissipation rate, ω	10^{-6}
Dissipation rate of turbulence kinetic energy, ε	10^{-6}
Energy	10^{-6}
Species	10^{-4}
Discrete ordinates	$5x10^{-6}$

For numerical simulations, it is important to highlight the boundary conditions used in the reference case [59]. These conditions combined with the experimental data in methane flameless combustion allow the study of the most adequate turbulence model to characterize the flow present in the combustor and to study the grid independence. Table 4.3 presents the boundary conditions used in this work [59].

Table 4.3 – Boundary conditions for reference case [59]

Parameter		Value
Fuel		Methane (CH_4)
Input Power (kW)		10
Equivalence ratio (φ)		0.5
Inlet air temperature (K)		773
Inlet air velocity (m/s)		102.1
Inlet fuel temperature (K)		293
Inlet fuel velocity (m/s)		24.4
Wall temperature (K)		1173
Wall emissivity (ε)		0.7
Outlet pressure (atm)		1
Air and fuel turbulent intensity (%)		10
Hydraulic diameter (mm)	Air	9
	Fuel	4
Kinetic Mechanism	Name	GRI-Mech 2.11 [84]
	Nº of species	49
	Nº of reactions	277

To perform the combustion simulations for the fuels proposed in this work, it is important to know that the only variables changed are: the air inlet velocity, the equivalence ratio, the fuel inlet temperature and velocity and the kinetic mechanism. The other boundary conditions presented in table 4.3 remain

unchanged. Table 4.4 presents the tested conditions for the proposed fuels, as well as the associated kinetic mechanism, specifying the number of species and reactions present in the mechanism.

Table 4.4 – The tested conditions and the kinetic mechanism used for the fuels proposed.

Fuel	*φ*	*Inlet air velocity (m/s)*	*Inlet fuel velocity (m/s)*	*Inlet fuel temperature (K)*	*Kinetic Mechanism*		
					Name	*Nº of species*	*Nº of reactions*
Propane	0.5	99.15	9.36	293	Polimi_C1C3 [85]	115	2142
Acetylene	0.5	80.70	15.24	293	FFCM-1 [86]	38	291
Biogas	0.5	101.00	39.74	293	GRI-Mech3.0 [64]	53	325
Ethanol	0.5	95.11	21.60	423	Marinov [69]	57	383
Syngas	0.5	79.93	89.85	293	Polimi_H2CO [85]	32	174
Hydrogen	0.5	84.09	81.28	293	Polimi_H2CO [85]	32	174
50%CH_4/50%H_2	0.5	97.01	36.64	293	GRI-Mech3.0 [64]	53	325
30%CH_4/70%NH_3	0.5	98.57	41.37	293	Li 2019 [55]	51	420
20%CH_4/80%NH_3	0.5	97.89	46.22	293	Li 2019 [55]	51	420
	2/3	73.42	46.22				
	1	48.95	46.22				
	1.2	40.79	46.22				
30%H_2/70%NH_3	0.5	92.93	65.00	293	Li 2019 [55]	51	420
20%H_2/80%NH_3	0.5	93.98	63.39	293	Li 2019 [55]	51	420
	2/3	70.48	63.39				
	1	46.99	63.39				
	1.2	39.16	63.69				

To close this chapter, it is important to note that the kinetic mechanisms used in acetylene and ethanol do not have the NO_x formation mechanisms. The thermal-NO, prompt-NO and intermediate N_2O-route mechanisms available in *Ansys Fluent* [74] were applied in the post-processing of the main combustion calculations. Furthermore, it is important to mention that acetylene and propane are fuels with tendency for soot formation under conventional non-premixed combustion, which means that there is a need to simulate soot formation in the flameless combustion mode. The soot formation model applied is the Moss-Brookes model which is also available on *Ansys Fluent* [74]. The soot formation model is run simultaneously with the turbulence, combustion and radiation models in contrast to the NO_x formation mechanisms for NO_x prediction in acetylene and ethanol.

5. Results and Discussion

In this chapter, all the results obtained in the simulations performed on *Ansys Fluent 18* will be presented and discussed. This chapter is divided into four sections. In the first section, the study of the influence of the grid size will be presented. Then, the influence of the turbulence models and the comparison of the predicted results with the experimental results will be studied. In the third section, the simulation results for different fuels will be presented and discussed in order to find the influence of the fuel in obtaining flameless combustion, keeping the same geometrical characteristics of the combustor and operational conditions. Finally, the last section shows the flue gas emissions at the combustion chamber outlet and the flue gas recirculation rate for each fuel.

Before presenting the results, it is important to know that each simulation is divided into three parts. In the first part, the simulation runs in the conventional non-premixed combustion regime through the chemical equilibrium model to obtain ignition and ends when the convergence criterion for continuity, velocities and energy is reached. Then, the combustion model is changed from the chemical equilibrium model to the species transport model, where the Eddy-Dissipation Concept model is used together with the most appropriate kinetic mechanism for the fuel to be studied. In this second part, the ISAT tolerance is 10^{-3} and the simulation runs until the convergence criteria are satisfied. The last part corresponds to a decrease in the ISAT tolerance to 10^{-4} and the simulation is performed until the convergence criteria are satisfied and the final solution is reached and analyzed.

5.1. Grid Independence Study

In this section, the effect of the grid size is studied, in other words, the minimum number of grid elements for which there is convergence in the results obtained. The three meshes studied are composed approximately by 50 000, 79 000 and 114 000 elements, respectively. The study of the grid independency is carried out under methane flameless combustion, whose operating conditions are shown in table 4.3 in the previous chapter.

The grid independency study is done by comparing the axial profiles of temperature, velocity and O_2, CO_2, CO and NO_x concentrations. The profiles are shown in figure 5.1.

In figure 5.1, it can be seen that the three meshes behave in similar way in the velocity field and in the O_2 and CO_2 concentration fields. From the temperature data, it can be seen that between the points x = 300 mm and x = 400 mm there is a slight change in the behavior of the profiles. When the number of elements in the mesh increases, the maximum temperature decreases. The maximum temperature difference occurs between the coarse mesh and the fine mesh for the position $x \approx 378$ mm and has a value of 31.5 K. The relative error associated with this temperature difference is less than 2.35%, which is less than the thermocouple error used by Rebola *et al.* [59], which is 5%.

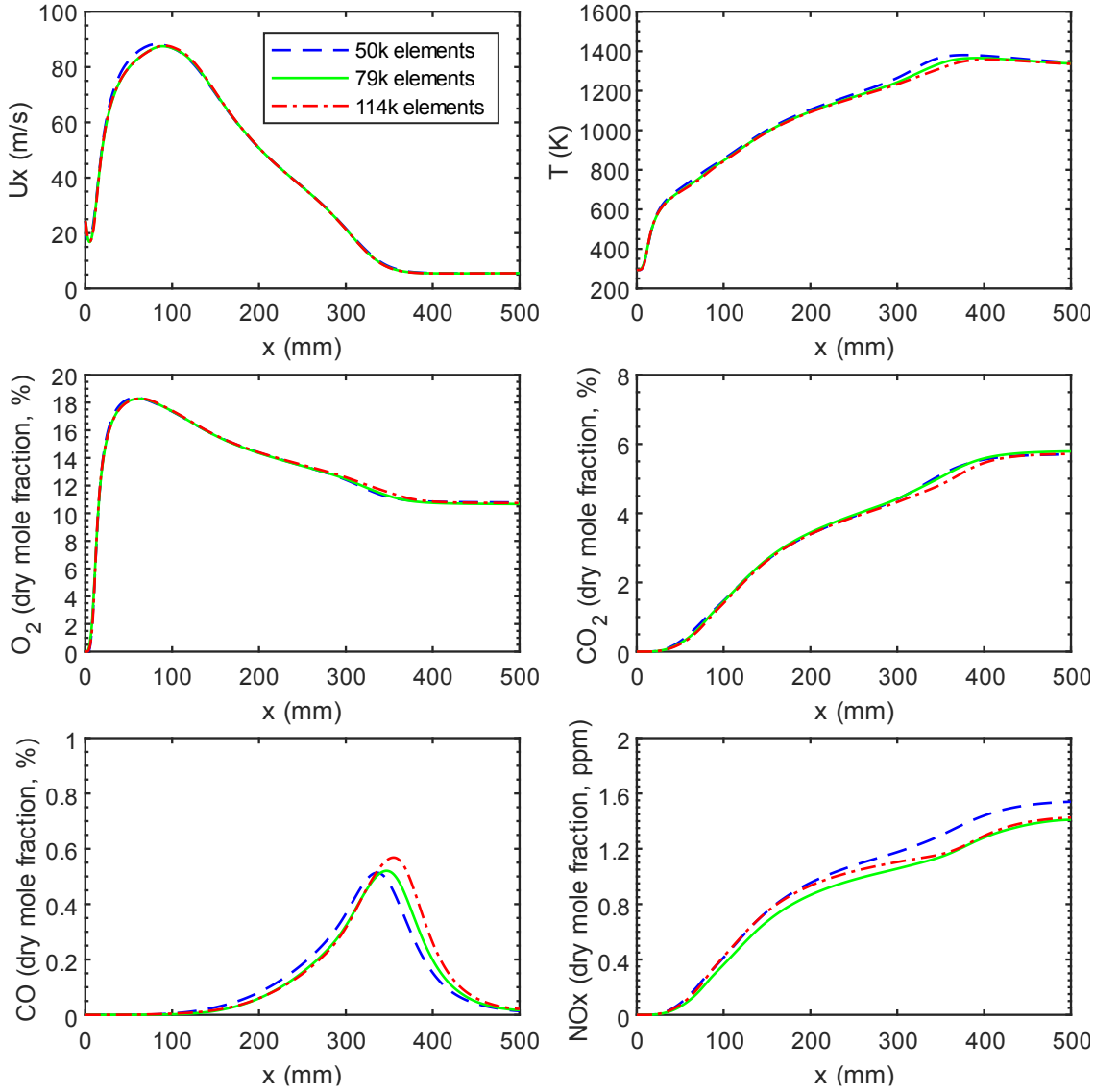

Figure 5.1 – Predicted of axial profiles of axial velocity, temperature, O_2, CO_2, CO and NO_x molar fractions on a dry basis

From figure 5.1, it is observed that the CO concentration profiles have the same behavior, but the maximum CO concentration has different values and occurs at different positions. For the coarse mesh, the maximum CO molar fraction is 0.513%, the maximum CO molar fraction is 0.52% for intermediate mesh and the fine mesh has a maximum CO molar fraction of 0.568%. According to the CO concentration data, it can be observed that the reaction zone moves downstream of the burner when the number of elements in the mesh increases, which promotes small deviations in the CO_2 concentration and temperature profiles in the region located between x = 300 mm and x = 400 mm.

The NO_x concentration, presented in figure 5.1, shows that the coarse mesh tends to overestimate the NO_x concentration compared to the NO_x concentration of the other meshes. At the combustion chamber outlet, the coarse mesh predicts a NO_x molar fraction of 1.54 ppm, while the intermediate mesh yields 1.41 ppm of NO_x and the NO_x molar fraction for the fine mesh is 1.43 ppm. The maximum difference is 0.13 ppm which corresponds to a relative error of 9.2%. This error is less than the uncertainty present

in the species concentration measurement techniques performed by Rebola *et al.* [59], which is 10%. It is important to note that the relative errors calculated in the CO or NO_x concentration fields tend to be higher than the errors calculated in the temperature field. In this case, CO and NO_x concentrations are mostly 10^3 and 10^6 times lower than the reported temperature values. Therefore, small perturbations tend to produce larger relative errors in the CO and NO_x concentration fields than in the temperature field.

Based on the available data in figure 5.1 and the statements mentioned above, it can be concluded that the mesh with 79 000 elements is adequate to perform the study of influence of the turbulence models and the numerical simulations for the other fuels. The reason for excluding the coarse mesh is that it overestimates the temperature and the NO_x concentration and underestimates the CO concentration compared to the other meshes. The fine mesh was excluded due to the higher computational cost and computational time to obtain results similar to those of the intermediate mesh.

5.2 Independence of Turbulence Models

The turbulence models studied in this work are standard k-ε (SKE), realizable k-ε (RKE) and SST k-ω (SSTKW), which are described in chapter 4. The purpose of this section is to study which turbulence model together with the EDC and discrete ordinates models simulate results consistent with experimental data for methane flameless combustion obtained by Rebola *et al.* [16,59].

The experimental parameters measured were the temperature and the O_2, CO_2, CO and NO_x concentrations. Figure 5.2 shows the radial profiles of temperature and O_2 and CO_2 molar fractions and figure 5.3 presents the radial profiles for CO and NO_x molar fractions. It is important to remember that the burner is located at the top of the combustion chamber while the flue gases are exhausted at the bottom of the combustion chamber.

Based on the figures 5.2 and 5.3, it is observed that three studied turbulence models present similar behavior for all parameters and axial positions studied, with some exceptions. For the position x = 270 mm, it can be seen that the SST k-ω model produces satisfactory results compared to experimental results for all parameters studied except for CO concentration. This happens because the SST k-ω model is a combination of standard k-ε and Wilcox k-ω models, which allows the SST k-ω model to predict satisfactory results near and far from the wall positions.

In figure 5.2, it is analyzed that the studied models tend to underestimate the values near the symmetry axis when compared with the experimental results for the temperature field until the position x = 150 mm, but there is an adequate prediction of the values near the wall when compared with experimental results. The same behavior can be observed in the CO_2 concentration field. Relatively to the O_2 concentration field, there is a reasonable agreement between the predicted and experimental results.

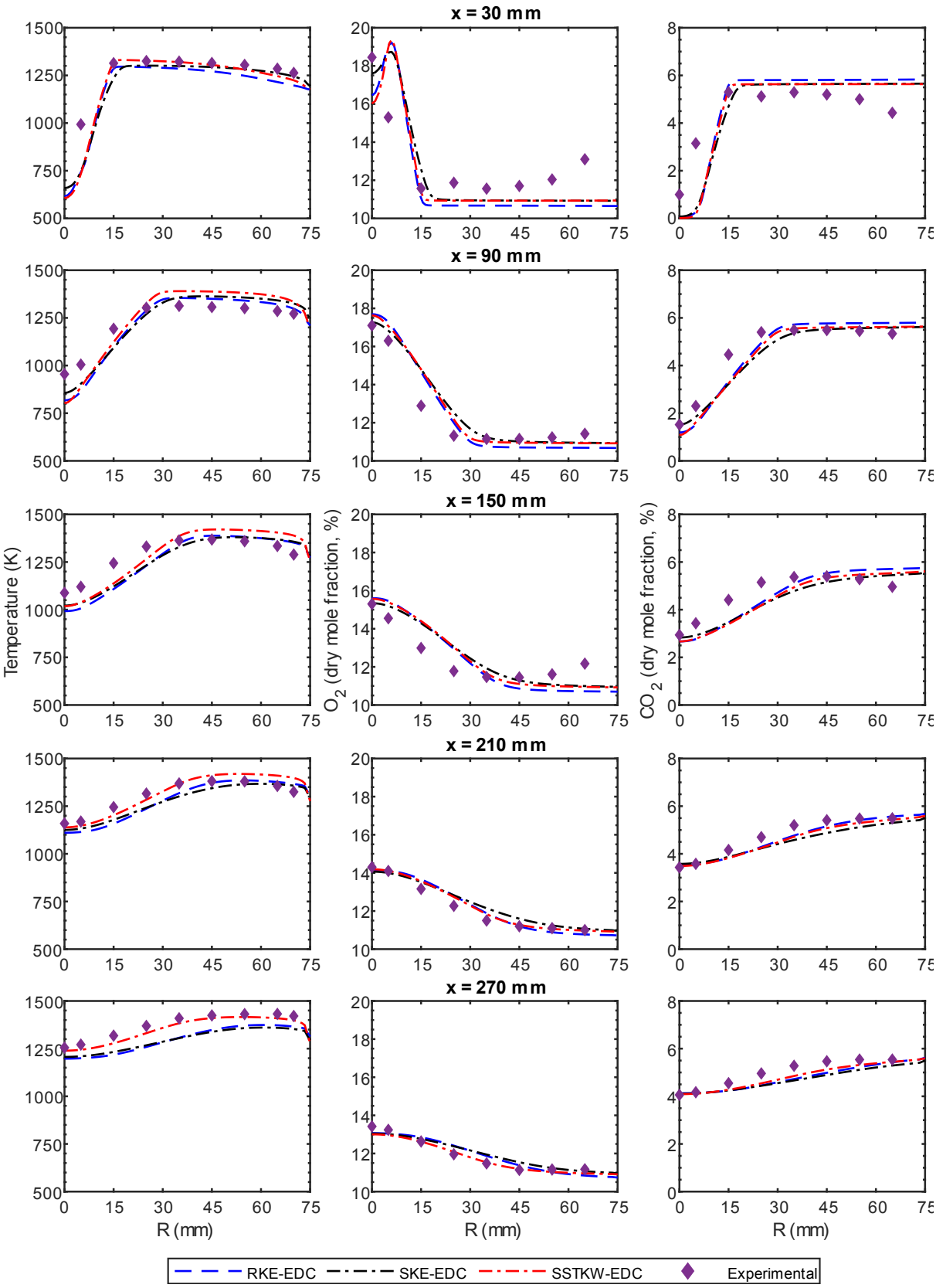

Figure 5.2 – Predicted and measured radial profiles of temperature, O_2 and CO_2 mole fractions on a dry basis.

The three models overestimate the CO concentration when compared to the experimental results, but the realizable k-ε model is the one that predicts the lower CO concentration, see figure 5.3.

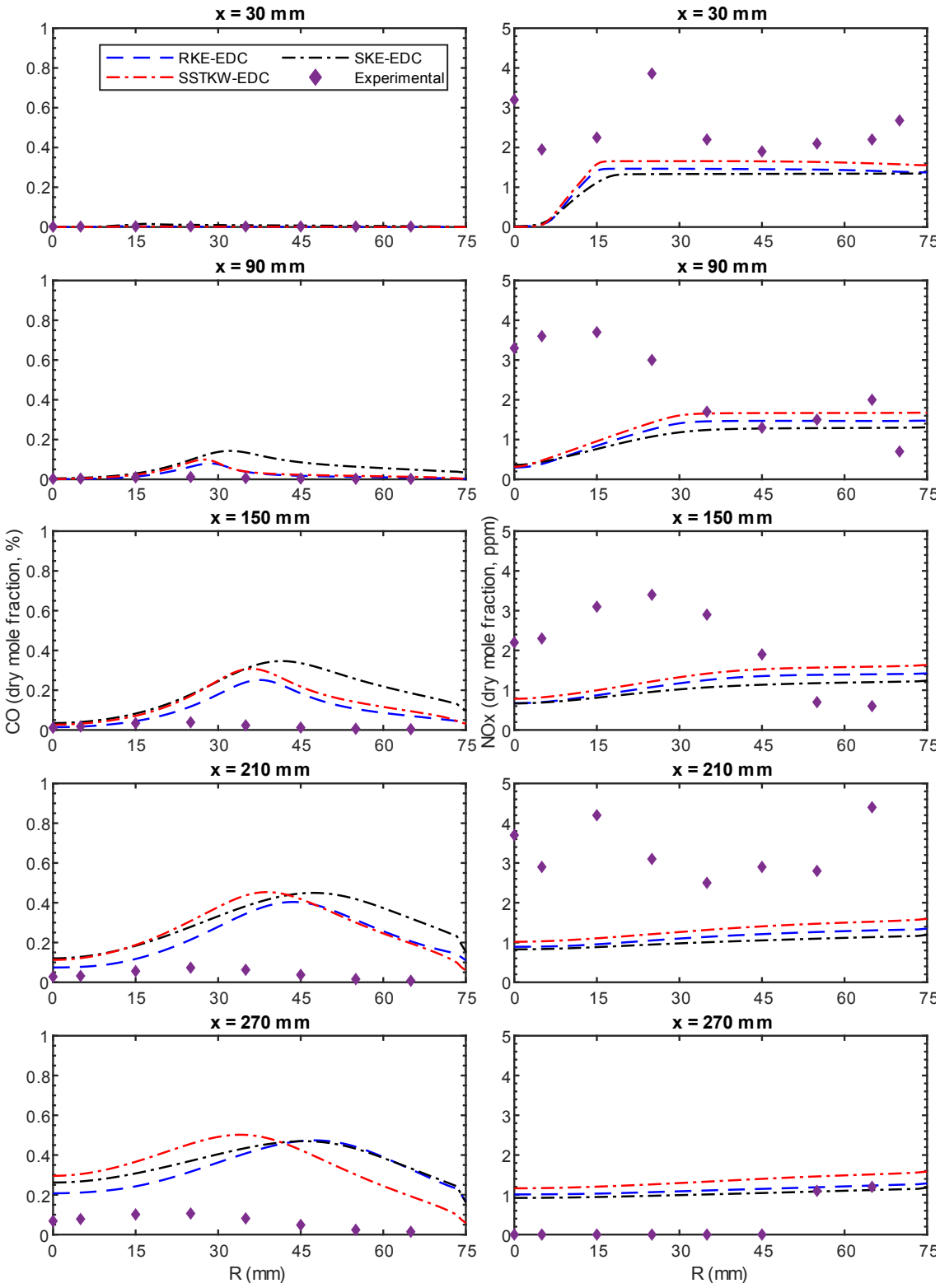

Figure 5.3 – Predicted and measured radial profiles of CO and NO_x mole fractions on a dry basis.

From figure 5.3, it can be seen that in the first four radial positions regardless of the axial position the models tend to underestimate the NO_x concentration. For the positions close to the wall, the predicted

results have a reasonable agreement with the experimental results, except for x = 210 mm. The three turbulence models reproduce similar NO_x concentration profiles and none of them can reproduce the NO_x concentration profile obtained experimentally due to significant experimental uncertainty when the chemical species concentration is too low. The thermal-NO, prompt-NO and intermediate-N_2O route mechanisms for NO_x formation are included in the kinetic mechanism and the NO_x concentration is calculated during the simulation and not in post-processing.

The results presented in figures 5.2 and 5.3 show that all the turbulence models perform satisfactorily. Although, in general, the standard k-ε model is the least accurate model, the flow in the combustion chamber does not present a strong adverse pressure gradient or a strong curvature of the streamlines or the presence of rotation in the flow, as verified by Rebola *et al.* [59]. The lack of experimental measurements of the mean and fluctuating velocity fields prevents a rigorous analysis for the selection of the appropriate turbulence model for this small combustor, requiring the use of one more criterion to help in the choice of the turbulence model.

The auxiliary criterion used to choose the appropriate turbulence model is the computational time. Based on this criterion and for this combustion chamber, it is observed that SST k-ω model is the model that takes the longest time to reach the convergence criteria presented in chapter 4. Both tested k-ε models take approximately the same time to reach the defined convergence criteria, but for the standard k-ε model, it is necessary to change the species relaxation factors to reach the value of 10^{-4} defined for the species residues in the convergence criteria.

Therefore, based on the results presented in figures 5.2 and 5.3 and on the computational time criterion, the realizable k-ε model is chosen to study the influence of the fuel to obtain flameless combustion keeping the same geometric characteristics of the combustor and operational conditions.

5.3 Influence of Fuel on Flameless Combustion

In this part, the combustion simulations performed on fuels tested in this work are presented. The main objective is to determine how the performance of different fuels affects the achievement of the flameless combustion mode for a burner designed to operate in this combustion mode. The different fuels as well as the operating conditions are available in table 4.4 in chapter 4. The combustion of these fuels has not been studied experimentally or numerically by other authors for this small combustor.

Based on previous experimental and numerical studies carried out on this small scale combustor [16,59] and based on the fundamental knowledge acquired in the literature, the nature of the flow must be explained to better understand the results presented. The air jet momentum is strong enough to generate a reverse flow zone that is responsible for the recirculation of the hot flue gas towards the reactant inlet zone. This momentum is also responsible for the dilution of the fuel from the central jet and the oxygen in the entire combustion chamber to allow flameless combustion. Figure 5.4 shows the vector field and the streamlines of the axial velocity and the temperature contour for flameless combustion of methane.

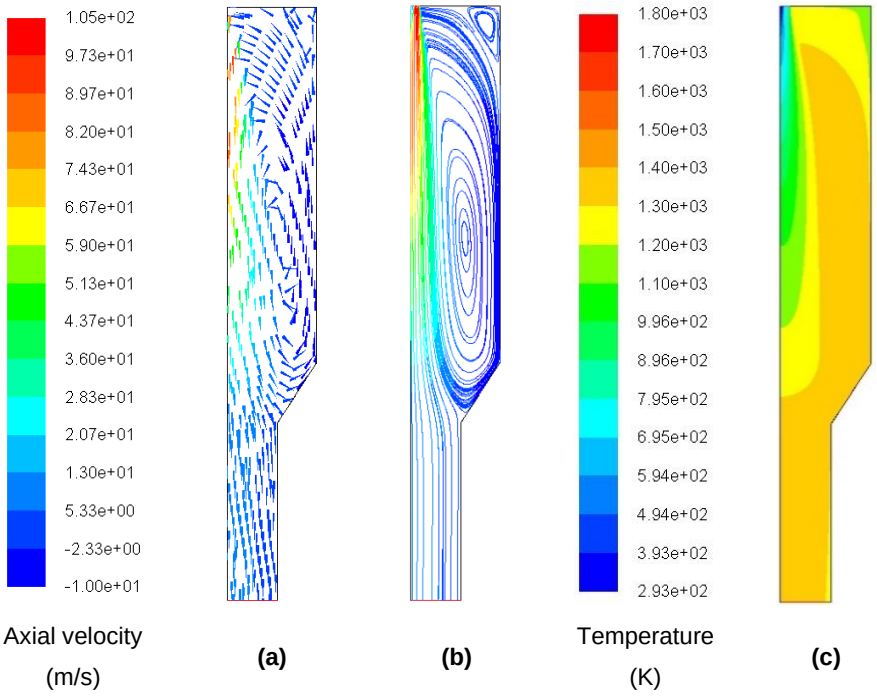

Figure 5.4 – Vector field (a) and streamlines (b) of the axial velocity and temperature contour (c) for methane flameless combustion.

Figure 5.4 c shows that combustion occurs at temperatures well below the adiabatic flame temperature and that the temperature field is characterized by thick regions of relatively uniform temperature and smooth temperature gradients caused by the recirculation of the flue gases and the heating of the reactants by these gases.

In the next subsection, the axial profiles of velocity, temperature and concentrations of the most relevant species for the different fuels studied are presented. Then, the temperature contours and the contours of the normalized deviation of the predicted temperature (T*) are presented to observe the temperature distribution inside the combustion chamber. To close this chapter, the average values of the flue gases recirculation rate and the emissions at the combustor outlet are presented.

5.3.1 Axial Profiles of the Relevant Parameters for Different Fuels

Figure 5.5 shows the axial profiles of velocity (Ux), temperature and concentrations of O_2, CO_2, CO, NO_x, soot and unburned hydrocarbons (HC) for the following fuels: methane (CH_4), propane (C_3H_8), acetylene (C_2H_2), biogas and ethanol. The biogas used in the work consists of a mixture of 60% CH_4 and 40% CO_2 in molar fraction. This biogas composition was also studied experimentally and numerically by Hosseini *et al.* [17, 40] to obtain flameless combustion.

From figure 5.5, it is observed that the velocity profiles are similar regardless of the air and fuel inlet velocities, the fuel inlet temperature and the type of fuel used. Until the position x ≈ 5 mm, there is a slight reduction in velocity and then a progressive velocity increase to the position x ≈ 100 mm. In this point, the maximum velocity is reached and then the velocity decreases until it becomes constant downstream of the point x = 400 mm. The velocity reduction of the fuel jet observed at the beginning

occurs because, according to equation 5.1, the temperature increase in that initial region is less than the increase of the jet cross-sectional area.

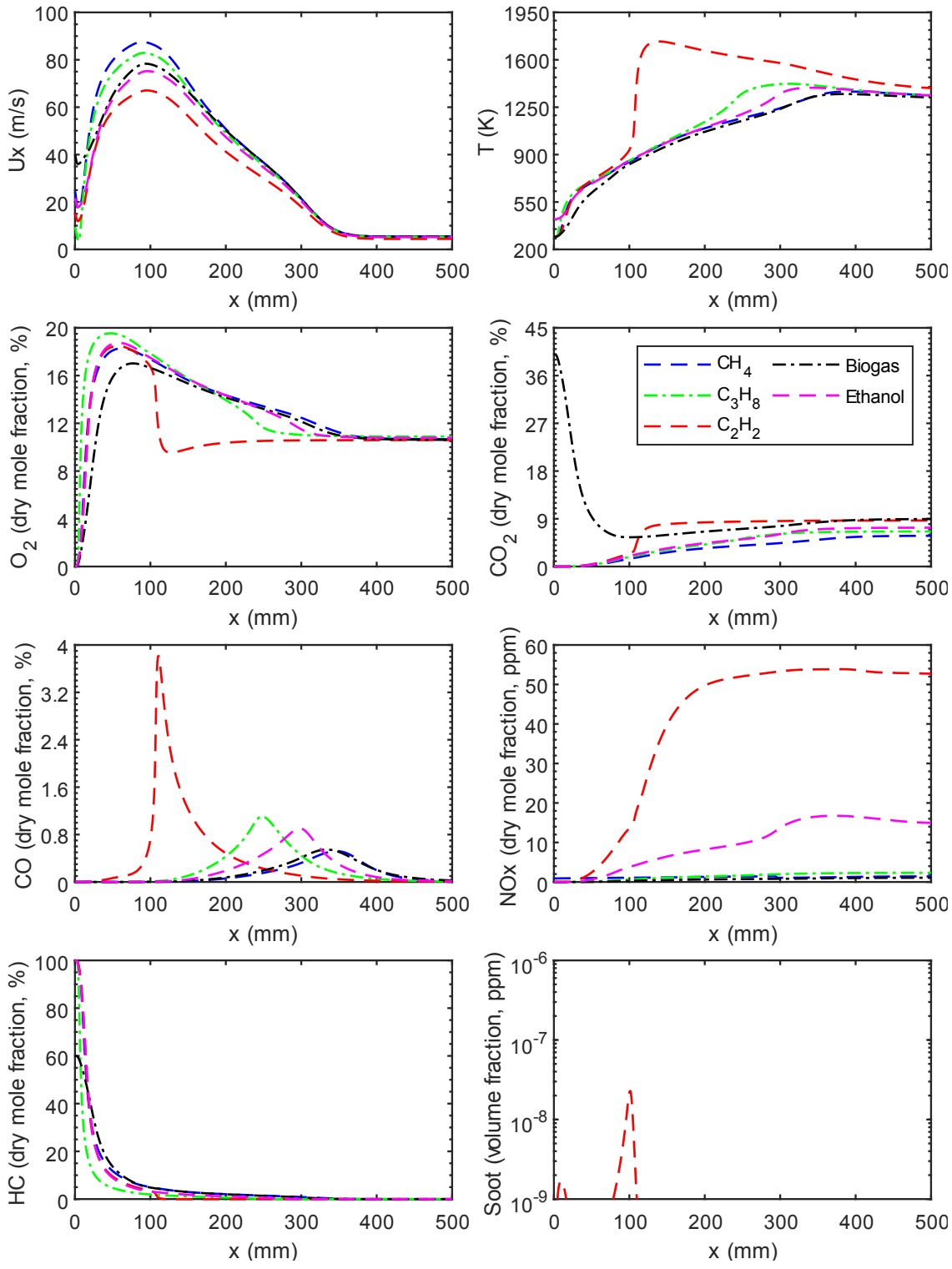

Figure 5.5 - Axial profiles of velocity, temperature, O_2, CO_2, CO, NO_x, HC and soot concentrations for combustion of methane, propane, acetylene, biogas and ethanol.

The minimum velocity recorded at the point x = 5 mm occurs when the air and fuel jet shear layers merge. From this point, a fuel jet acceleration occurs because the air jet velocity is higher than the fuel

jet velocity, which performs a momentum transfer to the fuel jet. The acceleration of the central jet also occurs because the temperature increase compensates the increase of the jet cross-sectional area according to equation 5.1. Downstream of the point x = 100 mm, the jet velocity decreases because the temperature increase of the central jet does not compensate the increase of the jet cross-sectional area, but also due to momentum transfer to the recirculated flue gas, which has a lower velocity compared to the reactants.

$$\frac{U_{x_2}}{U_{x_1}} = \frac{A_{x_1}}{A_{x_2}} \cdot \frac{T_{x_2}}{T_{x_1}} \tag{5.1}$$

Based on figure 5.5, it is observed that the temperature and the O_2, CO_2, CO and NO_x concentration profiles for CH_4, C_3H_8, biogas and ethanol have similar behavior. The maximum temperatures differ because the fuels have different adiabatic flame temperatures, with the higher adiabatic flame temperature in propane followed by ethanol, biogas and methane. The maximum temperature, O_2, CO_2 and CO concentrations also differ since the air-fuel ratio and the chemical composition differ from fuel to fuel.

According to the CO concentration profiles present in figure 5.5, it is observed that the onset of CO oxidation occurs for different positions depending on the fuel used and for different CO consumption rates. In acetylene, combustion occurs after the position x = 100 mm and the CO consumption rate is much higher than the CO consumption rates observed for other fuels. In propane, it is observed that the CO consumption occurs at x = 250 mm and, for ethanol, biogas and methane, the onset of CO consumption takes place between x = 300 mm and x = 350 mm which corresponds to the combustion chamber section where the reduction of the cross-sectional area takes place.

In relation to acetylene, it can be seen in figure 5.5 that at x = 100 mm a significant increase in temperature and CO_2 and NO_x concentrations occurs, which is accompanied by a significant reduction in O_2 and CO concentrations. The variations occurring at this point indicate the presence of a flame inside the combustion chamber although the maximum temperature (T_{max} = 1736 K) is much lower than the adiabatic flame temperature of acetylene (T_{ad} = 2607 K). In the acetylene combustion, there is a tendency for soot formation, although the combustion takes place in fuel-lean condition and the presence of a homogeneous concentration of oxygen inside the combustion chamber, which reduces the appearance of incomplete or partial combustion zones of C_2H_2. For these working conditions, there was not soot formation in the propane combustion since the temperatures recorded inside the combustion chamber are lower than the minimum temperature required for soot formation in non-premixed combustion. According to Glassman *et al.* [87], the minimum temperature for soot formation is 1600 K.

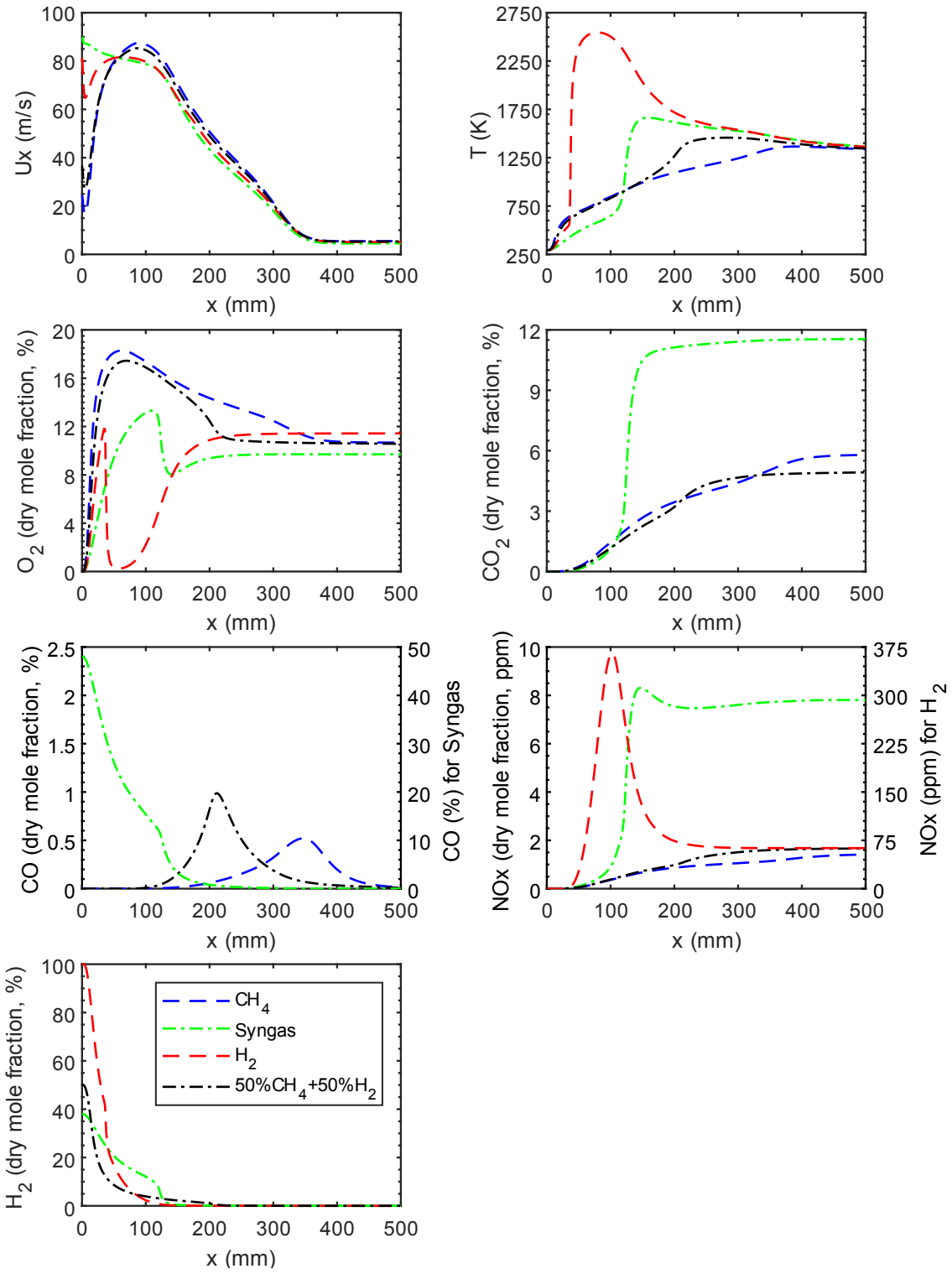

Figure 5.6 – Axial profiles of velocity, temperature, O_2, CO_2, CO, NO_x and H_2 concentrations for combustion of methane, syngas, hydrogen and 50% CH_4 + 50% H_2.

Figure 5.6 shows the axial profiles of velocity, temperature and O_2, CO_2, CO, NO_x and H_2 mole fractions on a dry basis for the following fuels: methane, syngas, hydrogen (H_2) and a mixture composed of 50% CH_4 and 50% H_2 by volume. The syngas used in this work has the following composition by volume: 48% CO, 38% H_2 and 14% N_2 [47].

According to figure 5.6, the velocity profiles for the 50%CH_4/50%H_2 mixture and H_2 follow the same trend as the CH_4 velocity profile where there is a reduction of the fuel jet velocity in the vicinity of the burner. Subsequently, there is an acceleration of the jet until reaching the maximum value and finally it decreases until reaching a constant value at the combustion chamber outlet. In relation to syngas, there is an absence of the first two phases in the velocity profile since the air jet velocity is lower than the fuel jet velocity, which means that the entrainment effect that promoted the acceleration of the fuel jet does not exist. Therefore, a gradual reduction in velocity is observed up to the position x ≈ 400 mm from which the velocity remains constant.

The data available for the combustion of the 50%CH_4/50%H_2 mixture in figure 5.5 show that the temperature and species concentration profiles follow a similar behavior to those obtained in methane flameless combustion. The maximum temperature for this mixture is expected to be higher than the maximum temperature for methane because the adiabatic flame temperature of this mixture (T_{ad} = 2286 K) is higher than the adiabatic flame temperature of methane (T_{ad} = 2236 K). The CO concentration profile for this mixture in figure 5.6 shows that the CO oxidation occurs beyond the point x ≈ 210 mm and small variations are observed in the temperature and O_2 and CO_2 concentration profiles for this same point. This point shows the onset of the reaction zone.

According to the available data for syngas in figure 5.6, it can be seen a rapid increase in temperature CO_2 and NO_x concentrations at x = 110 mm which is accompanied by a sharp reduction in the concentrations of O_2, CO and H_2. In flameless combustion, the temperature profile is characterized by smooth temperature gradients while in conventional combustion there is a sudden temperature increase followed by a smooth temperature decrease when moving away of the flame front. In syngas there is an increase of approximately 950 K from the point x = 110 mm to the point x = 160 mm where the maximum temperature occurs. This sudden temperature increase suggests the appearance of a flame inside the combustion chamber.

In hydrogen combustion, there is a sudden variation in temperature and species concentration at x = 36 mm, see figure 5.6. In the temperature profile, there is a temperature increase of approximately 1920 K between the point x = 36 mm and the point x = 80 mm, which suggests the presence of flame inside the combustion chamber. The available O_2 concentration data in figure 5.6 show an almost total O_2 consumption in a length of 21 mm, followed by an O_2 concentration increase to 11.5% in H_2 combustion. The radial O_2 concentration profiles present in appendix A.3 show a low O_2 concentration on the symmetrical axis, followed by an O_2 concentration increase until radial position of 15 mm and this phenomenon is observed in the axial position of 90 mm.

The radial temperature profiles available in appendix A.3 suggest that the wall temperature defined in the boundary conditions is not suitable for this simulation. Between the positions x = 90 mm and x = 150 mm, the system needs to transfer a huge amount of heat to the outside in order to compensate the temperature differential above 1000 K between the symmetrical axis and the combustor wall. To decrease this temperature difference, it is necessary to increase the temperature of the combustor walls. In practice, pure H_2 is not burnt in a combustion chamber due to the high temperatures recorded in the

walls, which leads to rapid wear of the material and changes in the physical properties of the combustor material.

Due to the growing interest in ammonia (NH_3) combustion as a carbon-free fuel, the next paragraphs of this subsection will be dedicated to analyzing and discussing the results obtained in simulations of ammonia mixed with methane or hydrogen. In this work, the influence of the NH_3 concentration in mixture and the equivalence ratio were studied. Table 5.1 shows the NH_3 concentrations in the mixture and the equivalence ratios studied.

Table 5.1 – Different NH_3 concentrations in the mixture and the equivalence ratios studied.

Mixture	**H_2 (mole fraction, %)**	**CH_4 (mole fraction, %)**	**NH_3 (mole fraction, %)**	**φ**
1	—	30	70	0.5
2	—	20	80	0.5
3	—	20	80	2/3
4	—	20	80	1
5	—	20	80	1.2
6	30	—	70	0.5
7	20	—	80	0.5
8	20	—	80	2/3
9	20	—	80	1
10	20	—	80	1.2

From figure 5.7, it is observed that the velocity profiles are similar to the methane velocity profile when the equivalence ratio is less than 1 and is independent of the NH_3 concentration in the mixture. For the same NH_3 concentration, the maximum jet velocity decreases when the equivalence ratio increases. The maximum velocity decreases for $\varphi \leq 1$ because the air mass flow rate decreases when the φ increases, which decreases the momentum transfer to accelerate the central jet. For $\varphi > 1$, the jet velocity is maximum at the injector outlet since the air jet velocity is less than the fuel jet velocity. In this case, there is a momentum transfer from the fuel jet to air jet, which tends to slow down the fuel jet velocity.

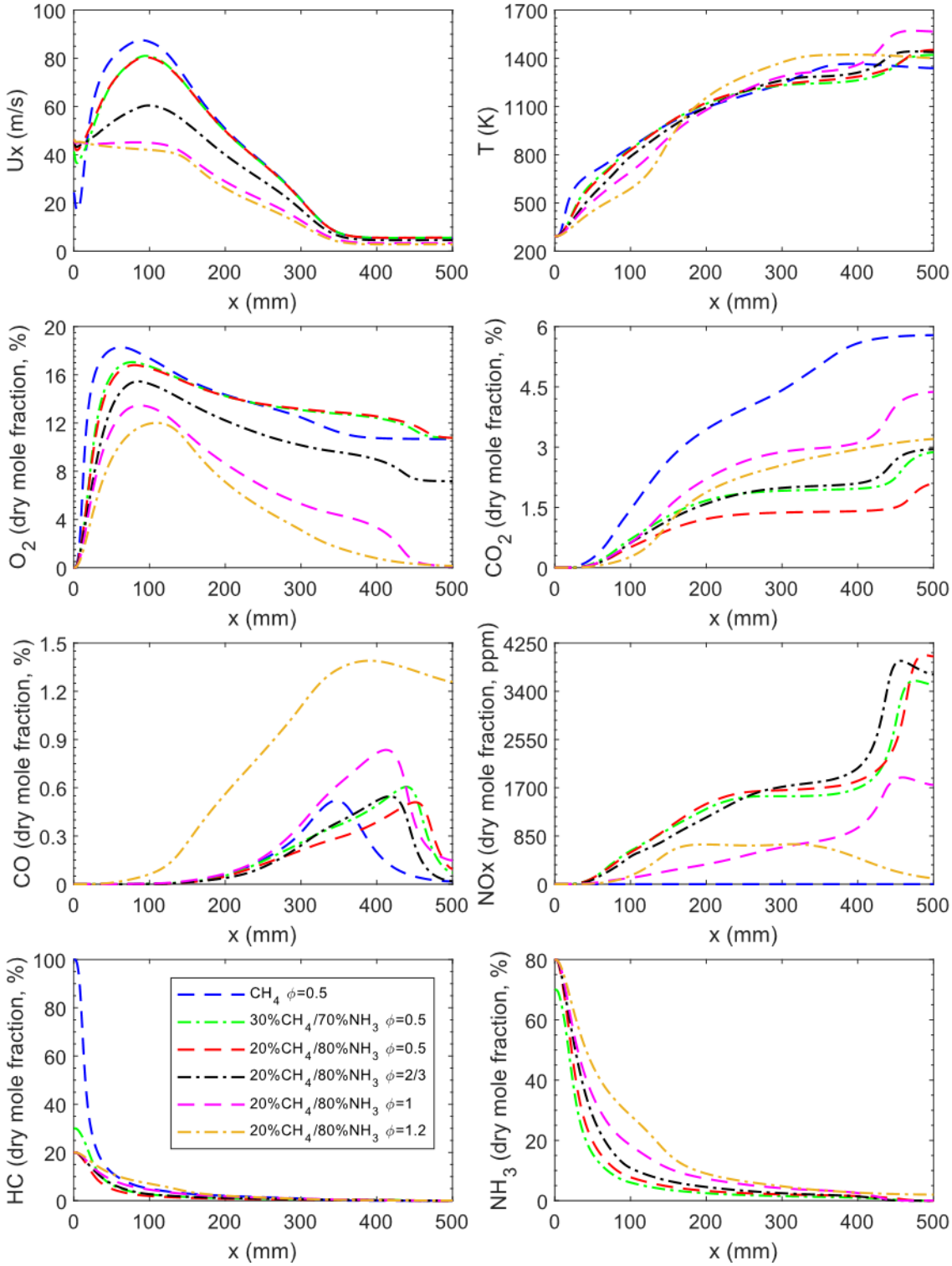

Figure 5.7 – Axial profiles of velocity, temperature, O_2, CO_2, CO, NO_x, HC and NH_3 concentration for combustion of different CH_4/NH_3 mixture and equivalence ratios studied.

In figure 5.7, it is observed that the temperature profiles obtained for mixtures with φ ≤ 1 have a similar behavior to the methane temperature profile. For these mixtures, there is a moderate temperature increase downstream of x = 400 mm, which is also observed in the CO_2 and NO_x concentration profile and a decrease of O_2 and CO concentration after this point. For φ = 1.2, a temperature increase of approximately 565 K is observed between the points x = 100 mm and x = 200 mm although for other

equivalence ratios there is a temperature increase below 400 K for the same distance covered. After that, a moderate temperature increase is observed up to the point x = 300 mm followed by a temperature plateau until the combustion chamber outlet.

The O_2 concentration profiles in figure 5.7 show that regardless of the NH_3 concentration in the mixture and the equivalence ratio used, the profiles behave similarly to the O_2 concentration profile in CH_4. It is expected that the O_2 concentration at the combustor outlet will decrease with equivalence ratio increase and that for stoichiometric and fuel-rich conditions, the O_2 concentration at the exit will be zero.

In figure 5.7, it can be seen that CO_2 emission decreases when the CH_4 concentration in the mixture decreases for the same equivalence ratio. For the same CH_4 concentration in the mixture, it appears that the CO_2 concentration increases with the equivalence ratio up to $\varphi = 1$. This happens because the onset of CO to CO_2 conversion occurs in a region close to the combustion chamber outlet, typically for $x \geq 400$ mm, which causes an appreciable CO concentration at the combustor outlet.

The NO_x concentration data in figure 5.7 shows that for $\varphi < 1$ there is a higher tendency for NH_3 to oxidize and form NO_x and that for $x > 400$ mm there is a significant increase in NO_x concentration since the CO and CH_4 promote the formation of a radical pool consisting essentially of O, H and OH that accelerate the reaction rates and favor the ammonia oxidation pathways [88]. For fuel-rich conditions, the NO_x concentration is less than under fuel-lean conditions since NH_3 is more propense to undergo pyrolysis than to oxidize, with N_2 and H_2 being the pyrolysis products. The NO_x concentration decreases downstream of point x = 314 mm because the NO_x consumption rate is higher than the NO_x formation rate. The NOx consumption is done essentially through the following chemical reaction [89]:

$$NO + NH_2 \Leftrightarrow N_2 + H_2O$$

From the studied conditions, it is observed that the mixture with $\varphi = 2/3$ is the most suitable for the size of the combustion chamber used due to the low CO, HC and NH_3 emissions while the other conditions studied require a larger combustion chamber.

From figure 5.8, it can be seen that the velocity profiles of the H_2/NH_3 mixtures have similar behavior to the velocity profiles of CH_4/NH_3 mixtures. Regarding the O_2 concentration data, figure 5.8 shows that the O_2 concentration profiles of the studied H_2/NH_3 mixtures have the same tendency as the O_2 concentration profile in CH_4 combustion. As the equivalence ratio increases, the expected O_2 concentration at the combustor outlet decreases and decreases to zero for $\varphi \geq 1$.

The NH_3 and H_2 concentrations, see figure 5.8, indicate that when the equivalence ratio increases, the time needed to dilute NH_3 and H_2 increases, especially in the first half of the combustion chamber. This lower dilution rate is due to the lower air jet velocity when the equivalence ratio increases. For $\varphi = 1.2$ there is an H_2 concentration increase in the second half of the combustion chamber. This phenomenon happens because the ammonia has a greater tendency to pyrolyze and form N_2 and H_2 instead of oxidizing for fuel-rich conditions [88]. This H_2 concentration in the order of 5% is also present in the

recirculation zones and near the wall, as can be seen in the radial H_2 concentration profiles present in appendix A.5.

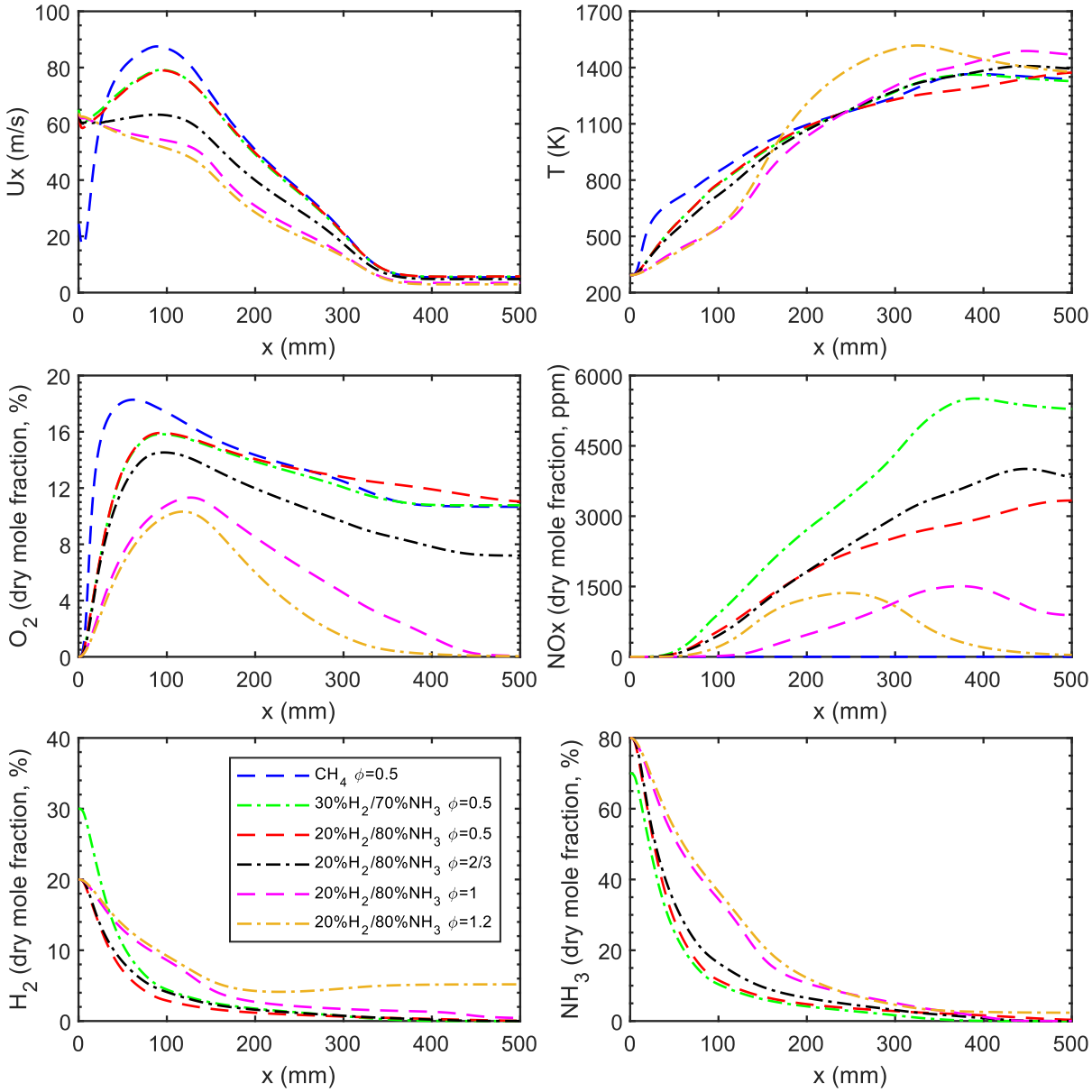

Figure 5.8 – Axial profiles of velocity, temperature, O_2, CO_2, CO, NO_x, H_2 and NH_3 concentrations for combustion of different H_2/NH_3 mixture and equivalence ratios studied.

When the NH_3 concentration in the fuel decreases, the NO_x concentration increases for the same equivalence ratio, see figure 5.8. According to Wendt and Sternling [88], this phenomenon happens because the percentage of NH_3 to NO_x conversion is dependent on the NH_3 concentration in the fuel. When the NH_3 concentration in the fuel increases, the conversion rate decreases since NH_3 has a self-inhibiting oxidation effect. At the combustor outlet, it is observed that for stoichiometric or fuel-rich conditions the NOx concentration is lower than in fuel-lean conditions. For $\varphi \geq 1$, the NO_x consumption occurs in the second half of the combustion chamber because the ammonia is partially cracked after

the heating period in which the NH_2 radicals are obtained. The NH_2 radicals react with NO to produce N_2 in lower temperature regions [90].

In figure 5.8, it is observed that in fuel-lean conditions, NO_x concentration is lower for φ = 2/3 than for φ = 0.5. This happens because for the condition φ = 2/3 there is a higher NH_3 to NO_x conversion due to the higher concentration of the radicals O, H and OH in relation to the last condition. For this reason, at the combustor outlet, the condition φ = 2/3 emits only 0.0016% H_2 and 0.0014% NH_3 compared to 0.036% H_2 and 0.296% NH_3 emitted in the condition φ = 0.5.

5.3.2 Temperature Contours

This section presents the temperature contours and the contours of the normalized deviation of the predicted temperature for all fuels studied in this work. The normalized deviation of the predicted temperature (T^*) is a dimensionless parameter that assesses the uniformity of the temperature field and is defined as:

$$T^* = \frac{T_{measured} - \bar{T}}{\bar{T}} \tag{5.2}$$

where $T_{measured}$ is the measured local temperature and $\bar{T}$ is the average temperature over all of the combustion chamber.

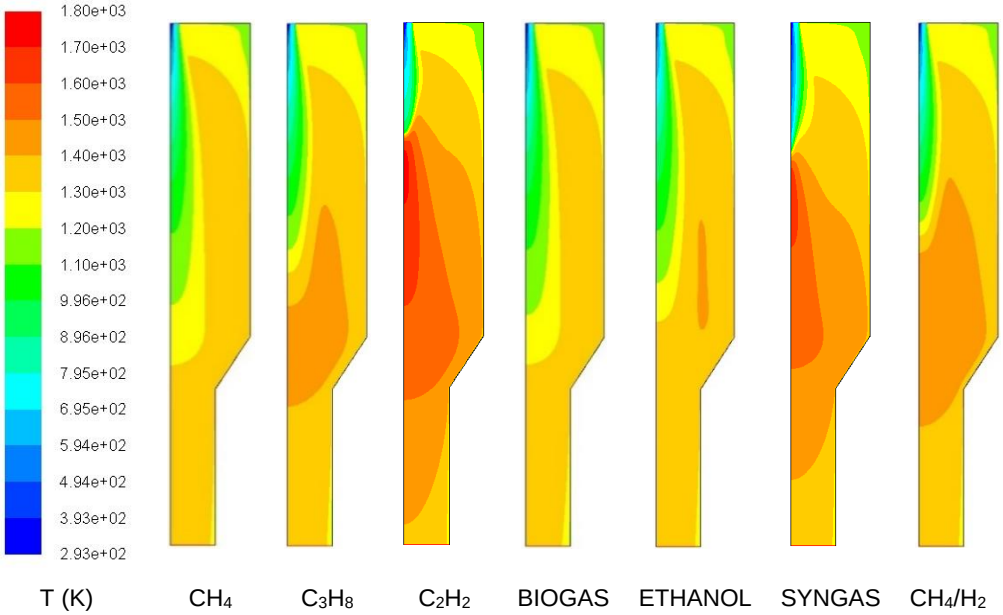

Figure 5.9 – Temperature contours of carbon fuels for the same equivalence ratio, φ = 0.5.

Figure 5.9 reveals that there are extensive regions inside the combustion chamber that are in the same temperature range. The axial and radial profiles available in figures 5.5 and 5.6 and appendixes A.2 and A.3 are consistent with the temperature contours shown in figure 5.9. Through the radial temperature profiles and temperature contours, smooth temperature gradients are observed in all fuels except acetylene and syngas. The temperature contours of C_2H_2 and syngas have mean temperatures above

1600 K and these temperatures are restricted to a small region located on the axis symmetry. However, the flue gas temperature is higher in acetylene combustion than in syngas combustion.

Figure 5.10 shows that the methane, ethanol and biogas highest temperature regions are thick and elongated starting in the recirculation zone and finishing at the combustion chamber outlet. The corresponding high temperature zones of propane and the CH_4/H_2 mixture are U-shaped, beginning in the recirculation zone and extending to the section where there is a cross-sectional area reduction. These zones are thicker in the propane and the CH_4/H_2 mixture combustions. In case of C_2H_2 and syngas, it seems that the high temperature zones are thin and close to the symmetry axis and the temperature fields are less uniform than the temperature field in CH_4. As the methane combustion occurs in flameless combustion mode, based on the comparison of the temperature and T* contours, as well as the velocity and chemical species concentration profiles in figures 5.5 and 5.6, it is believed that this combustion mode also occurs in the propane, biogas, ethanol and CH_4/H_2 combustion, despite the absence of experimental results and of excited OH radical contours, which would allow drawing more reliable conclusions about the combustion mode. However, the acetylene and syngas combustion are likely to occur in conventional non-premixed combustion mode, due to the presence of larger temperature gradients and less uniform temperature and species concentration fields.

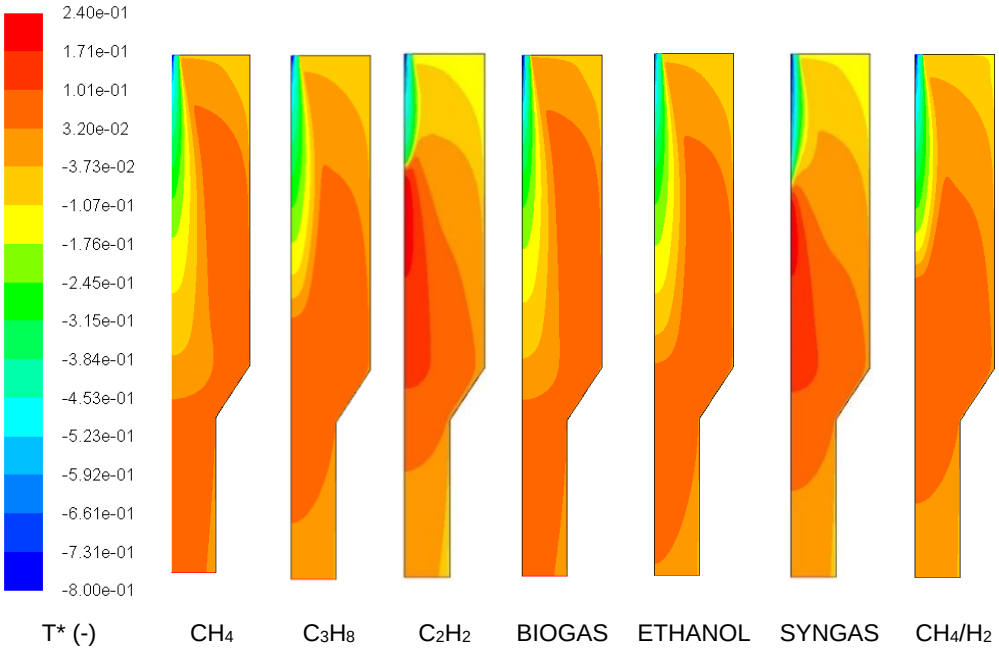

Figure 5.10 – Contours of the normalized deviation of measured temperature of carbon fuels for the same equivalence ratio, φ = 0.5.

The axial and radial profiles in figure 5.6 and Appendix A.3 are consistent with the temperature contours presented in figure 5.11 for H_2 combustion. These results show the presence of a thin region of high temperatures close to the axis of symmetry and the predicted temperatures are close to the adiabatic flame temperature of hydrogen. It can also be seen the presence of strong axial and radial temperature gradients. The T* contours of hydrogen are completely different from the ones obtained for methane, which suggests that the H_2 combustion occurs in the conventional non-premixed combustion, such as acetylene and syngas.

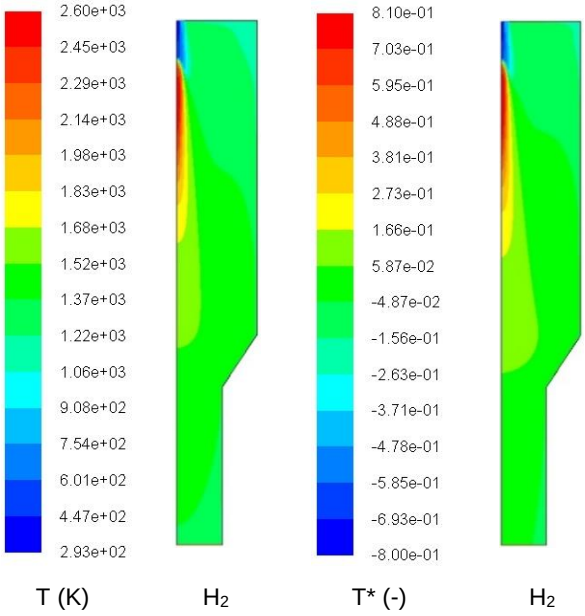

Figure 5.11 – Temperature and normalized deviation of the predicted temperature (T*) contours of H_2.

Figure 5.12 shows that for fuel-lean and stoichiometric conditions of CH_4/NH_3 mixtures, there are two hotter regions located in the recirculation zone and close to the combustion chamber outlet. For $\varphi \leq 1$, it is also observed that when the NH_3 concentration in the mixture or the equivalence ratio increases, these hot regions are thicker. Based on figure 5.12 and the radial temperature profiles available in appendix A.4, it indicates that the temperature gradients are smooth for conditions with $\varphi \leq 1$. However, a thin and elongated region is observed between x = 30 mm and x = 150 mm for $\varphi = 1.2$.

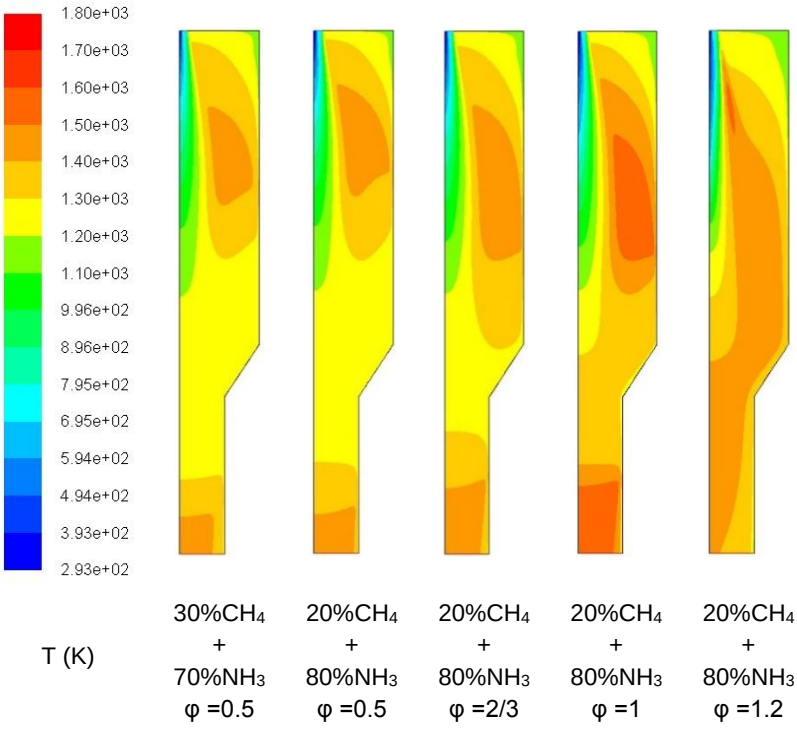

Figure 5.12 – Temperature contours for different chemical compositions and equivalence ratios studied for CH_4/NH_3 mixtures.

The T* contours in figure 5.13 reveal that the high temperature zone grows when the NH_3 concentration in the CH_4/NH_3 mixture increases and when the equivalence ratio increases until the stoichiometric condition is reached. Although there are small elliptical regions with a higher T* value under stoichiometric condition, these regions do not suggest the presence of a flame front because there is no sudden temperature increase in the axial and radial temperature profiles shown in figure 5.7 and Appendix A.4. For the fuel-rich condition, a thin and elongated region with higher T* value between x = 30 mm and x = 150 mm is observed. Based on the temperature and T* contours and chemical species concentration profiles presented in figure 5.7, it is likely that flameless combustion occurs with $\varphi \leq 1$, while the fuel-rich condition ($\varphi = 1.2$) leads to conventional non-premixed combustion mode, despite the absence of experimental results to confirm this.

The temperature contours in figure 5.14 show the appearance of higher temperature regions when the NH_3 concentration in the H_2/NH_3 mixture is 80%. These regions grow when the equivalence ratio increases and the flue gas temperature is higher in the stoichiometric condition. The appearance of two hot regions occurs for $\varphi \geq 2/3$, one region located in the recirculation zone and the other one located at the combustion chamber outlet.

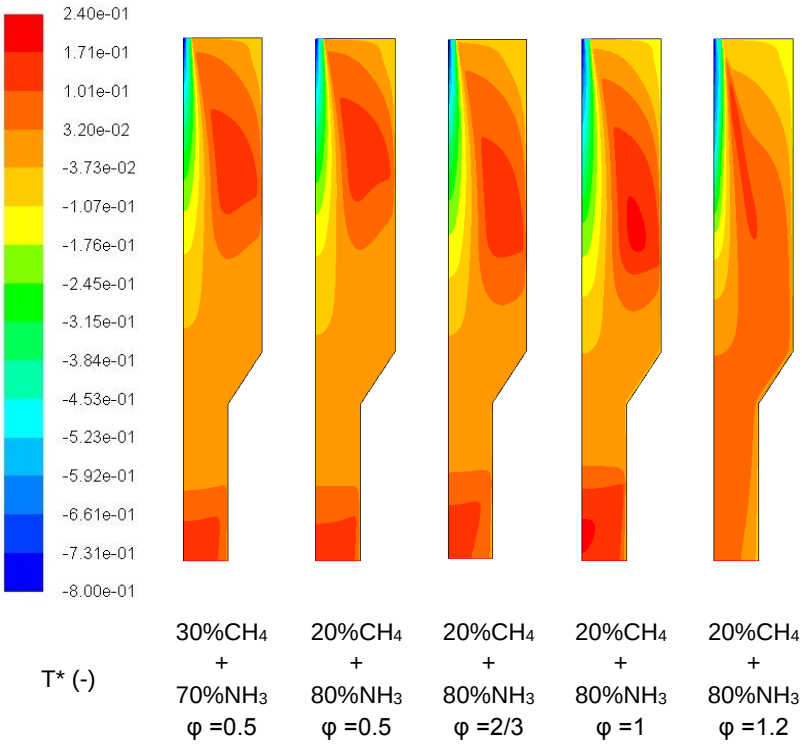

Figure 5.13 – Normalized deviation of the predicted temperature contours for different chemical compositions and equivalence ratios studied for CH_4/NH_3 mixtures.

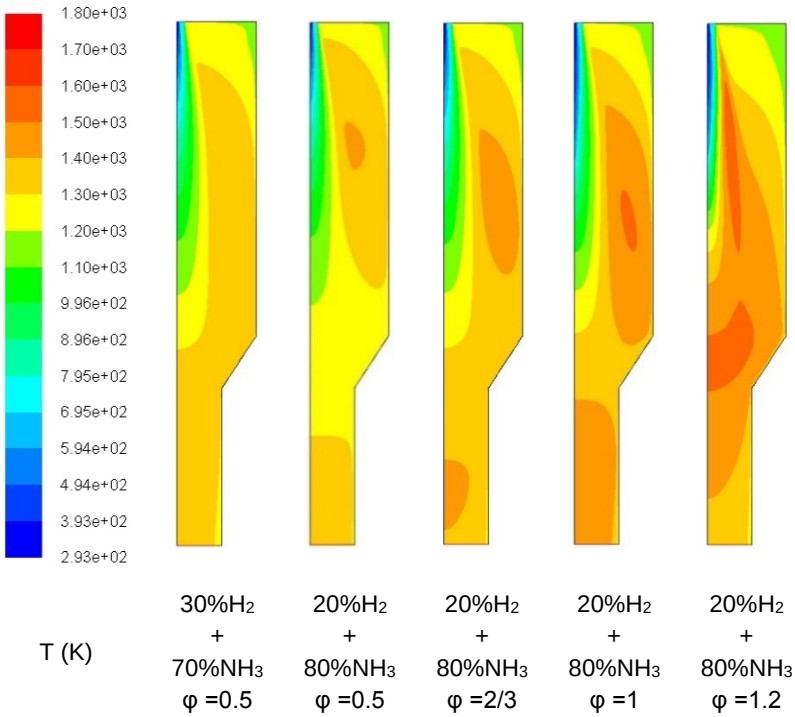

Figure 5.14 – Temperature contours for different chemical compositions and equivalence ratios studied for H_2/NH_3 mixtures.

In figure 5.15, it is observed the presence of two high temperature zones for $\varphi \geq 0.5$ and NH_3 concentration of 80%, one of them is in the recirculation zone and the other one is close to the combustion chamber outlet, except for $\varphi = 1.2$ where the second zone is located in the cross-sectional area reduction zone. The locations of these zones do not depend on the fuel mixed with the ammonia, but the high temperature zones present in CH_4/NH_3 mixtures are more intense compared to those present in H_2/NH_3 mixtures. For $\varphi = 1.2$, a thin and elongated zone is observed and is located between x = 30 mm and x = 210 mm and for a radius above 15 mm. This region is accompanied by a sudden temperature increase followed by a significant temperature reduction present in radial temperature profiles between x = 30 mm and x = 210 mm, see Appendix A.5. Based on figures 5.8, 5.14 and 5.15, it can be assumed that flameless combustion occurs for $\varphi \leq 1$ and the conventional non-premixed combustion takes place for $\varphi = 1.2$.

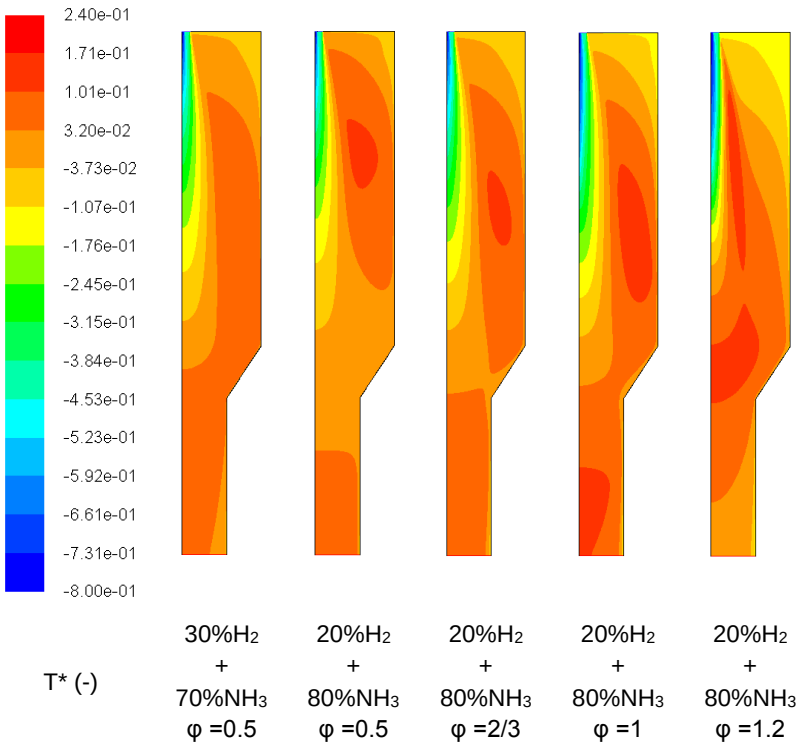

Figure 5.15 – Normalized deviation of the predicted temperature contours for different chemical compositions and equivalence ratios studied for H_2/NH_3 mixtures.

5.4 Flue Gas Emissions

To close this chapter, the flue gas concentration and the flue gas recirculation rate for each fuel studied is presented. The flue gas recirculation rate is defined as the ratio of the internal flue gas recirculation mass flow rate to the sum of the fuel and air mass flow rates at the burner inlet, see equation 2.5.

From table 5.2, it can be seen that the syngas has the lowest flue gas recirculation rate (K_v = 1.99) while methane has the highest flue gas recirculation rate (K_v = 2.15). According to the K_v definition, this parameter is dependent on the air mass flow rate , which is a function of the stoichiometric air-fuel ratio. In this case, when the stoichiometric air-fuel ratio decreases, the flue gas recirculation rate decreases.

Table 5.2 – The recirculation rate and respective flue gas emissions on dry molar basis for nitrogen-free fuels.

Fuel	φ	K_v	Flue gas emissions				
			CO_2 (%)	CO (ppm)	NO_x (ppm)	UHC (ppm)	H_2 (ppm)
CH_4	0.5	2.15	5.8	138.9	1.4	≈ 0	—
C_2H_2	0.5	2.02	8.7	44.0	52.7	≈ 0	—
C_3H_8	0.5	2.13	6.6	66.3	2.3	≈ 0	—
Biogas	0.5	2.06	9.0	228.7	1.1	≈ 0	—
Ethanol	0.5	2.07	7.3	93.5	14.9	≈ 0	—
Syngas	0.5	1.99	11.5	34.9	7.8	—	3.0
50% CH_4/50% H_2	0.5	2.12	4.9	81.4	1.7	≈ 0	3.9
H_2	0.5	2.10	—	—	63.0	—	2.1

The CO_2 concentration is less than 12% for any fuel tested although methane and biogas emit more than 100 ppm of CO, see table 5.2. The high CO content in biogas is due to the fact that biogas has a significant CO_2 concentration in its composition, which tends to act as an oxidizing agent in environments of higher temperatures. In both fuels, the reaction zone starts beyond the point x = 300 mm, which means that the combustion chamber is not long enough for total oxidation of CO.

According to the NOx emissions in table 5.2, the acetylene combustion emits about 53 ppm of NO_x, while ethanol emits around 15 ppm of NO_x and the remaining fuels emit less than 8 ppm of NO_x. In case of H_2 combustion, the amount of NOx emitted is around 63 ppm at combustor outlet. This amount of NOx emitted is due to the fact that the thermal-NO mechanism contributes significantly to the NOx formation since temperatures above 1800 K are observed, followed by the intermediate N_2O-route and prompt mechanisms. According to Bal [91], the responsible NO_x formation mechanisms in flameless combustion are the thermal-NO and intermediate N_2O-route mechanisms, although the temperature range recorded in this work is less than 1800 K, which is the minimum temperature at which the thermal-NO mechanism has an expressive response. Based on this, it is expected that the contribution of the thermal-NO mechanism in the NO_x formation will be higher in the acetylene combustion than in the other fuels since acetylene combustion exhibits higher temperatures.

Based on the temperature and concentration profiles analyzed above and with the NO_x concentration in exhaust gas shown in table 5.2, the flameless combustion is characterized by NO_x emissions lower than 15 ppm for carbon-based fuels.

Table 5.3 – The recirculation rate and respective flue gas emissions on dry molar basis for NH_3 mixture studied.

Fuel	φ	K_v	Flue gas emissions					
			CO_2 (%)	CO (ppm)	NO_x (ppm)	UHC (ppm)	H_2 (ppm)	NH_3 (ppm)
30% CH_4/70% NH_3	0.5	2.15	2.9	478.9	3471.8	3.0	—	11.0
20% CH_4 /80% NH_3	0.5	2.14	2.1	607.8	3917.3	7.6	—	63.3
	2/3	1.89	3.0	122.9	3658.5	0.3	—	2.8
	1	1.74	4.4	1247.9	1682.7	0.2	—	4.1
	1.2	1.69	3.2	12471.4	89.7	658.5	—	≈ 2.0%
30% H_2 /70% NH_3	0.5	2.02	—	—	5274.5	—	1.6	0.2
20% H_2 /80% NH_3	0.5	2.07	—	—	3266.8	—	357.8	2956.0
	2/3	1.89	—	—	3782.8	—	16.7	14.1
	1	1.75	—	—	867.9	—	3968.3	1.0
	1.2	1.71	—	—	34.2	—	≈ 5.2%	≈ 2.4%

In CH_4/NH_3 mixtures, when the NH_3 concentration in the mixture increases, the recirculation rate decreases, see table 5.3. This happens because of the stoichiometric O_2 amount required to convert a mole of this fuel decreases, i.e. the stoichiometric air-fuel ratio decreases. However, in H_2/NH_3 mixtures, the recirculation rate increases with the NH_3 concentration in fuel. In this mixture, when the NH_3 concentration increases, the number of hydrogen atoms increases in contrast to what is observed in

CH_4/NH_3 mixtures. As the number of hydrogen atoms in the fuel increases, so the oxygen content for stoichiometric combustion increases, i.e. the stoichiometric air-fuel ratio increases.

In both mixtures, when the equivalence ratio increases, the flue gas recirculation rate significantly decreases, see table 5.3. Tables 5.2 and 5.3 show that the flue gas recirculation rate is strongly dependent on the equivalence ratio, followed by the stoichiometric air-fuel ratio and finally the fuel composition.

For $\varphi \leq 1$, the CH_4/NH_3 mixtures show a higher CO concentration (see table 5.3) because the beginning of the CO oxidation is close to the combustor outlet, which means that the combustion chamber is not long enough to promote the total oxidation of CO. In the fuel-rich condition, oxygen is not enough to complete combustion of the CH_4/NH_3 mixture, which promotes high CO and fuel emissions despite low NO_x emissions.

Both mixtures have low NO_x emissions in fuel-rich conditions because ammonia, in oxygen-poor environments, tends to pyrolyze and form N_2 and H_2 and also the NO_x consumption that is associated to recombination of NO with NH_2 radicals. For this reason, the H_2/NH_3 mixture presents a concentration of H_2 in order of 5% despite its reactivity.

Finally, flameless combustion of CH_4/NH_3 and H_2/NH_3 mixtures is expected to be possible with this combustor. However, it is necessary to optimize this small-scale combustor in order to reduce NO_x emissions to make ammonia flameless combustion a viable alternative to flameless combustion of carbon fuels.

6. Conclusions and Future Work

6.1 Conclusions

The numerical simulations of a small-scale combustor operating in a flameless combustion mode have been conducted. The main objective of this work was to study the flexibility of this combustor to burn different fuels in order to obtain the flameless combustion mode, in the other words, to study the influence of the fuel to obtain flameless combustion in the same combustor and the operating conditions, namely the equivalence ratio, the air inlet temperature and wall temperature and emissivity for a thermal input of 10 kW. In order to optimize the setup of the simulations, a study of the independence of the grid was initially made, then the influence of the turbulence models and finally the influence of the fuels proposed in this work were studied. The study of the influence of fuels on the combustor was made using the realizable k-ε for turbulence model and the species transport model used was EDC coupled with a detailed kinetic mechanism suitable for each studied fuel, the kinetics mechanisms used are shown in table 4.4.

As a result of the grid independence study, the velocity, temperature, O_2 and CO_2 concentration fields are similar for the three meshes. However, the CO concentration field exhibits little differences in the three meshes and in the NO_x concentration field the coarse mesh differs in relation to the other two studied grids. Having in mind the computational time and the differences between the three meshes in the studied are less than the uncertainty in the measurement instruments used by Rebola *et al.* [59], the intermediate mesh with 79 000 elements was chosen for the following simulations.

The study of the influence of the turbulence model reveals that the three tested models produce satisfactory results in comparison with the experimental data. The tested models were the SST k-ω, standard k-ε, realizable k-ε models and keeping in mind the computational time and the use of more rigorous convergence criteria, it is observed that the realizable k-ε and standard k-ε models reach the convergence criteria in less time than the SST k-ω model. However, the realizable k-ε model does not have the need to change the relaxation factors of the species residues in relation to the standard k-ε model. Therefore, the realizable k-ε model was chosen to study the influence of fuel on this small-scale combustor in flameless combustion regime.

All fuels were simulated, and only methane provided essential experimental data for the validation of the turbulence, species transport and radiation models. The main conclusions of the results presented and discussed in chapter 5 are as follows:

- The combustion of propane, biogas and ethanol is likely to occur in flameless combustion mode in which NO_x emissions below 2.5 ppm are observed for propane and biogas and about 15 ppm for ethanol. Regarding CO concentration, it is observed that biogas emits more than 200 ppm while ethanol and propane emit less than 100 ppm. This increase in CO emission in biogas is due to the fact that CO_2 in high concentration and at high temperatures behaves as an oxidizing agent.

- Acetylene and syngas are two fuels where the flameless combustion mode is not achieved, but conventional non-premixed combustion occurs. However, CO and NO_x emissions are less than 45 ppm and 53 ppm, respectively. These results indicate that in this combustor it is also possible to perform conventional non-premixed combustion with low CO and NO_x concentrations due to the presence of strong internal flue gas recirculation rates.
- Regarding the soot formation, there is no soot formation in the flameless combustion of propane and soot formation in the acetylene combustion. The absence of soot in combustion of propane is due to the fact that the combustion of this fuel takes place at a temperature lower than the minimum temperature at which there is a tendency for the soot formation. In relation to acetylene, the soot concentration is low due to the temperature difference between the maximum temperature and the minimum temperature for which soot formation occurs is small and the homogeneity of the O_2 concentration inside the combustion chamber.
- Flameless combustion is expected to perform in the CH_4/H_2 mixture, while the hydrogen combustion takes place in conventional non-premixed combustion mode. In the CH_4/H_2 mixture, CO and NO_x emissions are less than 100 ppm and 2 ppm, respectively. In hydrogen combustion, the flame temperature is close to the adiabatic flame temperature and there is a temperature difference above 1000 K between the symmetry axis and the combustor wall. These results suggest that the wall temperature defined in the boundary conditions is not the most appropriate. The pure hydrogen combustion does not normally take place due to the high temperatures existing inside the combustion chamber, which leads to changes in the physical properties of the combustor material and to an increase in its wear under intensive conditions.
- In CH_4/NH_3 mixtures, the flameless combustion is expected to be possible at $\varphi \leq 1$ and the conventional non-premixed combustion occurs in the fuel-rich condition. In fuel-lean conditions, the NOx and CO emissions are higher than 3400 ppm and 120 ppm, respectively, and that for $\varphi \geq 1$ the CO emission is above 1200 ppm and the NO_x emission is below 1700 ppm. The NO_x emission decreases for $\varphi \geq 1$ because the NH_3 has a greater tendency to pyrolyze and form N_2 and H_2 and also due to the NH_2 and NO recombination to form N_2 and H_2O [89].
- In relation to H_2 /NH_3 mixtures, the NO_x emission decreases when the NH_3 concentration in the fuel increases because NH_3 has a self-inhibiting effect its own oxidation. The flameless combustion is expected to occur for $\varphi \leq 1$ and the NO_x emission is higher than 3000 ppm. In the fuel-rich condition, the conventional non-premixed combustion is observed and the NO_x emission is below 1000 ppm.
- In the CH_4/NH_3 and H_2/NH_3 combustion, the CO, H_2 and NH_3 emissions in the exhaust gas suggest that the combustion chamber used is not long enough. The possible techniques to reduce the CO and NO_x emissions are the use of a larger combustion chamber, the external recirculation of the exhaust gases and the introduction of secondary air downstream of the second half of the combustor.

6.2 Future Works

In the course of this work, some aspects were identified that can be considered in future investigations in order to improve the understanding of the phenomena associated with flameless combustion and conventional non-premixed combustion. The following suggestions for future work are presented:

- Perform experimental tests for the fuels and operating conditions studied in order to extract axial and radial profiles of temperature, velocity and concentrations of O_2, CO_2, CO, NO_x, NH_3 and unburned hydrocarbons. And compare the experimental and numerical results to validate the numerical model used.
- Develop a detailed kinetic mechanism suitable for the acetylene combustion in which soot and NO_x formation mechanisms are incorporated, as well as perform a kinetic study and sensitivity analysis in order to know the preferred acetylene oxidation pathways.
- To study the influence of the air inlet temperature and the equivalence ratio to obtain flameless combustion in syngas and acetylene, but also to study the critical values for which this combustion mode no longer occurs for the other fuels proposed in this work.
- Perform a kinetic study and sensitivity analysis of the preferred NO_x formation pathways for each fuel and check if the preferred NO_x formation mechanisms differ with the fuel used.
- For mixtures with ammonia, it is suggested to study the influence of the combustion chamber size, the influence of the external flue gas recirculation and the influence of secondary air introduced downstream of the second half of the combustor.
- Perform a kinetic study and a sensitivity analysis of the preferred pathways for ammonia flameless combustion for the different NH_3 concentrations and equivalence ratios.

References

[1] “The Paris Agreement | UNFCCC.”. Accessed on Jan. 16, 2020. [Online]. Available: https://unfccc.int/process-and-meetings/the-paris-agreement/the-paris-agreement

[2] H. Van Soest et al., “Opportunities for Enhanced Action to Keep Paris Goals in Reach”. Accessed on Jan. 16, 2020. [Online]. Available: https://themasites.pbl.nl/commit/wp-content/uploads/Opportunities-for-Enhanced-Action-to-Keep-Paris-Goals-within-Reach-COMMITCD-LINKS-policy-brief.pdf

[3] P. Capros, EU Reference Scenario 2016. Accessed on Jan. 16, 2020. [Online]. Available: https://op.europa.eu/en/publication-detail/-/publication/aed45f8e-63e3-47fb-9440-a0a14370f243/language-en/format-PDF/source-106883045

[4] B. Miller, “Greenhouse gas – carbon dioxide emissions reduction technologies” in Fossil Fuel Emissions Control Technologies, 2015, pp. 367-438.

[5] P. F. Li et al., “Progress and recent trend in MILD combustion,” Sci. China Technol. Sci., vol. 54, no. 2, pp. 255–269, 2011, doi: 10.1007/s11431-010-4257-0.

[6] M. P. Boyce, Advanced industrial gas turbines for power generation. Elsevier Masson SAS., 2012.

[7] A. E. E. Khalil and A. K. Gupta, “Fuel flexible distributed combustion for efficient and clean gas turbine engines,” Appl. Energy, vol. 109, pp. 267–274, 2013, doi: 10.1016/j.apenergy.2013.04.052.

[8] P. J. Coelho and M. Costa, Combustão, 2nd ed. Edições Orion, 2012.

[9] T. J. Poinsot and D. P. Veynante, “Combustion,” in Encyclopedia of Computational Mechanics, 2004th ed., E. Stein, R. de Borst, and T. J. R. Hughes, Eds. John Wiley & Sons, Ltd, 1978, pp. 201–256.

[10] S. K. Aggarwal, “Extinction of laminar partially premixed flames,” Prog. Energy Combust. Sci., vol. 35, no. 6, pp. 528–570, 2009, doi: 10.1016/j.pecs.2009.04.003.

[11] D. L. Wisman, S. D. Marcum, and B. N. Ganguly, “Electrical control of the thermodiffusive instability in premixed propane-air flames,” Combust. Flame, vol. 151, no. 4, pp. 639–648, 2007, doi: 10.1016/j.combustflame.2007.06.021.

[12] J. A. Wünning and J. G. Wünning, “Flameless Oxidation to Reduce Thermal NO-Formation”, Prog. Energy Combust. Sci., vol. 23, no. 1, pp. 81–94, 1997, doi: 10.1016/S0360-1285(97)00006-3

[13] A. Cavaliere and M. De Joannon, “Mild combustion,” Prog. Energy Combust. Sci., vol. 30, no. 4, pp. 329–366, 2004, doi: 10.1016/j.pecs.2004.02.003.

[14] P. Li, B. B. Dally, J. Mi, and F. Wang, “MILD oxy-combustion of gaseous fuels in a laboratory-scale furnace,” Combust. Flame, vol. 160, no. 5, pp. 933–946, 2013, doi: 10.1016/j.combustflame.2013.01.024.

[15] P. Sabia, “Experimental and Numerical Study of Mild Combustion Processes in Model Reactors,” Ph.D. dissertation, Scuola Politecnica e delle Scienze di Base, Università Degli Studi di Napoli Fredeico II, 2006.

[16] A. Rebola, M. Costa, and P. J. Coelho, “Experimental evaluation of the performance of a flameless combustor,” Appl. Therm. Eng., vol. 50, no. 1, pp. 805–815, 2013, doi: 10.1016/j.applthermaleng.2012.07.027.

[17] S. E. Hosseini, G. Bagheri, and M. A. Wahid, “Numerical investigation of biogas flameless combustion,” Energy Convers. Manag., vol. 81, pp. 41–50, 2014, doi: 10.1016/j.enconman.2014.02.006.

[18] J. Mi, P. Li, B. B. Dally, and R. A. Craig, “Importance of initial momentum rate and air-fuel premixing on moderate or intense low oxygen dilution (MILD) combustion in a recuperative furnace,” Energy and Fuels, vol. 23, no. 11, pp. 5349–5356, 2009, doi: 10.1021/ef900866v.

[19] J. Ye, P. R. Medwell, B. B. Dally, and M. J. Evans, “The transition of ethanol flames from conventional to MILD combustion,” Combust. Flame, vol. 171, pp. 173–184, 2016, doi: 10.1016/j.combustflame.2016.05.020.

[20] J. Ye, P. R. Medwell, E. Varea, S. Kruse, B. B. Dally, and H. G. Pitsch, “An experimental study on MILD combustion of prevaporised liquid fuels,” Appl. Energy, vol. 151, pp. 93–101, 2015, doi: 10.1016/j.apenergy.2015.04.019.

[21] D. Perrone, T. Castiglione, A. Klimanek, P. Morrone, and M. Amelio, “Numerical simulations on Oxy-MILD combustion of pulverized coal in an industrial boiler,” Fuel Process. Technol., vol. 181, no. September, pp. 361–374, 2018, doi: 10.1016/j.fuproc.2018.09.001.

[22] B. Lou, Y. H. Lou, and X. Q. Ma, “Model and experimental validation on NOx emission of biomass combustion in rotary kiln with HTAC,” Proceedings Chinese Soc. Electr. Eng., vol. 27, pp. 68–73, 2007.

[23] C. Galletti, A. Parente, and L. Tognotti, “Numerical and experimental investigation of a mild combustion burner,” Combust. Flame, vol. 151, no. 4, pp. 649–664, 2007, doi: 10.1016/j.combustflame.2007.07.016.

[24] M. Huang et al., “Effect of air preheat temperature on the MILD combustion of syngas,” Energy Convers. Manag., vol. 86, no. x, pp. 356–364, 2014, doi: 10.1016/j.enconman.2014.05.038.

[25] K. P. Cheong, G. Wang, B. Wang, R. Zhu, W. Ren, and J. Mi, “Stability and emission characteristics of nonpremixed MILD combustion from a parallel-jet burner in a cylindrical furnace,” Energy, vol. 170, pp. 1181–1190, 2019, doi: 10.1016/j.energy.2018.12.146.

[26] X. Huang, M. J. Tummers, and D. J. E. M. Roekaerts, “Experimental and numerical study of MILD combustion in a lab-scale furnace,” Energy Procedia, vol. 120, pp. 395–402, 2017, doi: 10.1016/j.egypro.2017.07.231.

[27] Y. Liu, J. Cheng, C. Zou, L. Cai, Y. He, and C. Zheng, “Experimental and numerical study on the CO formation mechanism in methane MILD combustion without preheated air,” Fuel, vol. 192, pp. 140–148, 2017, doi: 10.1016/j.fuel.2016.12.010.

[28] A. S. Veríssimo, A. M. A. Rocha, and M. Costa, “Operational, Combustion, and Emission Characteristics of a Small-Scale Combustor,” Energy Fuels, vol. 25, no. 6, pp. 2469-2480, 2011, doi: 10.1021/ef200258t.

[29] S. Karyeyen, “Combustion characteristics of a non-premixed methane flame in a generated burner under distributed combustion conditions: A numerical study,” Fuel, vol. 230, pp. 163–171, 2018, doi: 10.1016/j.fuel.2018.05.052.

[30] M. Castela, A. S. Veríssimo, A. M. A. Rocha, and M. Costa, “Experimental study of the combustion regimes occurring in a laboratory combustor,” Combust. Sci. Technol., vol. 184, no. 2, pp. 243–258, 2012, doi: 10.1080/00102202.2011.630592.

[31] Y. Tu, H. Liu, S. Chen, Z. Liu, H. Zhao, and C. Zheng, “Effects of furnace chamber shape on the MILD combustion of natural gas,” Appl. Therm. Eng., vol. 76, pp. 64–75, 2015, doi: 10.1016/j.applthermaleng.2014.11.007.

[32] Y. Tu, M. Xu, D. Zhou, Q. Wang, W. Yang, and H. Liu, “CFD and kinetic modelling study of methane MILD combustion in O2/N2, O2/CO2 and O2/H2O atmospheres,” Appl. Energy, vol. 240, pp. 1003–1013, 2019, doi: 10.1016/j.apenergy.2019.02.046.

[33] G. Sorrentino, P. Sabia, M. De Joannon, A. Cavaliere, and R. Ragucci, “Design and development of a lab-scale burner for MILD/flameless combustion,” Chem. Eng. Trans., vol. 43, pp. 883–888, 2015, doi: 10.3303/CET1543148.

[34] G. Sorrentino, P. Sabia, P. Bozza, R. Ragucci, and M. de Joannon, “Impact of external operating parameters on the performance of a cyclonic burner with high level of internal recirculation under MILD combustion conditions,” Energy, vol. 137, pp. 1167–1174, 2017, doi: 10.1016/j.energy.2017.05.135.

[35] K. P. Cheong, G. Wang, J. Mi, B. Wang, R. Zhu, and W. Ren, “Premixed MILD Combustion of Propane in a Cylindrical Furnace with a Single Jet Burner: Combustion and Emission Characteristics,” Energy and Fuels, vol. 32, no. 8, pp. 8817–8829, 2018, doi: 10.1021/acs.energyfuels.8b01587.

[36] M. U. Alzueta, M. Borruey, A. Callejas, A. Millera, and R. Bilbao, “An experimental and modeling study of the oxidation of acetylene in a flow reactor,” Combust. Flame, vol. 152, no. 3, pp. 377–386, 2008, doi: 10.1016/j.combustflame.2007.10.011.

[37] X. Shen, X. Yang, J. Santner, J. Sun, and Y. Ju, “Experimental and kinetic studies of acetylene flames at elevated pressures,” Proc. Combust. Inst., vol. 35, no. 1, pp. 721–728, 2015, doi: 10.1016/j.proci.2014.05.106.

[38] F. Xu and G. M. Faeth, “Soot formation in laminar acetylene/air diffusion flames at atmospheric pressure,” Combust. Flame, vol. 125, no. 1–2, pp. 804–819, 2001, doi: 10.1016/S0010-2180(01)00221-8.

[39] Z. Al-Hamamre and J. Yamin, “The effect of hydrogen addition on premixed laminar acetylene-hydrogen-air and ethanol-hydrogen-air flames,” Int. J. Hydrogen Energy, vol. 38, no. 18, pp. 7499–7509, 2013, doi: 10.1016/j.ijhydene.2013.03.125.

[40] S. E. Hosseini and M. A. Wahid, “Biogas utilization: Experimental investigation on biogas flameless combustion in lab-scale furnace,” Energy Convers. Manag., vol. 74, pp. 426–432, 2013, doi: 10.1016/j.enconman.2013.06.026.

[41] A. F. Colorado, B. A. Herrera, and A. A. Amell, “Performance of a Flameless combustion furnace using biogas and natural gas,” Bioresour. Technol., vol. 101, no. 7, pp. 2443–2449, 2010, doi: 10.1016/j.biortech.2009.11.003.

[42] A. Mameri, F. Tabet, and A. Hadef, “MILD combustion of hydrogenated biogas under several operating conditions in an opposed jet configuration,” Int. J. Hydrogen Energy, vol. 43, no. 6, pp. 3566–3576, 2018, doi: 10.1016/j.ijhydene.2017.04.273.

[43] C. G. de Azevedo, J. C. de Andrade, and F. de Souza Costa, “Flameless compact combustion system for burning hydrous ethanol,” Energy, vol. 89, pp. 158–167, 2015, doi: 10.1016/j.energy.2015.07.049.

[44] A. E. E. Khalil and A. K. Gupta, “Fostering distributed combustion in a swirl burner using prevaporized liquid fuels,” Appl. Energy, vol. 211, pp. 513–522, 2018, doi: 10.1016/j.apenergy.2017.11.068.

[45] S. Zhu, A. Pozarlik, D. Roekaerts, H. C. Rodrigues, and T. van der Meer, “Numerical investigation towards HiTAC conditions in laboratory-scale ethanol spray combustion,” Fuel, vol. 211, pp. 375–389, 2018, doi: 10.1016/j.fuel.2017.09.002.

[46] L. Yang and X. Ge, “Biogas and Syngas Upgrading,” in Advances in Bioenergy, vol. 1, Y. Li and X. Ge, Eds. 2016, pp. 125–188.

[47] M. Huang et al., “Effect of air/fuel nozzle arrangement on the MILD combustion of syngas,” Appl. Therm. Eng., vol. 87, pp. 200–208, 2015, doi: 10.1016/j.applthermaleng.2015.04.076.

[48] M. M. Huang et al., “Effect of fuel injection velocity on MILD combustion of syngas in axially-staged combustor,” Appl. Therm. Eng., vol. 66, no. 1–2, pp. 485–492, 2014, doi: 10.1016/j.applthermaleng.2014.02.033.

[49] A. Mardani and H. Karimi Motaalegh Mahalegi, “Hydrogen enrichment of methane and syngas for MILD combustion,” Int. J. Hydrogen Energy, vol. 44, no. 18, pp. 9423–9437, 2019, doi: 10.1016/j.ijhydene.2019.02.072.

[50] Y. Yu, W. Gaofeng, L. Qizhao, M. Chengbiao, and X. Xianjun, “Flameless combustion for hydrogen containing fuels,” Int. J. Hydrogen Energy, vol. 35, no. 7, pp. 2694–2697, 2010, doi: 10.1016/j.ijhydene.2009.04.036.

[51] M. Ayoub, C. Rottier, S. Carpentier, C. Villermaux, A. M. Boukhalfa, and D. Honoré, “An experimental study of mild flameless combustion of methane/hydrogen mixtures,” Int. J. Hydrogen Energy, vol. 37, no. 8, pp. 6912–6921, 2012, doi: 10.1016/j.ijhydene.2012.01.018.

[52] M. Nikakhtar and M. H. Akbari, “Modeling of Flameless Combustion of Hydrogen in Combustor of a Gas Turbine,” in The Fourth Fuel & Combustion Conference of IRAN, University of Kashan, Kashan, 2012.

[53] S. Lee and O. C. Kwon, “Effects of ammonia substitution on extinction limits and structure of counterflow nonpremixed hydrogen/air flames,” Int. J. Hydrogen Energy, vol. 36, no. 16, pp. 10117–10128, 2011, doi: 10.1016/j.ijhydene.2011.05.082.

[54] D. H. Um, J. M. Joo, S. Lee, and O. C. Kwon, “Combustion stability limits and NOx emissions of nonpremixed ammonia-substituted hydrogen-air flames,” Int. J. Hydrogen Energy, vol. 38, no. 34, pp. 14854–14865, 2013, doi: 10.1016/j.ijhydene.2013.08.140.

[55] R. Li, A. A. Konnov, G. He, F. Qin, and D. Zhang, “Chemical mechanism development and reduction for combustion of NH3/H2/CH4 mixtures,” Fuel, vol. 257, p. 116059, 2019, doi: 10.1016/j.fuel.2019.116059.

[56] B. B. Dally, A. N. Karpetis, and R. S. Barlow, “Structure of turbulent non-premixed jet flames in a diluted hot coflow,” Proc. Combust. Inst., vol. 29, no. 1, pp. 1147–1154, 2002, doi: 10.1016/S1540-7489(02)80145-6.

[57] G. Sorrentino, P. Sabia, P. Bozza, R. Ragucci, and M. de Joannon, “Low-NOx conversion of pure ammonia in a cyclonic burner under locally diluted and preheated conditions,” Appl. Energy, vol. 254,pp. 1–7, 2019, doi: 10.1016/j.apenergy.2019.113676.

[58] F. C. Christo and B. B. Dally, “Modeling turbulent reacting jets issuing into a hot and diluted coflow,” Combust. Flame, vol. 142, no. 1–2, pp. 117–129, 2005, doi: 10.1016/j.combustflame.2005.03.002.

[59] A. Rebola, P. J. Coelho, and M. Costa, “Assessment of the performance of several turbulence and combustion models in the numerical simulation of a flameless combustor,” Combust. Sci. Technol., vol. 185, no. 4, pp. 600–626, 2013, doi: 10.1080/00102202.2012.739222.

[60] D. Lupant and P. Lybaert, “Assessment of the EDC combustion model in MILD conditions with in-furnace experimental data,” Appl. Therm. Eng., vol. 75, pp. 93–102, 2015, doi: 10.1016/j.applthermaleng.2014.10.027.

[61] A. Parente, C. Galletti, and L. Tognotti, “Effect of the combustion model and kinetic mechanism on the MILD combustion in an industrial burner fed with hydrogen enriched fuels,” Int. J. Hydrogen Energy, vol. 33, no. 24, pp. 7553–7564, 2008, doi: 10.1016/j.ijhydene.2008.09.058.

[62] D. Tabacco, C. Innarella, and C. Bruno, “Theoretical and Numerical Investigation on Flameless Combustion,” Combustion Science and Technology, vol. 174, 2002, doi: 10.1080/00102200208984086.

[63] A. De, E. Oldenhof, P. Sathiah, and D. Roekaerts, “Numerical simulation of Delft-Jet-in-Hot-Coflow (DJHC) flames using the eddy dissipation concept model for turbulence-chemistry interaction,” Flow, Turbul. Combust., vol. 87, no. 4, pp. 537–567, 2011, doi: 10.1007/s10494-011-9337-0.

[64] G. P. Smith et al., “GRI - Mech 3.0.” Accessed on Oct. 27, 2019. [Online]. Available: http://www.me.berkeley.edu/gri_mech/.

[65] A. S. Veríssimo, A. M. A. Rocha, P. J. Coelho, and M. Costa, “Experimental and Numerical Investigation of the Influence of the Air Preheating Temperature on the Performance of a Small-Scale Mild Combustor,” Combust. Sci. Technol., vol. 187, no. 11, pp. 1724–1741, 2015, doi: 10.1080/00102202.2015.1059330.

[66] R. Sankaran, E. R. Hawkes, J. H. Chen, T. Lu, and C. K. Law, “Structure of a spatially developing turbulent lean methane-air Bunsen flame,” Proc. Combust. Inst., vol. 31 I, no. 1, pp. 1291–1298, 2007, doi: 10.1016/j.proci.2006.08.025.

[67] C. Jiménez, B. Cuenot, T. Poinsot, and D. Haworth, “Numerical simulation and modeling for lean stratified propane-air flames,” Combust. Flame, vol. 128, no. 1–2, pp. 1–21, 2002, doi: 10.1016/S0010-2180(01)00328-5.

[68] A. Kazakov and M. Frenklach, “Reduced Reaction Sets based on GRI - Mech 1.2.” Accessed on Oct. 25, 2019. [Online]. Available: http://combustion.berkeley.edu/drm/.

[69] N. M. Marinov, “Kinetic Model for High Temperature Ethanol Oxidation,” Int. J. Chem. Kinet., vol. 31, no. 3, pp. 183–220, 1999, doi: 10.1002/(SICI)1097-4601(1999)31:3<183::AID-KIN3>3.0.CO;2-X

[70] G. H. Yeoh and K. K. Yuen, Computational Fluid Dynamics in Fire Engineering, 1st ed. USA: Elsevier Inc., 2009.

[71] H. K. Versteeg and W. Malalasekera, An Introduction to Computational Fluid Dynamics, 2nd ed. Essex, England: Pearson Education Limited, 2007.

[72] C. D. Argyropoulos and N. C. Markatos, “Recent advances on the numerical modelling of turbulent flows,” Appl. Math. Model., vol. 39, no. 2, pp. 693–732, 2015, doi: 10.1016/j.apm.2014.07.001.

[73] B. E. Launder and D. B. Spalding, Lectures in Mathematical Models of Turbulence. London, England: Academic Press, 1972.

[74] Ansys Inc., Ansys Fluent Theory Guide, 2017.

[75] F. R. Menter, “Two-Equation Eddy-Viscosity Turbulence Models for Engineering Applications,” AIAA J., vol. 32, no. 8, pp. 1598–1605, 1994, doi: 10.2514/3.12149.

[76] “SST K-Omega Turbulence Models | CFD | Autodesk Knowledge Network.” Accessed on Feb. 1, 2020. [Online]. Available: https://knowledge.autodesk.com/support/cfd/learn-explore/caas/CloudHelp/cloudhelp/2014/ENU/SimCFD/files/GUID-0F5C4828-9F91-46B6-A16A-2578D72DCFCC-htm.html. [Accessed: 11-Feb-2020].

[77] B. F. Magnussen, “On the Structure of Turbulence and a Generalized Eddy Dissipation Concept for Chemical Reaction in Turbulent Flow,” in Nineteenth AIAA Meeting, St. Louis, Jan. 12-15, 1981.

[78] S. B. Pope, “Computationally efficient implementation of combustion chemistry using in-situ adaptive tabulation,” Combust. Theory Model., vol. 1, pp. 41–63, 1997, doi: 10.1080/713665229.

[79] P. J. Coelho, “Advances in the discrete ordinates and finite volume methods for the solution of radiative heat transfer problems in participating media,” J. Quant. Spectrosc. Radiat. Transf., vol. 145, pp. 121–146, 2014, doi: 10.1016/j.jqsrt.2014.04.021.

[80] M. E. Modest, Radiative Heat Transfer, Third Edit. Oxford, UK: Elsevier Inc., 2013.

[81] T. F. Smith, Z. F. Shen, and J. N. Friedman, “Evaluation of Coefficients for the Weighted Sum of Gray Gases Model,” J. Heat Transfer, vol. 104, no. 4, pp. 602–608, 1982, doi: 10.1115/1.3245174.

[82] A. Coppalle and P. Vervisch, “The total emissivities of high-temperature flames,” Combust. Flame, vol. 49, no. 1–3, pp. 101–108, 1983, doi: 10.1016/0010-2180(83)90154-2.

[83] S. J. Brookes and J. B. Moss, “Prediction of soot and thermal radiation properties in confined turbulent jet diffusion flames,” Combust. Flame, vol. 116, pp. 486–503, 1999, doi: 10.1016/S0010-2180(98)00056-X.

[84] C. T. Bowman et al., “GRI-Mech 2.11.” Accessed on Oct. 27, 2019. [Online]. Available: http://www.me.berkeley.edu/gri_mech/.

[85] “CRECK Modeling Group.” Accessed on Nov. 20, 2019. [Online]. Available: http://creckmodeling.chem.polimi.it/.

[86] G. P. Smith and H. Wang, “Foundational Fuel Chemistry Model Version 1.0.” Accessed on Nov. 25, 2019. [Online]. Available: http://nanoenergy.stanford.edu/ffcm1.

[87] I. Glassman, O. Nishida, and G. Sidebotham, “Critical temperatures of soot formation,” Springer Ser. Chem. Phys., no. 59, pp. 316–324, 1994, doi: 10.1007/978-3-642-85167-4_18.

[88] J. O. L. Wendt and C. V. Sternling, “Effect of Ammonia in Gaseous Fuels on Nitrogen Oxide Emissions,” J. Air Pollut. Control Assoc., vol. 24, no. 11, pp. 1055–1058, 1974, doi: 10.1080/00022470.1974.10470013.

[89] S. Koger and H. Bockhorn, “NOx formation from ammonia, hydrogen cyanide, pyrrole, and caprolactam under incinerator conditions,” Proc. Combust. Inst., vol. 30, no. 1, pp. 1201–1209, 2005, doi: 10.1016/j.proci.2004.08.114.

[90] N. A. Hussein, A. Valera-Medina, and A. S. Alsaegh, “Ammonia- hydrogen combustion in a swirl burner with reduction of NOx emissions,” Energy Procedia, vol. 158, no. 2018, pp. 2305–2310, 2019, doi: 10.1016/j.egypro.2019.01.265.

[91] M. Bal, “Numerical investigation of the influence of operating conditions on a mild laboratory scale combustor,” Master Thesis in Energy Engineering and Management, Instituto Superior Técnico, Universidade de Lisboa, 2015.

Appendix

Appendix A.1

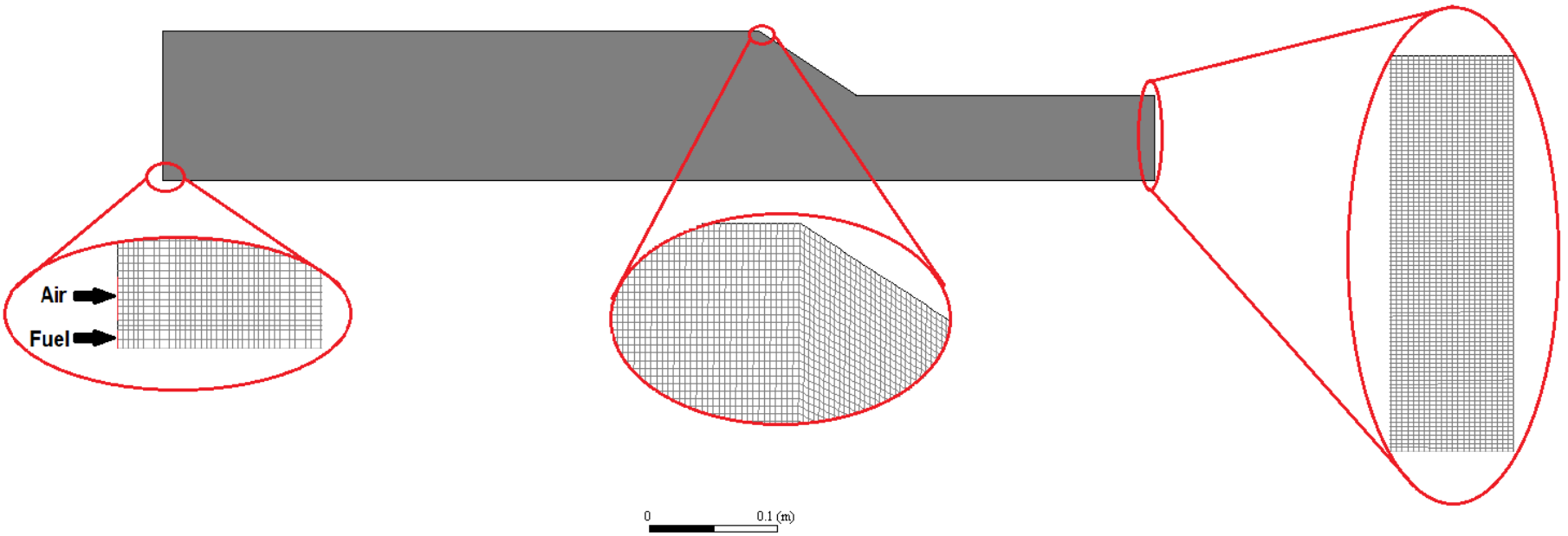

Figure A. 1 – Intermediate mesh with ~ 79 000 cells.

Appendix A.2

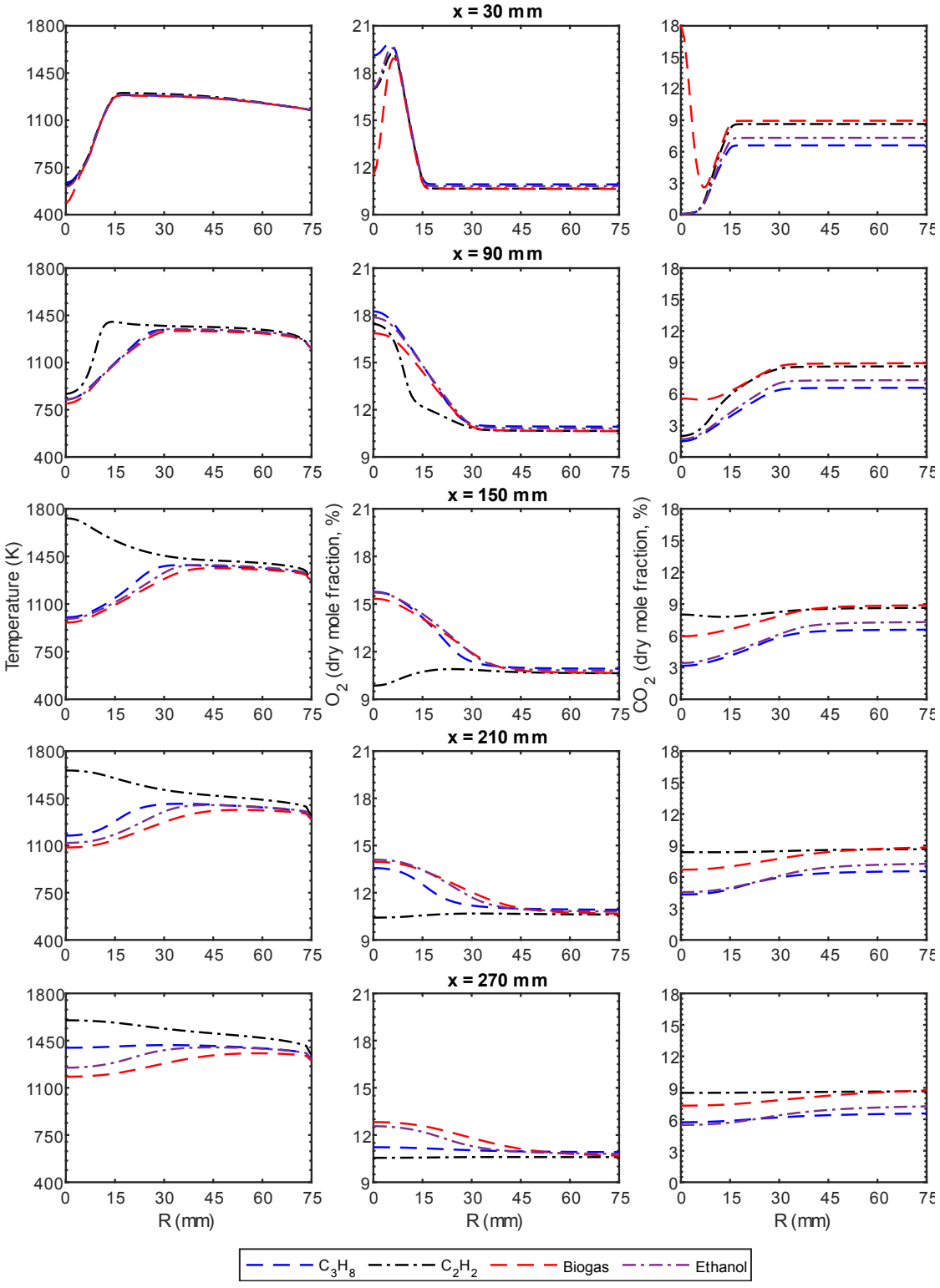

Figure A.2 – Radial profiles of temperature, O_2 and CO_2 concentrations on a dry basis for combustion of propane (C_3H_8), acetylene (C_2H_2), biogas and ethanol.

Appendix A.3

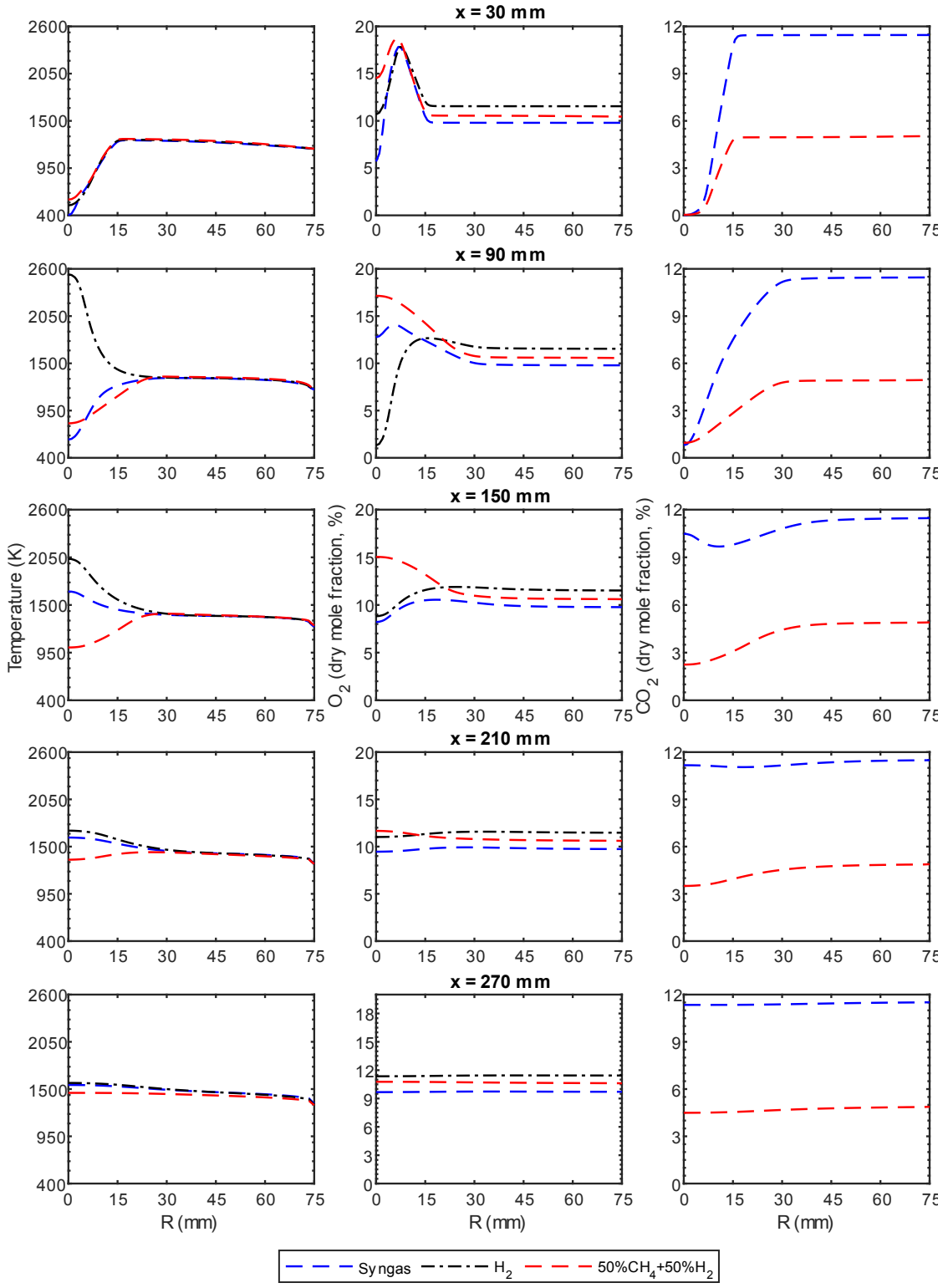

Figure A.3 – Radial profiles of temperature and O_2 and CO_2 concentrations on a dry basis for combustion of syngas, hydrogen (H_2) and CH_4/H_2 mixture.

Appendix A.4

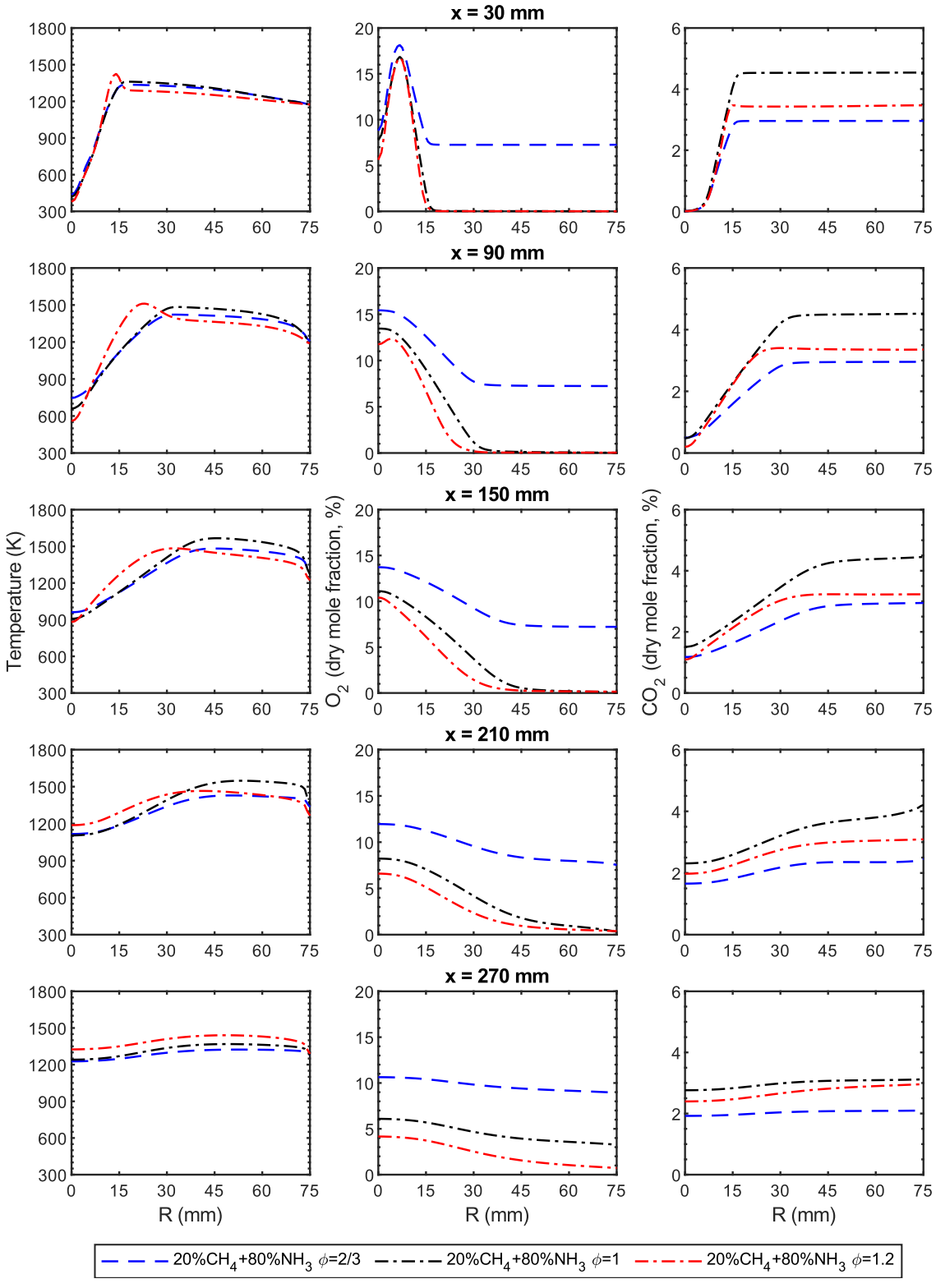

Figure A.4 – Radial profiles of temperature and O_2 and CO_2 concentrations on dry basis for combustion of CH_4/NH_3 mixture.

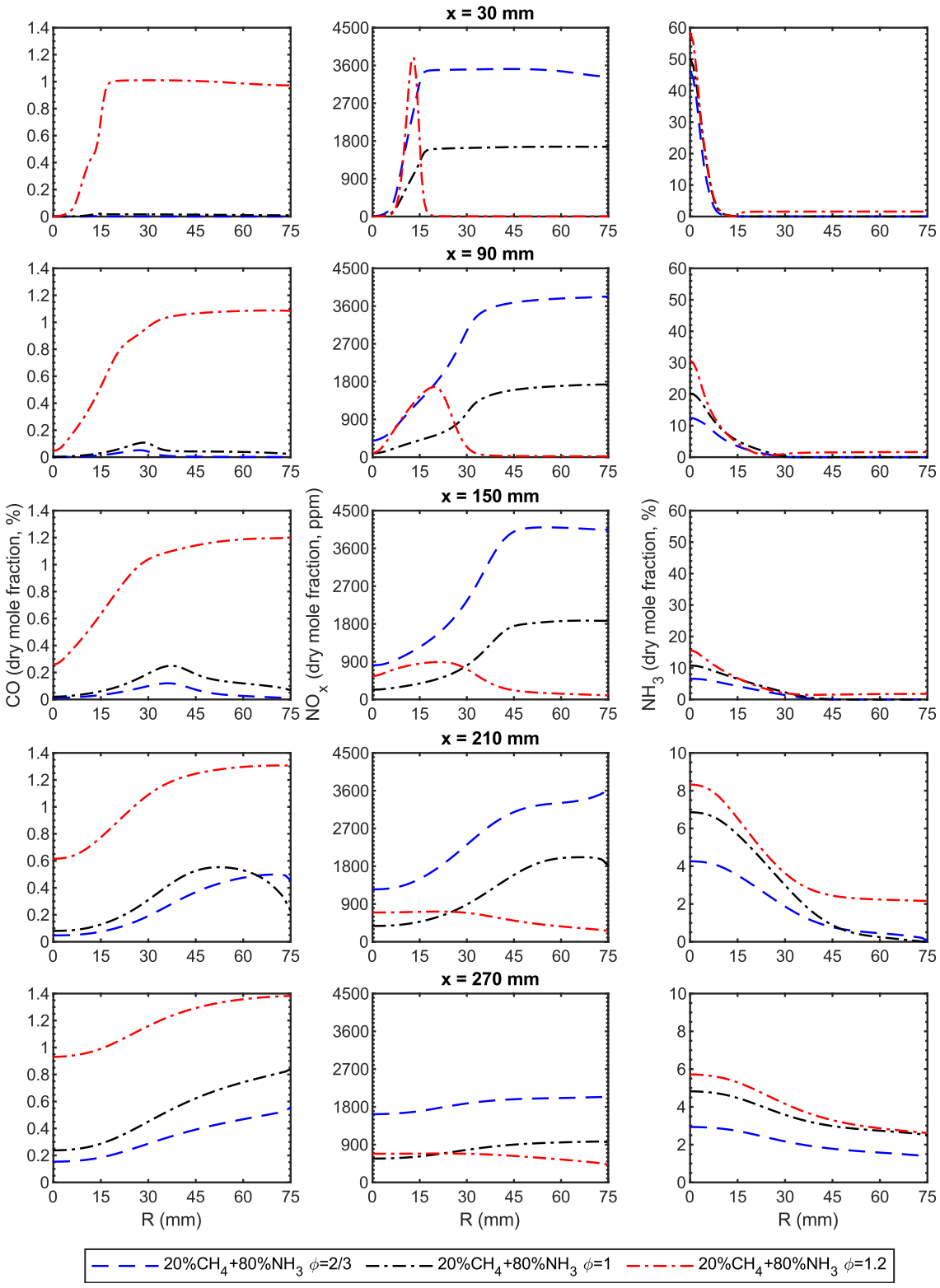

Figure A.5 – Radial profiles of CO, NO_x and NH_3 concentrations on a dry basis for combustion of CH_4/NH_3 mixture.

Appendix A.5

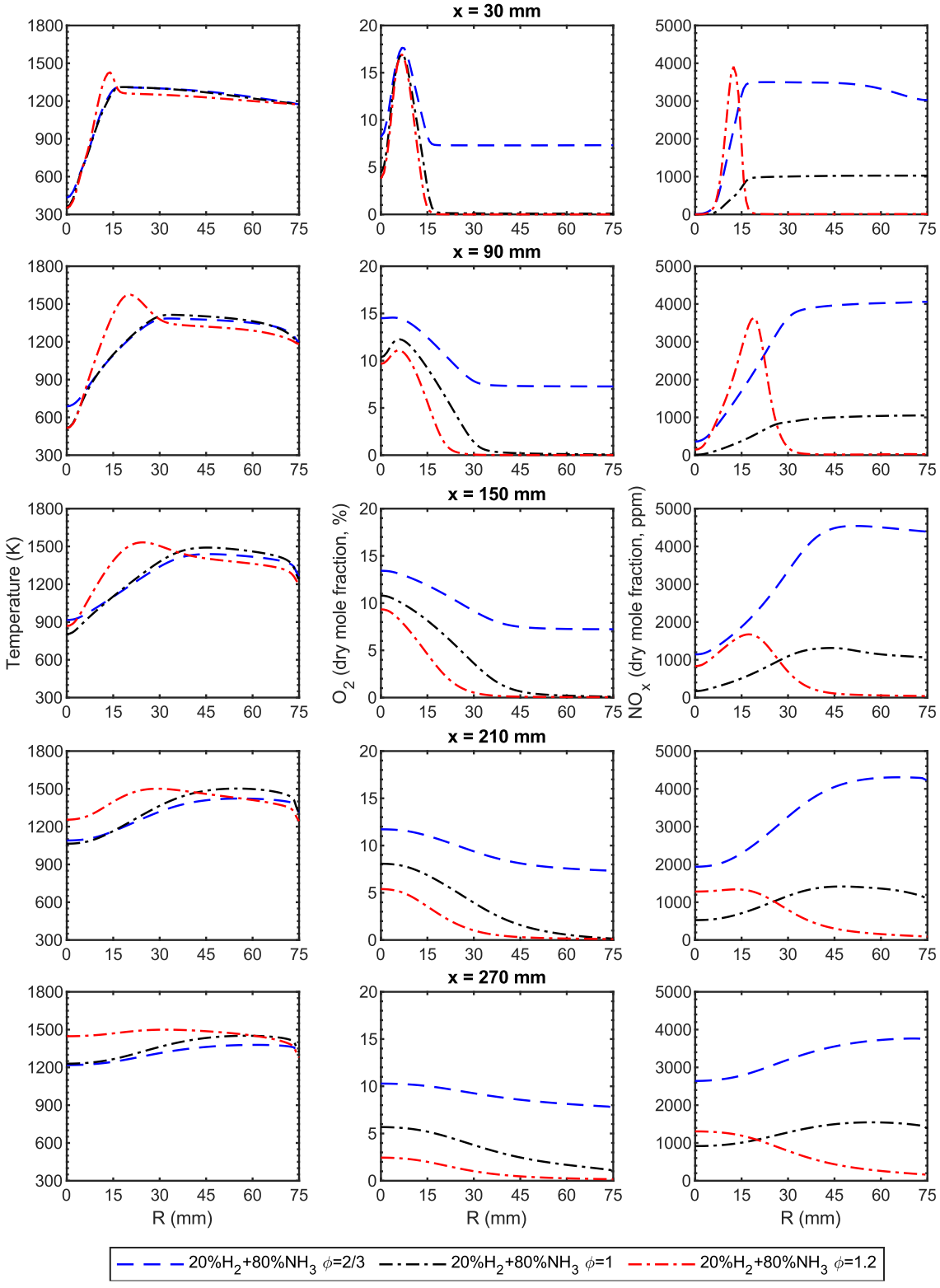

Figure A.6 – Radial profiles of temperature, O_2 and NO_x concentrations on a dry basis for combustion of H_2/NH_3 mixture.

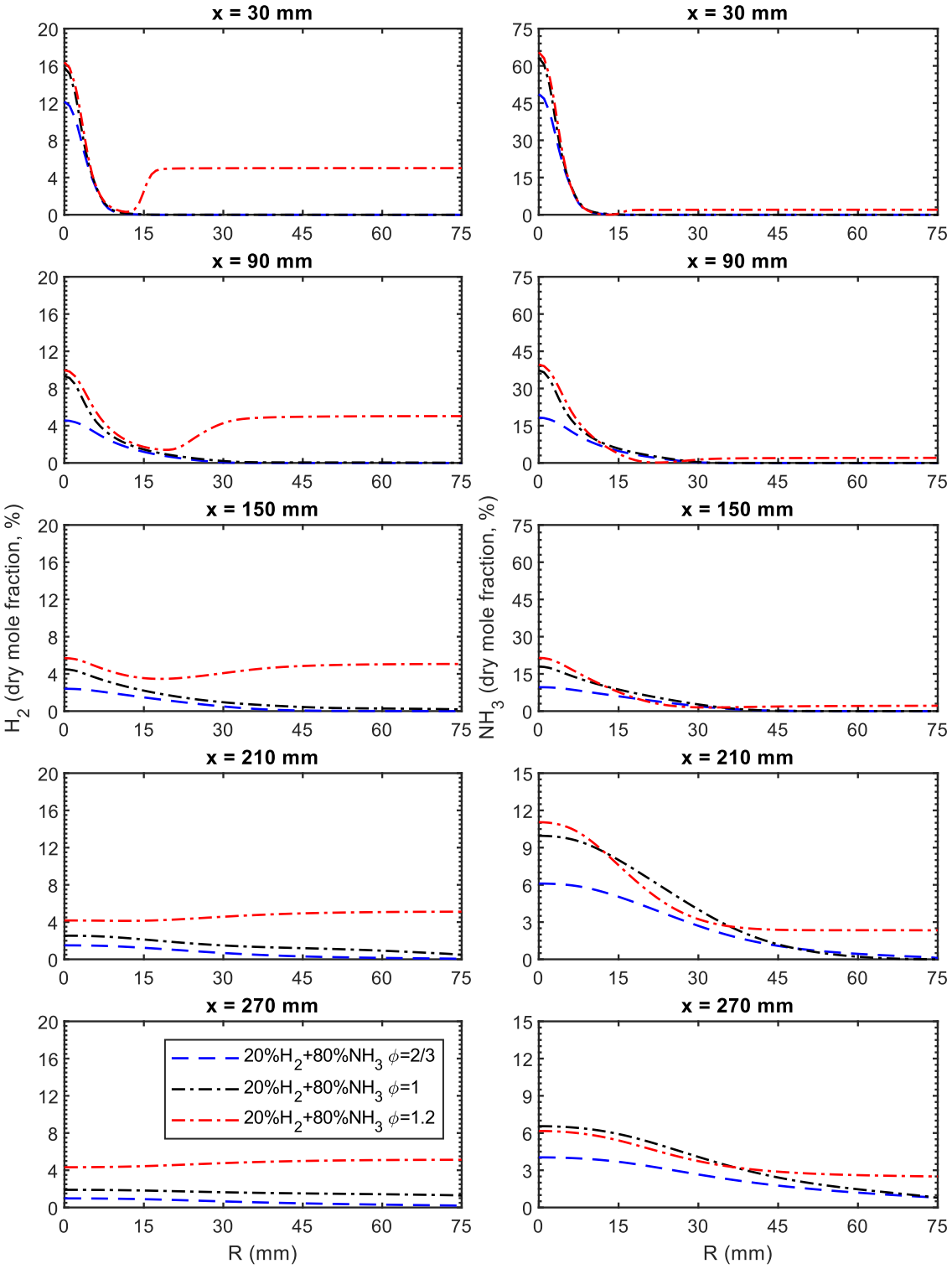

Figure A.7 – Radial profiles of H_2 and NH_3 concentrations on a dry basis for combustion of H_2/NH_3 mixture.

Appendix B

O_2 mole fraction contours of the fuels studied

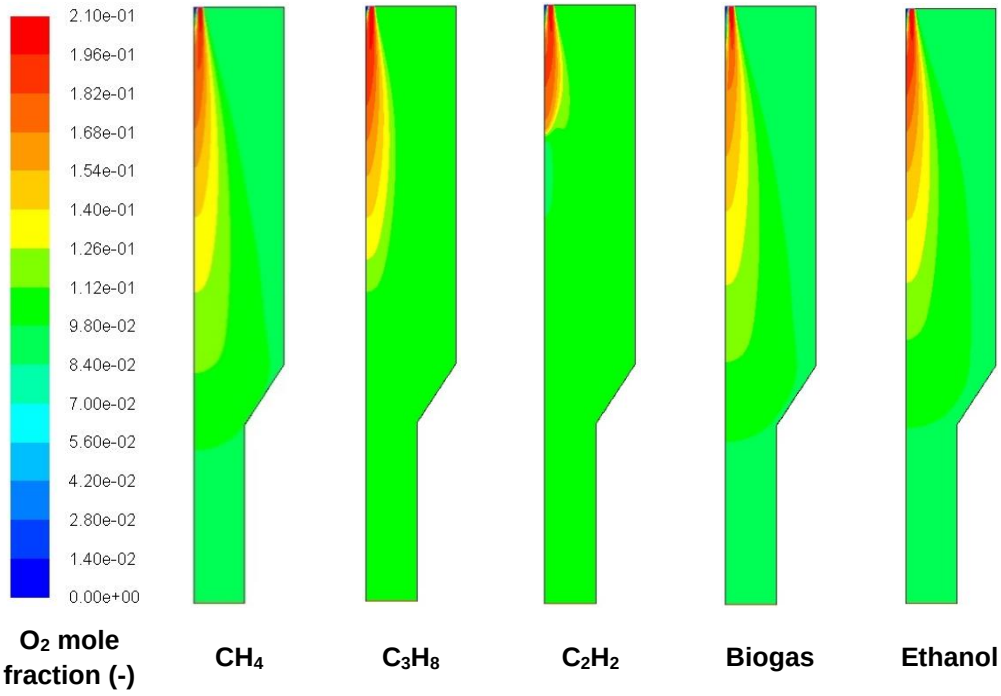

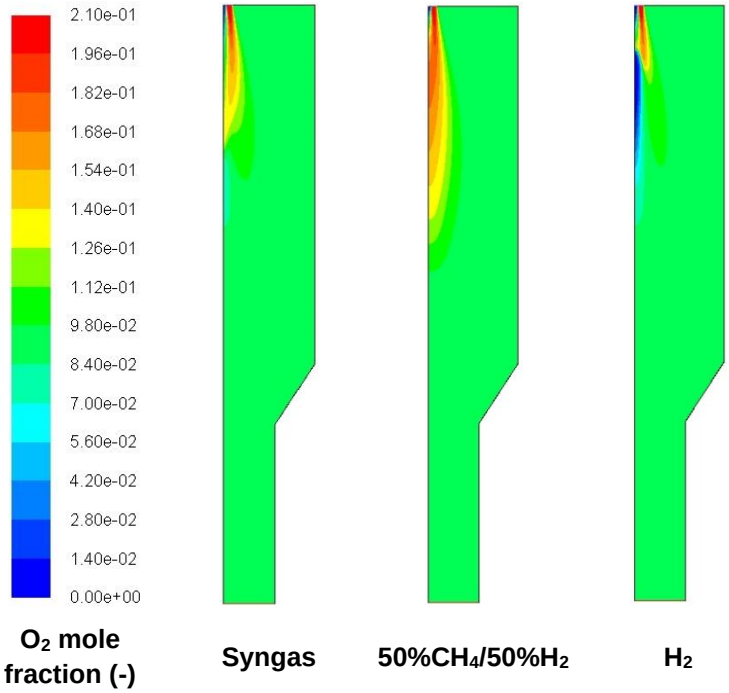

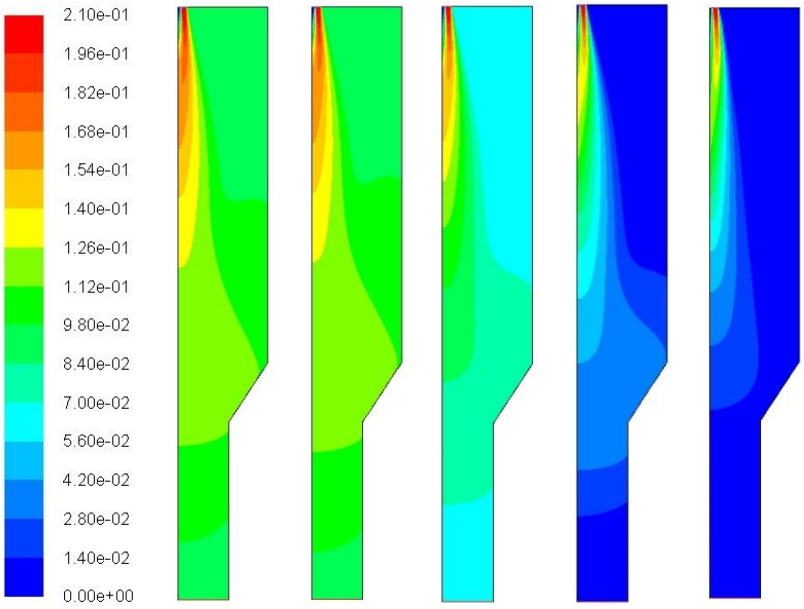

O_2 mole fraction (-)	30%CH_4 + 70%NH_3 φ =0.5	20%CH_4 + 80%NH_3 φ =0.5	20%CH_4 + 80%NH_3 φ =2/3	20%CH_4 + 80%NH_3 φ =1	20%CH_4 + 80%NH_3 φ =1.2

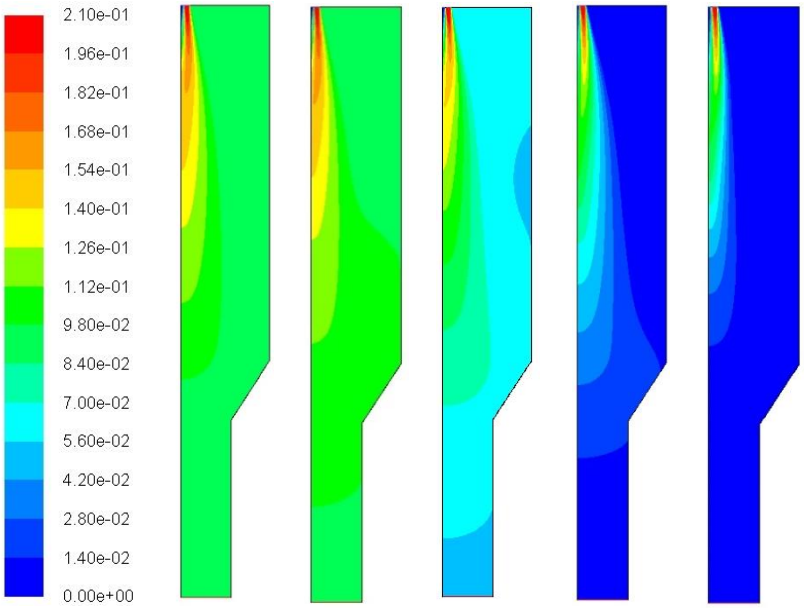

O_2 mole fraction (-)	30%H_2 + 70%NH_3 φ =0.5	20%H_2 + 80%NH_3 φ =0.5	20%H_2 + 80%NH_3 φ =2/3	20%H_2 + 80%NH_3 φ =1	20%H_2 + 80%NH_3 φ =1.2